Behaviour and Modelling of Flow-Drilling Screw Connections

Dan Hugo Amundsen

Jo Utne Gustad

Department of Structural Engineering
Faculty of Engineering Science and Technology
NTNU - Norwegian University of Science and Technology

MASTER THESIS 2014

SUBJECT AREA:	DATE:	NO. OF PAGES:
COMPUTATIONAL MECHANICS	10.06.2014	138 (121 + 17)

TITLE:

Behaviour and Modelling of Flow-Drilling Screw Connections
Åtferd og modellering av sambindingar med sjølvborande skruar

BY:

Dan Hugo Amundsen and
Jo Amund Utne Gustad

ABSTRACT:

This thesis presents an experimental and numerical study on the behaviour of Flow-Drilling Screw (FDS) connections under various quasi-static loading conditions, joining dissimilar materials. The behaviour and failure of the connections were closely studied by means of tests on simple coupons joined with a single connector and component tests.

Single-connector tests were performed on both two- and three-layered specimens. Cross tests in three loading directions, lap-joint tests and peeling tests were conducted for both configurations. The two-layered cross tests were used to calibrate two different macroscopic models. The first model was a point-connector model developed for self-piercing rivets (SPR), while the other was a material model developed for spot welds. Two different assemblies of three-layered cross tests were used to calibrate the SPR model for three-layered FDS connections. All models were validated by simulations of the lap-joint and peeling tests. A component test was performed to validate the two-layered macroscopic models for complex loading situations.

In the single-connector tests, shear-dominated loading situations generally produced higher forces than tension-dominated. Failure in the connections was mostly caused by pull-out from the bottom sheet. For the three-layered crosses and lap-joint specimens failure due to fracture of the screw itself, near the screw-head, was observed. In the component, all screws experienced both rotation and one-sided thread stripping.

The spotweld model was able to represent the stiffness and maximum force in some tests, but failure occurred too early in all simulations. The macroscopic model developed for SPR connections generally gave a good representation of the results, except under-predicting the force in peeling. The macroscopic model of the three-layered specimens showed some acceptable results, but under-estimated the forces in peeling, and over-estimated both force and displacement for the lap-joint. The macroscopic models gave an acceptable representation of maximum force in the component test, but were not able to accurately represent the stiffness observed in the experiments.

To develop a macroscopic model for FDS more work is necessary. The SPR model seems reliable for two-layered connections, but a model for three-layered connections requires further calibration, especially for shear-dominated loading cases. The spotweld model shows promising results, but further optimisation of the parameters must be conducted to conclude.

Department of Structural Engineering
Faculty of Engineering Science and Technology
NTNU - Norwegian University of Science and Technology

MASTER THESIS 2014

for

Dan Hugo Amundsen and Jo Amund Utne Gustad

Behaviour and Modelling of Flow-Drilling Screw Connections

During a car crash, the load bearing structure of a vehicle has to maintain its integrity such that minimal forces are transferred to the occupants. This means that all structural elements in the car body and the connections between them have to behave in a controlled and reliable manner. Spot welding, riveting, clinching and flow-drilling screwing are some of the joining techniques currently used in the automotive industry to join aluminium parts in the load carrying structure.

Large scale finite element simulations with shell elements are extensively used by the automotive industry to optimise vehicle designs. This requires not only accurate material models, but also robust and reliable models for the connections between the different parts of the structure, in order to correctly predict the real life behaviour of the car body, for instance in a crash situation. However, no models for large scale shell analyses tailored for flow-drilling screw connections are yet available.

In order to establish a basis for a new engineering model for flow-drilling screw connections, a research programme is established at SIMLab, NTNU. The present thesis is thus a part of this project and will focus on connections where an AA6016 T4 sheet is joined to an AA6063 T6 extrusion. Both two- and three-layered connections are to be considered.

The following plan for the Master's project is proposed:
- Material testing of the AA6063 T6, with subsequent material model calibration and validation.
- Single connector tests in order to reveal the mechanical behaviour under different loading conditions.
- Calibration and validation of available point-connector models for large scale shell analyses.
- Validation of the calibrated models using component tests.

Supervisors: Magnus Langseth, David Morin and Johan Kolstø Sønstabø from SIMLab

The thesis must be written according to current requirements and submitted to the Department of Structural Engineering, NTNU, no later than June 10th, 2014.

NTNU, January 14th, 2014

Magnus Langseth
Professor

Preface

This master's thesis in computational mechanics was written for the Centre for Research-Based Innovation (CRI) SIMLab hosted by the Department of Structural Engineering, Norwegian University of Science and Technology. The work has been conducted in the spring semester of 2014, and the extent of the work is 30 educational points per author.

Firstly, we would like to thank our project supervisors Professor Magnus Langseth, Dr. David Morin and Johan Kolstø Sønstabø, for constructive response to our work, and inspiring guidance during our work. Sønstabø has contributed not only with knowledge, but also helped with conducting experiments and with shaping the report. We would also like to thank the following persons: Chief Engineer Trond Auestad for support during the experimental tests in the laboratory. Dr. Egil Fagerholt for assistance and analytical help with DIC analysis. Mechanic Tore Wisth for machining the specimens used and the test setup for the component test.

Assembly of all screwed connections were done by Honda R&D Americas, Inc.

<div align="center">

Trondheim, June 10, 2014

</div>

<div align="center">

_____   _____
Dan Hugo Amundsen   Jo Amund Utne Gustad

</div>

Abstract

This thesis presents an experimental and numerical study on the behaviour of Flow-Drilling Screw (FDS) connections under various quasi-static loading conditions, joining dissimilar materials. The behaviour and failure of the connections were closely studied by means of tests on simple coupons joined with a single connector and component tests.

Single-connector tests were performed on both two- and three-layered specimens. Cross tests in three loading directions, lap-joint tests and peeling tests were conducted for both configurations. The two-layered cross tests were used to calibrate two different macroscopic models. The first model was a point-connector model developed for self-piercing rivets (SPR), while the other was a material model developed for spot welds. Two different assemblies of three-layered cross tests were used to calibrate the SPR model for three-layered FDS connections. All models were validated by simulations of the lap-joint and peeling tests. A component test was performed to validate the two-layered macroscopic models for complex loading situations.

In the single-connector tests, shear-dominated loading situations generally produced higher forces than tension-dominated. Failure in the connections was mostly caused by pull-out from the bottom sheet. For the three-layered crosses and lap-joint specimens failure due to fracture of the screw itself, near the screw-head, was observed. In the component, all screws experienced both rotation and one-sided thread stripping.

The spotweld model was able to represent the stiffness and maximum force in some tests, but failure occurred too early in all simulations. The macroscopic model developed for SPR connections generally gave a good representation of the results, except under-predicting the force in peeling. The macroscopic model of the three-layered specimens showed some acceptable results, but under-estimated the forces in peeling, and over-estimated both force and displacement for the lap-joint. The macroscopic models gave an acceptable representation of maximum force in the component test, but were not able to accurately represent the stiffness observed in the experiments.

To develop a macroscopic model for FDS more work is necessary. The SPR model seems reliable for two-layered connections, but a model for three-layered connections requires further calibration, especially for shear-dominated loading cases. The spotweld model shows promising results, but further optimisation of the parameters must be conducted to conclude.

Samandrag

Denne oppgåva tek for seg ein eksperimentell og numerisk studie av åtferd og modellering av sambindingar med sjølvborande skruar (FDS) under varierande kvasi-statiske lastkombinasjonar. Åtferd og brot i sambindingane vart nøye undersøkt ved hjelp av ulike kombinasjonar av plater skrudde saman med ein enkel sjølvborande skrue. Ein komponent sett saman av to aluminiumsprofilar og seks skruar vart også testa.

Sambindingar av både to og tre aluminiumplater skrudde saman med ein enkel skrue vart testa. Det vart utførd krysstestar i tre lastretningar, testar på overlappa sambindingar og skrelletestar for sambindingar av både to og tre plater. Krysstestane av to plater vart brukte til å kalibrera to ulike makroskopiske modellar; den fyrste var ein punktsambindingsmodell som er utvikla for sjølvpenetrerande naglar (SPR), medan den andre var ein materialmodell utvikla for punktsveisar. To ulike samansetjingar av trelags krysstestar vart nytta til å kalibrera punktsambindingsmodellen for trelags sambindingar med sjølvborande skruar. Alle modellane vart validerte ved simuleringar av testane med overlappa sambindingar og skrelletestane. Ein test av komponenten vart utførd for å validera modellane i ein kompleks lastsituasjon.

Høgare krefter vart observerte i skjærdominerte lasttilfelle enn i dei strekkdominerte. Brot i sambindingane oppstod stort sett ved utdraging frå botnplata. For trelags kryss og overlappa sambindingar braut sjølve skruen i avskjæring.

Materialmodellen for punktsveis skildrar elastiske eigenskapar og maksimal kraft med akseptabel presisjon, men brot oppstod for tidleg i alle testane. Punktsambindingsmodellen for naglar synte gode resultat, utanom skrelletesten, der modellen ikkje evna å skildra maksimal kraft. Den makroskopiske modellen for sambindingar av tre plater evna ikkje å skildra maksimal kraft i skrelletesten, og overestimerte både kraft og forskyving i den overlappa sambindinga. For komponenten synte begge modellane akseptabel maksimal kraft, men ingen av dei evna å skildra dei elastiske eigenskapane som vart observerte i forsøka.

Meir arbeid er naudsynt for å utvikla ein makroskopisk modell for sjølvborande skruar. Punktsambindingsmodellen for naglar gjev gode resultat for sambindingar med to plater, men vidare kalibrering må utførast for sambindingar av tre plater. Materialmodellen for punktsveis synte lovande resultat, men ei meir omfattande optimalisering må gjennomførast før ein kan anvenda eller avskriva modellen.

Contents

ix

x

List of Tables

List of Figures

xiv

Chapter 1

Introduction

Flow-Drilling Screws (FDS) are widely used to join parts in modern car structures. Finite element simulations of connections that represent physical behaviour well are vital for the automotive industry. The goal of this master's thesis is to contribute to the development of a reliable and accurate numerical model for FDS for use in large-scale finite element analyses.

Many studies have been conducted on the mechanical behaviour of connections. Connection possibilities in cold-formed steel including mechanical fasteners, adhesive bonding and welding were investigated by Tomà et al. [1]. Pedreschi [2] did a study on the potential of press-joining in cold-formed steel structures, by performing lap shear and bending tests on connections with different fasteners. Comparative investigations of different mechanical fasteners have been performed, containing clinching, self-piercing rivet (SPR), pop rivet, self-tapping screw, mono- and bi-component blind rivets, and circular press-joints [3, 4]. Spot welded connections have been extensively investigated [5–10] both experimentally and numerically. The last decade many studies have been conducted on SPR connections. Porcaro et al. [11–15], investigated joining of aluminium using SPR, examining the influence of material properties, plate thickness and loading conditions. They used some of the results to obtain parameters for a numerical model for the connection in the element code LS-DYNA. Static and dynamic component tests were used to validate the model. Sun et al. [16–18] studied fatigue and dynamic strength of SPR connections joining similar and dissimilar metals. However, only a few studies have been conducted for screwed connections [1, 3, 19].

1

Sønstabø and Holmstrøm [19] recently conducted a study on two-layered FDS connections where sheets of aluminium alloy 6016 in the T4 condition were joined, and compared with SPR connections. The ability of a macroscopic model to describe the behaviour of the connections was assessed. They found that FDS connections behave in a similar manner as SPR connections. The macroscopic model was promising in some loading modes, but was not able to describe mixed tensile and shear loadings. This thesis is based on their work, further investigating the FDS connection. In this work connections with dissimilar materials are investigated, and both two- and three-layered connections are considered. To the author's extent, no work on three-layered FDS connections has been published in the open literature.

Several ways of modelling point-connectors for use in large-scale finite element analyses with shell-element based models exists. Node-to-node constraints, node-to-surface and surface-to-surface constraining by contact formulations, discrete elements, beam elements and brick elements are all used for modelling connections [20]. These methods are simplified and not flexible enough to capture the complex behaviour of the SPR and FDS connections, which are dependent on sheet properties, load direction and the type of connector.

Two different ways to model FDS were investigated in this thesis. The first is a point-connector model proposed by Hanssen et al. [20] for self-piercing rivets. The model has been used in some studies about the behaviour of self-piercing rivets [19, 21], and showed good results. The second way to model the connections is a material model developed to represent spot welds [22, 23]. It has not been used extensively in the open literature, and information about the application of the model and the parameters used are sparse. Sommer et al. [24] investigated modelling of self-piercing riveted connections using implemented models in LS-DYNA, and found promising results using this model. It has been an objective in this work to investigate some of the parameters used, and to see if the model can be used to represent FDS connections.

An extensive experimental investigation on the behaviour and fracture of FDS connections under different loading conditions was performed. The experimental program was divided into three different parts. Firstly, material tests of the aluminium alloy used in the connections were performed. The aluminium alloys used in the thesis have to some extent been described in earlier work [25–27]. An 18 parameter yield function, proposed by Barlat et al. [28] was used with the 7 parameter Voce isotropic hardening rule to simulate the material behaviour. The second part consisted of experimental testing of two- and

three-layered FDS connections. The results from the two-layered cross tests were used to calibrate the proposed macroscopic models. The two-layered peeling and lap-joint tests were used for validation. For the three-layered cross tests, only the SPR point-connector model was calibrated. The three-layered peeling and lap-joint tests were used to validate the model. Finally, a component test was performed. The test was used to validate the combined material and two-layered point-connector models for a complex loading situation. The component test was inspired by the work of Hoang et al. [21], that used a similar test setup and the point-connector model proposed by Hanssen et al. [20].

Some of the work performed by Sønstabø and Holmstrøm [19] have been used as a basis for the work in this thesis. The material model for the aluminium alloy 6016 T4 developed in their thesis is used for the material in this work. All work in this thesis is related to Flow-Drilling Screws. Results from this study may be used in development of point-connector models.

Chapter 2

Theory

In this chapter relevant theory for the master's thesis is presented. First, the use of Flow-Drilling Screws (FDS) in the automotive industry is described. Then the different models used to simulate screwed connections in this thesis are presented. The material model used and its parameters are described, before the theory part is concluded with an introduction to the use of Digital Image Correlation (DIC).

2.1 Connections

In this section some commonly used joining techniques in the automotive industry are briefly presented, before the FDS is presented more in detail. When car manufacturers pursue lighter cars, lighter and thinner materials are essential. Based on what properties that are necessary, different materials are used in different places in the car body. Fig. 2.1 shows the different materials used in the body of an Audi TT Coupé '07. This kind of assembly demands a high focus on what connections that should be used to join the different parts of the body.

A number of joining techniques are used in joining of the body parts in the manufacturing of a car. Fig. 2.2 shows different joining techniques used in the Audi A8'10. All techniques have different advantages and disadvantages. The presentation of different joining techniques is mostly based on [29].
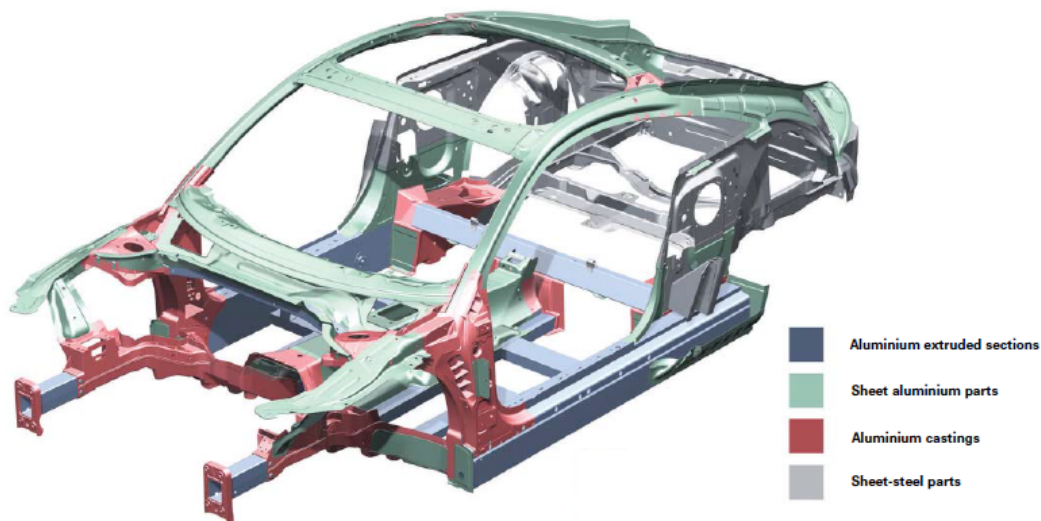
Figure 2.1: Overview of different materials in an Audi TT Coupé '07 [30].

Welding is one of the most common joining techniques used in the automotive industry. Some different welding techniques, including some advantages and disadvantages are presented in the following section. Metal Inert Gas (MIG) welding is a commonly used welding technique that produces high-strength joints with one-sided access, but at the cost of high temperature and relatively slow process speed. Resistance spot welding is another commonly used technique. Disadvantages with this technique is low electrical and thermal resistance, and the need for two sided access. Laser welding is a technique where a laser beam provides a concentrated heat source, allowing for narrow and deep welds. Laser welding only requires one-sided access, creates high static and dynamic strength connections, and is suitable for large-scale production. The main disadvantages of the laser welding are high investment and running costs [29].

Adhesive bonding can be used supplementary to other joining techniques, for instance punch riveted joints, FDS and resistance spot welds. The adhesive improves joint strength and is noise reducing. It is also effective for corrosion protection, as the materials in the connection are superficially insulated.

Mechanical fastening techniques include punch riveting, solid punch riveting, screwing, bolting, clinching and press joining. In clinching, metal sheets are joined by being clamped between a die and a blank holder. The sheets are pushed down into the die to form an interlocking joint. This technique is not as strong as other connections. Solid punch riveting involves the use of solid aluminium or coated stainless steel rivets. The rivet is

punched through both sheets to be joined. Solid rivets can be reworked mechanically unlike punch rivets, but at the cost of inferior strength. Punch riveting has become one of the principal techniques in aluminium joining in cars. It can be used for joining materials of both aluminium and steel, and combinations of both different material and sheet thickness [30]. Other advantages include high strength, no need for pre-drilling, water- and air tightness, and no thermal influence [31].
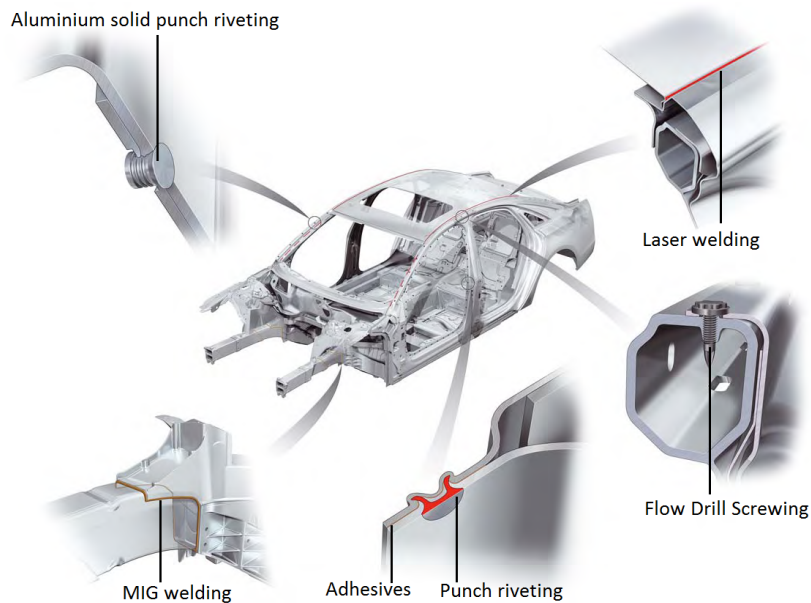
Figure 2.2: Joining techniques used in the manufacturing of the Audi A8'10 [32].

In this thesis FDS connections are investigated. Advantages of this technique include the possibility of joining dissimilar materials, one-sided assembly and little need for pre-preparations [30]. The connection manifests high shear, pull-out and torque capacity, and the screw can also be removed or replaced in service workshops, at a low overall joint cost [33].
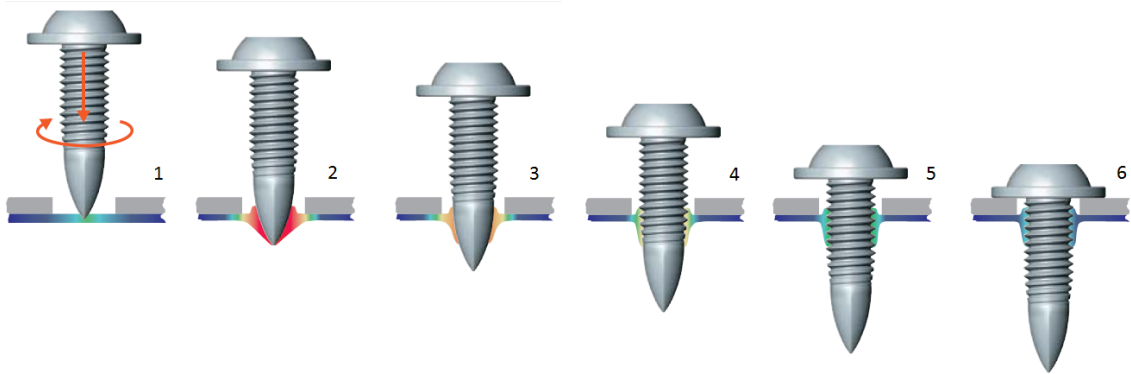
Figure 2.3: Assembly of Flow-Drilling Screws [33].

The different stages of the FDS assembly are shown in Fig. 2.3. The assembling is auto-mated, resulting in a fast and precise process. The stages are listed below [33]:

1. Warming the sheet metal by end load and high rotational speed

2. Penetration into the material

3. Forming of the through draught

4. Chipless forming of female machine thread

5. Engagement of full threads

6. Tightening with the pre-set torque

2.2 Connector models

Two different macroscopic models were used to simulate the experiments in this thesis. The first model used herein was proposed by Hanssen et al. [20], which is a model explicitly developed for self-piercing rivet connections, for use in large-scale finite element crash simulations. The model is a resultant-based point-connector model developed to represent the behaviour of a self-piercing rivet connection under any loading condition. Earlier work indicates that the model also can be suitable for FDS connections [19]. This model is denoted *CONSTRAINED_SPR2 in LS-DYNA [34]. Throughout this thesis, the model is referred to as *the spr2 model*. The second model that is used in this thesis is a material model developed for spot welds. The model is denoted *MAT_SPOTWELD

in LS-DYNA, and will be referred to as *the spotweld model* in this thesis. In the following, the theoretical foundation of the two models is presented.

2.2.1 The spr2 point-connector model

A node set is defined as the centre of the connection, as shown in Fig. 2.4. The algorithm of the point-connector model searches for and locates relevant nodes on the opposing shell segments within a user defined domain-diameter. Forces and moments are transferred between the nodes on opposing shell segments, and computed by a local model for each time step. This model use parameters that are identified by a reverse engineering approach, which means that the model parameters are iteratively changed to fit the experimental results [20].
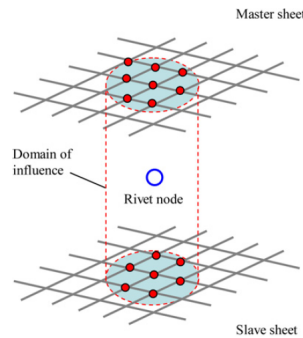
Figure 2.4: Rivet node between master and slave sheet [20].

Fig. 2.5a shows an illustration of a rivet that is about to be torn out of the bottom plate. All considerations in the model is in the plane of maximum opening, defined by the normal vector $\hat{\boldsymbol{n}}_0 = \hat{\boldsymbol{n}}_s \times \hat{\boldsymbol{n}}_m$, where $\hat{\boldsymbol{n}}_s$ is normal vector of the slave sheet, and $\hat{\boldsymbol{n}}_m$ is the normal vector of the master sheet. Fig. 2.5b and Fig. 2.5c show the kinematic of the SPR connection. The tangential unit normal vector of the rivet is defined by $\hat{\boldsymbol{n}}_t = \hat{\boldsymbol{n}}_0 \times \hat{\boldsymbol{n}}_m$. Fig. 2.5d shows the forces acting on the connector in the plane of maximum opening. The moment acting on the master sheet, M_m, must be balanced by the moment working on the slave sheet, M_s, by the following equation:

$$M_m + M_s = \frac{h_m + h_s}{2} f_t,$$ (2.1)

where h_m is the thickness of the master sheet, h_s the thickness of the slave sheet and f_t is the shear force acting on the rivet. For pure normal and pure shear deformation the following local force-deformation relationship is defined:

$$\frac{f_n}{f_n^{max}} = \frac{\delta_n}{\eta_{max}\delta_n^{fail}}\hat{f}_n(\eta_{max}) \tag{2.2}$$

and

$$\frac{f_t}{f_t^{max}} = \frac{\delta_t}{\eta_{max}\delta_t^{fail}}\hat{f}_t(\eta_{max}), \tag{2.3}$$

where f_n^{max} and f_t^{max} are the maximum rivet forces occurring during pure normal and shear deformation, respectively. Local deformation in pure normal and shear loading at failure are denoted δ_n^{fail} and δ_t^{fail}. The damage measure, η_{max}, is properly defined by Eq. (2.6) through Eq. (2.10). The dimensionless force-displacement relationships $\hat{f}_n(\eta_{max})$ and $\hat{f}_t(\eta_{max})$ are defined by

$$\hat{f}_n(\eta_{max}) = \begin{cases} 1 - \left(\frac{\xi_n - \eta_{max}}{\xi_n}\right)^8 & \text{for} \quad \eta_{max} \leq \xi_n \\ 1 - \frac{\eta_{max} - \xi_n}{1 - \xi_n} & \text{for} \quad \eta_{max} > \xi_n \end{cases} \tag{2.4}$$

and

$$\hat{f}_t(\eta_{max}) = \begin{cases} 1 - \left(\frac{\xi_t - \eta_{max}}{\xi_t}\right)^8 & \text{for} \quad \eta_{max} \leq \xi_t \\ 1 - \frac{\eta_{max} - \xi_t}{1 - \xi_t} & \text{for} \quad \eta_{max} > \xi_t \end{cases} \tag{2.5}$$

Here ξ_n and ξ_t define the region where softening starts.

(a) Plane of maximum opening.

(b) Simplified SPR configuration.

(c) Deformation measures of the connector model.

(d) Forces acting on the connector in the plane of maximum opening.
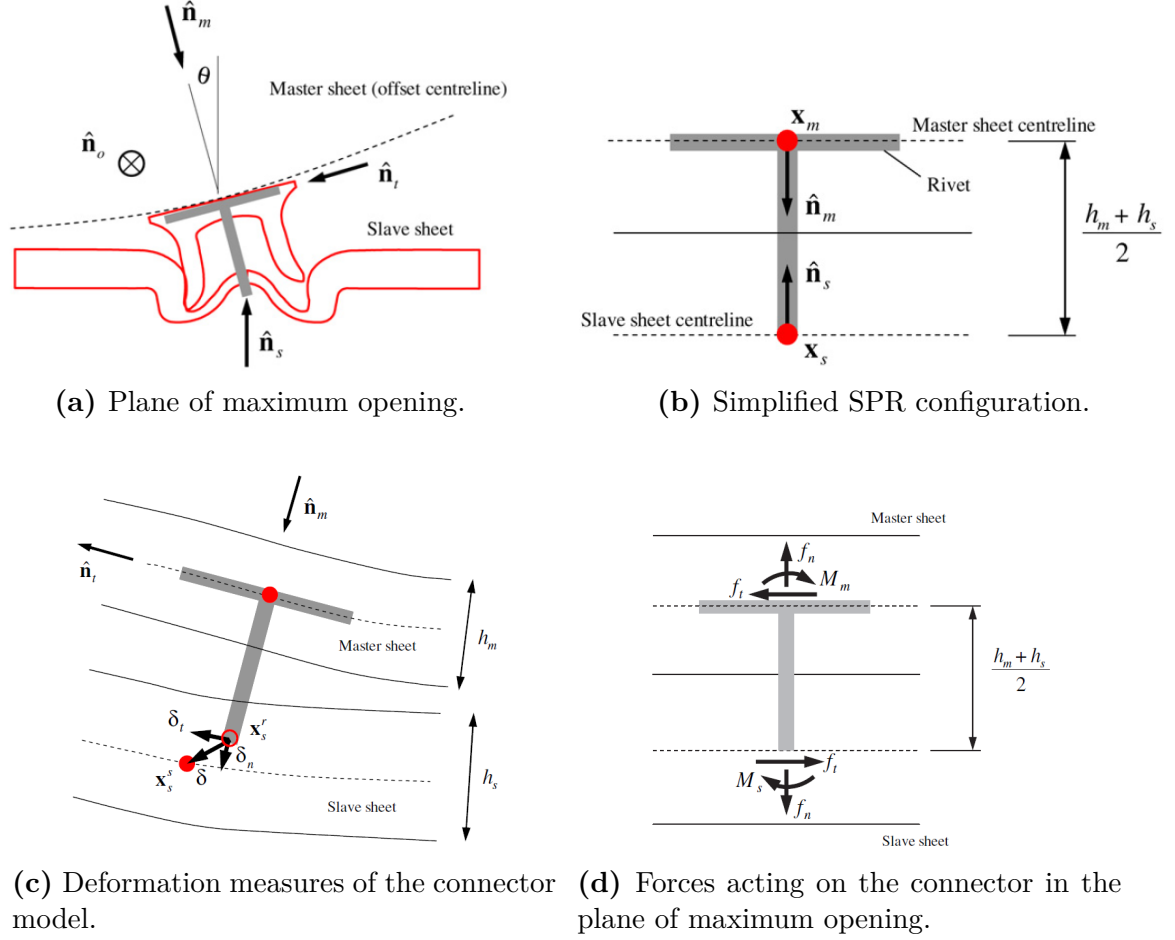
Figure 2.5: Illustration of the SPR configuration [20].

For pure normal or pure shear loading η_{max} can be illustrated by Fig. 2.6. Current maximum normal and shear local displacement at any given time is denoted δ_n^{max} and δ_t^{max}. For pure normal loading $\eta_{max} = \frac{\delta_n^{max}}{\delta_n^{fail}}$ and for pure shear loading $\eta_{max} = \frac{\delta_t^{max}}{\delta_t^{fail}}$, indicating that η_{max} grows from 0 to 1. Monotonic loading at all times is defined by $\delta_n = \delta_n^{max}$ and $\delta_t = \delta_t^{max}$ for pure normal and shear loading, respectively. From Eq. (2.2) and Eq. (2.3) it can be seen that $\frac{\delta_n}{\eta_{max}\delta_n^{fail}}$ and $\frac{\delta_t}{\eta_{max}\delta_t^{fail}}$ are unity for monotonic loading in pure normal or shear loading, respectively, and Eq. (2.4) and Eq. (2.5) will provide the capacities directly. For non-monotonic loading conditions, such as unloading, $\frac{\delta_n}{\eta_{max}\delta_n^{fail}}$ and $\frac{\delta_t}{\eta_{max}\delta_t^{fail}}$ will provide a linear force-displacement relationship, as seen in Fig. 2.6.

(a) Normal deformation.

(b) Shear deformation.
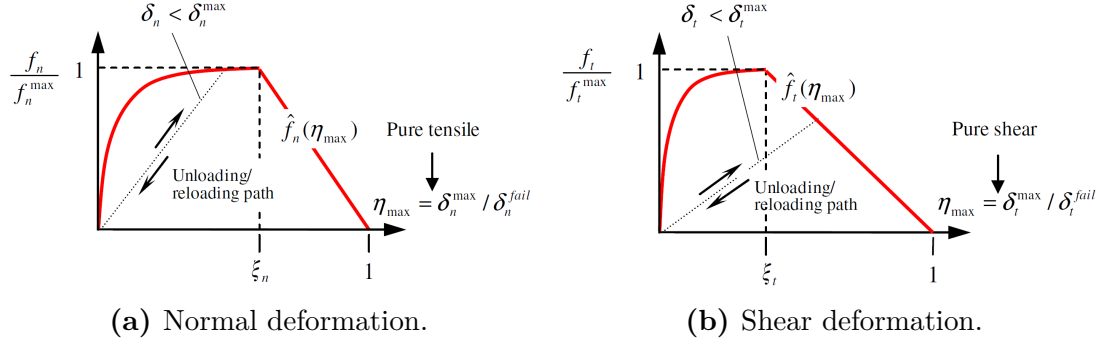
Figure 2.6: Local force-displacement relationship for pure normal and shear deformation [20].

The damage measure, η_{max} is calculated for each time step as

$$\eta_{max}(t) = \max(\eta(t)), \tag{2.6}$$

where η is a dimensionless effective displacement measure. The definition of effective displacement measure is then defined as

$$\eta = \left[\xi + \frac{1-\xi}{\alpha}\right]\sqrt{\left(\frac{\delta_n}{\delta_n^{fail}}\right)^2 + \left(\frac{\delta_t}{\delta_t^{fail}}\right)^2}. \tag{2.7}$$

Eq. (2.7) is illustrated in Fig. 2.7. α is a dimensionless model parameter and ξ is a directional scale factor on effective displacement measure, defined by

$$\xi = 1 - \frac{27}{4}\left(\frac{2\theta}{\pi}\right)^2 + \frac{27}{4}\left(\frac{2\theta}{\pi}\right)^3, \tag{2.8}$$

where θ is the loading angle given by

$$\theta = \arctan\left(\frac{\delta_n}{\delta_t}\right). \tag{2.9}$$
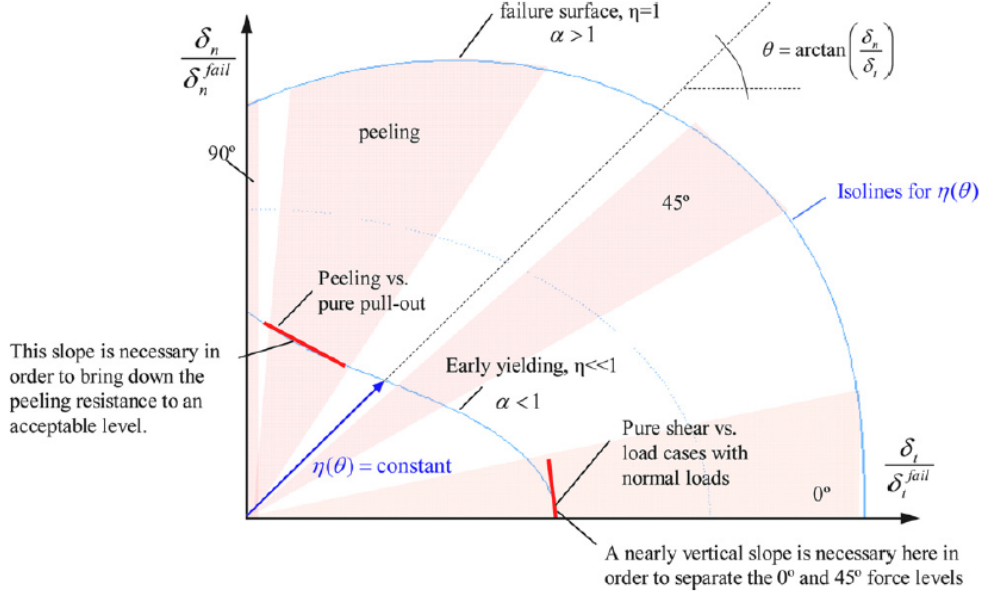
Figure 2.7: Discussion of effective displacement measure [20].

The damage driven model parameter α ensures that the loading angle dependency is damage dependent, which according to Hanssen et al. is required for self-pircing rivet connections [20]. The parameter is defined by:

$$\alpha = \begin{cases} \frac{\xi_t - \eta_{max}}{\xi_t}\alpha_1 + \frac{\eta_{max}}{\xi_t}\alpha_2 & \text{for} \quad \eta_{max} < \xi_t \\ \frac{1 - \eta_{max}}{1 - \xi_t}\alpha_2 + \frac{\eta_{max} - \xi_t}{1 - \xi_t}\alpha_3 & \text{for} \quad \eta_{max} \geq \xi_t \end{cases} \tag{2.10}$$

Here α_1 is the initial value of α, which grows to α_2 when $\eta_{max} = \xi_t$ and finally to α_3 when $\eta_{max} = 1$. The parameters α_1 and α_2 are corrections to bring down the force in peeling and oblique loading cases. The main effect of α_3 is to moderate the failure displacement in oblique loading directions. Failure is reached when $\eta_{max} = 1$, where Eq. (2.2) and Eq. (2.3) give no resistance for both the normal and shear component.

The two main principal features of the model included with the effective displacement measure are shown in Fig. 2.7. Firstly, it can be seen that the effective displacement measure is loading angle dependent. This means that the degree of damage occurring for a certain load angle can be controlled. Secondly, it can be seen that the load angle dependency is history dependent. This means that different force-displacement curves for various loading angles can be controlled at all stages of deformation.

Until reaching the effective displacement $\eta_{max} = \xi_t$, the moment is distributed equally

to the master and slave sides, as shown in Eq. (2.1). As damage grows, more and more moment is transferred from the slave to the master side, defined by

$$
M_m = \begin{cases} \frac{h_m+h_s}{4} f_t & \text{for} \quad \eta_{max} < \xi_t \\ \frac{h_m+h_s}{4} \left(1 + \frac{\eta_{max}-\xi_t}{1-\xi_t}\right) f_t & \text{for} \quad \eta_{max} \geq \xi_t \end{cases}
\tag{2.11}
$$

and

$$
M_s = \begin{cases} \frac{h_m+h_s}{4} f_t & \text{for} \quad \eta_{max} < \xi_t \\ \frac{h_m+h_s}{4} \left(1 - \frac{\eta_{max}-\xi_t}{1-\xi_t}\right) f_t & \text{for} \quad \eta_{max} \geq \xi_t \end{cases}
\tag{2.12}
$$

Eventually, the connection to the slave sheet becomes a moment free hinge. This concludes the presentation of the spr2 point-connector model. The parameters that will be obtained using reversed engineering are listed and described in Table 2.1.

Table 2.1: Model parameters of the spr2 point-connector model.

Parameter	Description
f_n^{max}	Maximum pure normal force
f_t^{max}	Maximum pure shear force
δ_n^{fail}	Deformation at failure for pure normal load
δ_t^{fail}	Deformation at failure for pure shear load
ξ_n	Start of softening for pure normal deformation
ξ_t	Start of softening for pure shear deformation
$\alpha1$	Initial value of the damage parameter α
$\alpha2$	Value of α when softening starts
$\alpha3$	Final value of α
d	Numerical diameter

2.2.2   The spotweld macroscopic model

The spotweld macroscopic model is a material model representing the connection using solid or beam elements, which are connected to the plates using tie constraints. The model is included in LS-DYNA using the keyword *MAT_SPOTWELD. It can be modelled using 1 to 16 elements, as shown in Fig. 2.8. For the contact to be robust and acceptably mesh independent, multiple elements are needed [23].

Figure 2.8: Different mesh configurations of the spotweld; 1, 4, 8 and 16 elements.

The spotweld model is represented by a set of material parameters. Mass density, ρ, Young's modulus, E, Poisson's ratio, ν, initial yield stress, σ_y and hardening modulus, E_t, define the material. In addition, several failure models are available. In this work, a resultant based failure criterion defined by

$$\left(\frac{max(N_{rr},0)}{N_{rrF}}\right)^2 + \left(\frac{N_{rs}}{N_{rsF}}\right)^2 + \left(\frac{N_{rt}}{N_{rtF}}\right)^2 + \left(\frac{M_{rr}}{M_{rrF}}\right)^2 + \left(\frac{M_{ss}}{M_{ssF}}\right)^2 + \left(\frac{M_{tt}}{M_{ttF}}\right)^2 = 1 \quad (2.13)$$

was chosen, where the numerators in the equation are the resultants calculated in the local coordinates of the cross section, and the denominators are model parameters [34]. The moment resultants in Eq. (2.13) are not represented in the failure criterion used in this thesis to reduce the number of variables in the failure criterion. The criterion can then be reduced to:

$$\left(\frac{N_{rr}}{N_{rrF}}\right)^2 + \left(\frac{N_{rs}}{N_{rsF}}\right)^2 + \left(\frac{N_{rt}}{N_{rtF}}\right)^2 = 0 \quad (2.14)$$

In addition to the failure function a failure strain, ϵ_{fail}, will fail the connection at a given plastic strain in an element. All model parameters are described in Table 2.2. The section is placed between the two plates it connects as shown in Fig. 2.9. The thickness of the connector is the average of the thickness of the two plates:

$$t_{connector} = \frac{t_{plate1} + t_{plate2}}{2} \quad (2.15)$$

The spotweld is tied to the sheets using the keyword *CONTACT_TIED_NODES_ TO_SURFACE_ID. Two contact constrains are used for each connection, one for each side of the connector.

Figure 2.9: Placement of connector between two shell sections.

The parameters that needs to be determined for the model are shown in Table 2.2. The parameters are determined using a reverse engineering approach. The model parameters are iteratively determined to fit the experimental results.

Table 2.2: Parameters used in the spotweld macroscopic model.

Variable	Keyword in input card	Description
ρ	RO	Mass density
E	E	Young's modulus
ν	PR	Poisson's ratio
σ_y	SIGY	Initial yield stress
E_t	ET	Hardening modulus
$\epsilon_f ail$	EFAIL	Effective plastic strain in weld material at failure.
N_{rr}	NRR	Axial force resultant at failure
N_{rs}	NRS	Shear force resultant at failure
N_{rt}	NRT	Shear force resultant at failure
M_{rr}	MRR	Torsional moment resultant at failure
M_{ss}	MSS	Moment resultant at failure
M_{tt}	MTT	Moment resultant at failure

2.3 Base materials

The base materials used in this work is aluminium alloy 6016 received as flat rolled plates in temper T4, and extruded profile of aluminium alloy 6063 in T6 condition. T4 is a condition where the material has been solution heat-treated and naturally aged. T6 has been solution heat-treated and artificially aged [35]. The chemical composition of the alloys according to [36] are shown in Table 2.3.

Table 2.3: Chemical composition of base materials.

Chemical element	AA6016 (wt%)	AA6063(wt%)
Si	1.0 - 1.5	0.20 - 0.6
Fe	< 0.50	< 0.35
Cu	< 0.20	< 0.10
Mn	< 0.20	< 0.10
Mg	0.25 - 0.6	0.45 - 0.9
Cr	< 0.10	< 0.10
Zn	< 0.20	< 0.10
Ti	< 0.15	< 0.10
Others	< 0.15	< 0.15
Al	Rem.	Rem.

2.4 Modelling of base material

In this section the theory relevant for modelling the base material is presented. Firstly, the chosen yield function is presented, before the work hardening parameters that were chosen for the material are presented. Finally, some aspects on the yield surface are discussed.

2.4.1 YLD-2004-18P anisotropic yield function

The Yld2004-18p rate independent yield function by Barlat et al. [28] was used to model the material in this thesis. The following analytical yield function ϕ was proposed:

$$
\begin{aligned}
\phi = \phi(\Sigma) = \phi(\tilde{S}', \tilde{S}'') = & |\tilde{S}'_1 - \tilde{S}''_1|^a + |\tilde{S}'_1 - \tilde{S}''_2|^a + |\tilde{S}'_1 - \tilde{S}''_3|^a \\
& + |\tilde{S}'_2 - \tilde{S}''_1|^a + |\tilde{S}'_2 - \tilde{S}''_2|^a + |\tilde{S}'_2 - \tilde{S}''_3|^a \\
& + |\tilde{S}'_3 - \tilde{S}''_1|^a + |\tilde{S}'_3 - \tilde{S}''_2|^a + |\tilde{S}'_3 - \tilde{S}''_3|^a,
\end{aligned}
\tag{2.16}
$$

where a is an exponent that determines the curvature of the function. $\tilde{S}'$ and $\tilde{S}''$ are

the principal values of the tensors $\tilde{s}'$ and $\tilde{s}''$ defined by two linear transformations on the stress deviator s:

$$\tilde{s}' = C's = C'T\sigma \tag{2.17}$$

$$\tilde{s}'' = C''s = C''T\sigma \tag{2.18}$$

Here σ is a matrix representation of the Cauchy stress tensor, T transforms the stress tensor to its deviator s and C' and C''' are transformation matrices containing the anisotropy coefficients, given by

$$C' = \begin{bmatrix} 0 & -c'_{12} & -c'_{13} & 0 & 0 & 0 \\ -c'_{21} & 0 & -c'_{32} & 0 & 0 & 0 \\ -c'_{31} & c'_{32} & 0 & 0 & 0 & 0 \\ 0 & 0 & 0 & c'_{44} & 0 & 0 \\ 0 & 0 & 0 & 0 & c'_{55} & 0 \\ 0 & 0 & 0 & 0 & 0 & c'_{66} \end{bmatrix}, \tag{2.19}$$

$$C'' = \begin{bmatrix} 0 & -c''_{12} & -c''_{13} & 0 & 0 & 0 \\ -c''_{21} & 0 & -c''_{32} & 0 & 0 & 0 \\ -c''_{31} & c''_{32} & 0 & 0 & 0 & 0 \\ 0 & 0 & 0 & c''_{44} & 0 & 0 \\ 0 & 0 & 0 & 0 & c''_{55} & 0 \\ 0 & 0 & 0 & 0 & 0 & c''_{66} \end{bmatrix}. \tag{2.20}$$

The 18 coefficients are calculated by minimising an error function, fitting the model to experimental data. The exponent a can be included in the optimisation, or be specified before optimisation. If $a = 2$ or $a = 4$, the yield function will reduce to Von Mises'. With $a = 1$ or a high value of a, the yield function corresponds to Tresca's yield function. Based on crystal plasticity, a value $a = 8$ was proposed for FCC materials, such as the 6063 extruded aluminium alloy [28]. The exponent a has therefore been given the value 8 in this thesis.

2.4.2 Voce isotropic hardening rule

The Voce rule shown in Eq. (2.21), is a common model used to include isotropic hardening and was adopted here. The yield stress, σ_0 and the constants Q_1, C_1, Q_2, C_2, Q_3 and C_3 are defined using experimental results.

$$\sigma_Y = \sigma_0 + \Sigma_{n=1}^3 Q_n[1 - \exp(-C_n \epsilon_p)] \tag{2.21}$$

2.4.3 Concerning the yield surface

Fig. 2.10a shows a yield surface with intersections for constant shear stress σ_{xy}. In Fig. 2.10b the same yield surface is plotted in the σ_{xy} vs. $\frac{\sigma_x + \sigma_y}{\sqrt{2}}$ plane with intersections planes with normal vectors along the line $\sigma_x + \sigma_y = 0$. The location on the yield surface for some common material tests are indicated on the figures. The reference direction for the material is in the x-direction.

(a) Intersections for constant shear stress σ_{xy}.

(b) Shear deformation.
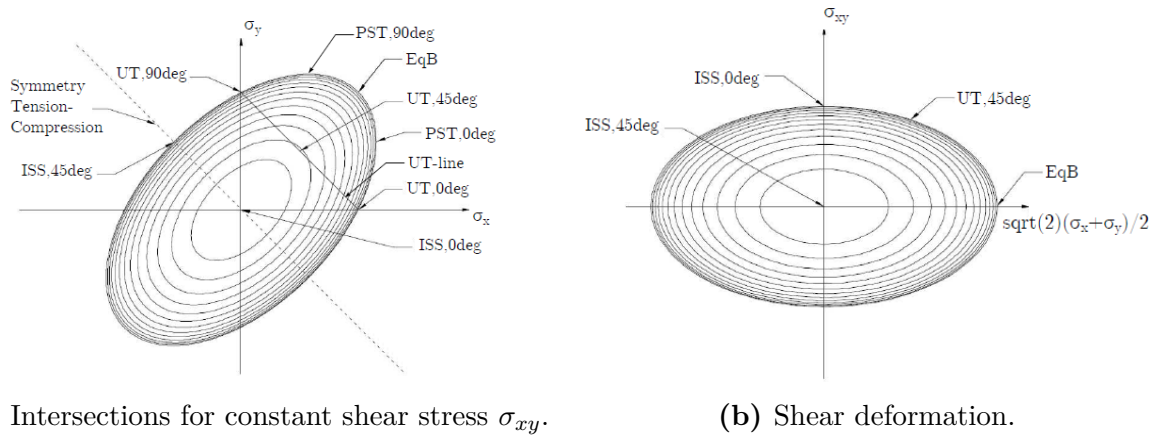
Figure 2.10: Different stress states on the yield surface. The material reference direction is the x-direction [19].

To calibrate the material model, strain ratios and flow stress ratios have to be calculated. The strain ratio, R_α, is calculated by the equation

$$R_\alpha = \left.\frac{\dot{\epsilon}_w^p}{\dot{\epsilon}_t^p}\right|_\alpha = \left.\frac{d\epsilon_w^p}{d\epsilon_t^p}\right|_\alpha = \left.\frac{\Delta\epsilon_w^p}{\Delta\epsilon_t^p}\right|_\alpha, \tag{2.22}$$

where $\dot{\epsilon}^p$ is the plastic strain rate, $d\epsilon^p$ is the infinitesimal plastic strain increment, and $\Delta\epsilon^p$ is the change in plastic strain measured in the uniaxial tensile tests. Notation w is used for strain in width of the specimen, t for the thickness, and α is the material direction in the specimen. The flow stress ratio, r_α, is calculated by the following equation:

$$r_\alpha(W^p) = \frac{\sigma_\alpha(W^p)}{\sigma_{ref}(W^p)}, \tag{2.23}$$

where σ_α is the stress in α direction, σ_{ref} is the stress in the reference direction and W_p is plastic work. The reference direction, 0-degree, is in the extruded direction of the alloy.

In the calibration of the material model the average values of the flow stress ratio, r_α^{avg}, is used. This is calculated by the equation

$$r_\alpha^{avg} = \frac{1}{W_{max}^p} \int_0^{W_{max}^p} r_\alpha(W^p)dW^p. \tag{2.24}$$

By preforming a disc compression test, information relevant for equibiaxial tension can be obtained [28]. The biaxial strain ratio, R_b is related to the gradient of the yield surface at the equi-biaxial point, denoted EqB in Fig. 2.10a. In order to determine the biaxial strain ratio the true principal strains under equibiaxial tension, ϵ_{11} and ϵ_{22} needs to be determined. The biaxial strain ratio was calculated by

$$R_b = \frac{\epsilon_{22}}{\epsilon_{11}}. \tag{2.25}$$

In this thesis, ϵ_{11} is chosen to be oriented in the extruded direction, while ϵ_{22} is oriented in the transverse direction. True strain in the thickness direction is denoted ϵ_{33}. The strains are calculated using Eq. (2.26) to Eq. (2.28), where D_0 and t_0 are original measures, and D_{ext}, $D_{transverse}$ and t are measures after compression of the disc.

$$\epsilon_{11} = \epsilon_{ext} = \ln\left(\frac{D_{ext}}{D_0}\right) \tag{2.26}$$

$$\epsilon_{22} = \epsilon_{transverse} = \ln\left(\frac{D_{transverse}}{D_0}\right) \tag{2.27}$$

$$\epsilon_{33} = \epsilon_t = \ln \left(\frac{t}{t_0} \right) \tag{2.28}$$

The principle of the disc compression test is shown in Fig. 2.11. The test is based on the assumption that plastic flow can be considered to be pressure independent. Frictionless uniaxial compression of a disc can be viewed as a combination of uniform pressure and equibiaxial stretching, where the uniform pressure does not affect the yield of the material. Thus, the plastic state in equi-biaxial tension and uniaxial compression are per assumption equivalent.

Since the plastic deformation of a metal is volume preserving, the sum of the true principal stains is supposed to be zero for a homogeneous deformation. The equation

$$\Sigma\epsilon_i = \epsilon_{11} + \epsilon_{22} + \epsilon_{33} = 0 \tag{2.29}$$

will be used as a control of the measurements. Results from others have shown that the sum usually equals a small positive percentage [28].
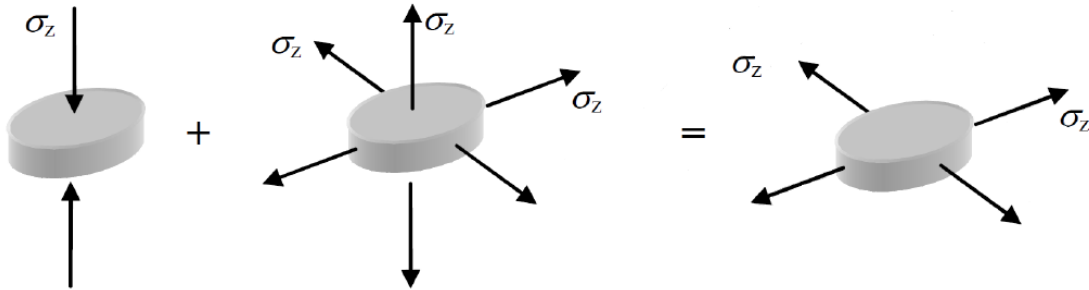
Figure 2.11: Disc compression test: test principle.

2.5 Digital Image Correlation

Digital Image Correlation (DIC) is an optical method to accurately measure changes in images in 2D and 3D. This is done by recording deformation and motion of a random grayscale pattern on a specimen surface before and after deformation of the body. To get accurate test results from the component tests, three-dimensional DIC was applied. To get familiar with the software and to obtain an extra validation, two-dimensional DIC was used on the ISS specimens. Using DIC, displacement fields were measured and strain

fields were calculated. The DIC measurements were used to compare with LS-DYNA simulations for validation.

For a thorough explanation of the theory behind, and use of DIC, the doctoral thesis by Fagerholt [37] or the work of Besnard et al. [38], which describe the method in detail, is recommended. A simplified description is given herein. Fig. 2.12a shows an example of a uniaxial tension test specimen with applied grey scale pattern and mesh for material point tracking. A principle sketch of the camera setup is shown in Fig. 2.12b. The log file from the experimental data is used as input in the DIC-analysis, thus making sure the time of each picture is registered correctly.

(a) Example of DIC mesh.

(b) Principle of DIC setup.
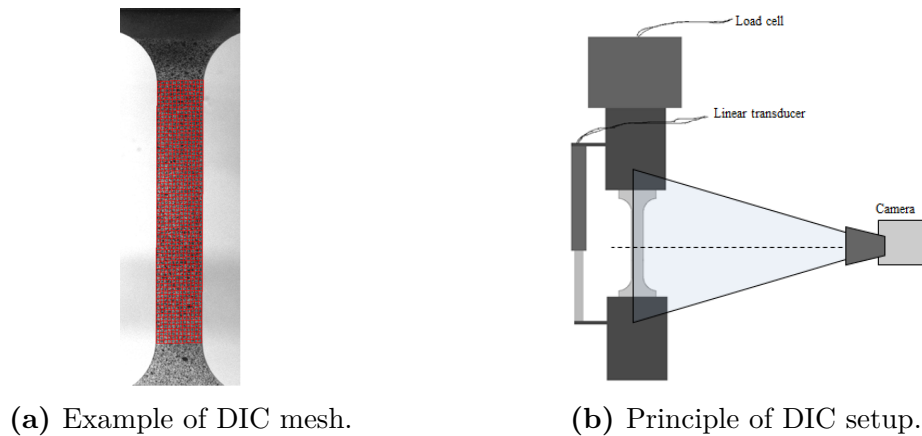
Figure 2.12: Example of mesh and setup for DIC [37].

For this introduction, only two-dimensional coordinates in the image plane will be referred to. Here, $\boldsymbol{X} = (X, Y)$ refer to the image coordinates in the reference configuration, $\boldsymbol{x} = (x, y)$ refer to the image coordinates in the current configuration, while $\boldsymbol{u} = (u, v)$ refer to the translation in horizontal and vertical direction, such that $\boldsymbol{u} = \boldsymbol{x} - \boldsymbol{X}$. The image from the deformed state (the current image) is denoted I_c, while the image from the undeformed state (reference image) is denoted I_r.

The mathematical formulation of DIC employs Newton-Raphson methods for optimisation. The correlation is carried out on a small rectangular region of an image, here called a subset. Deformation of the subset is given by six parameters, the translation of the centre point (u_c, v_c) as well as the first order displacement gradient $(\frac{\partial u}{\partial X}, \frac{\partial u}{\partial Y}, \frac{\partial v}{\partial X}, \frac{\partial v}{\partial Y})$ within the subset. The deformation parameters for a subset in the current image are found by minimising a certain correlation function F based on the difference in grayscale values between the reference image and the current image. Thus, the correlation function F is

used as the objective function in the Newton-Raphson optimisation.

The sum-of-squares of the grayscale differences within the subset is a correlation function, and is defined by

$$F = \sum_{i \in \Omega} (I_r(\boldsymbol{X}_i) - I_c(\boldsymbol{x}_i))^2, \tag{2.30}$$

where i denotes a specific pixel and Ω denotes the set of pixels within the subset at the reference configuration. The basic principle of the subset-based DIC approach is shown in Fig. 2.13. The figure shows the reference subset in the reference image I_r and the deformed subset in the current image I_c as well as the displacement (u_c, v_c) of the centre point of the subset.

(a) Reference stage.   **(b)** Updated stage.
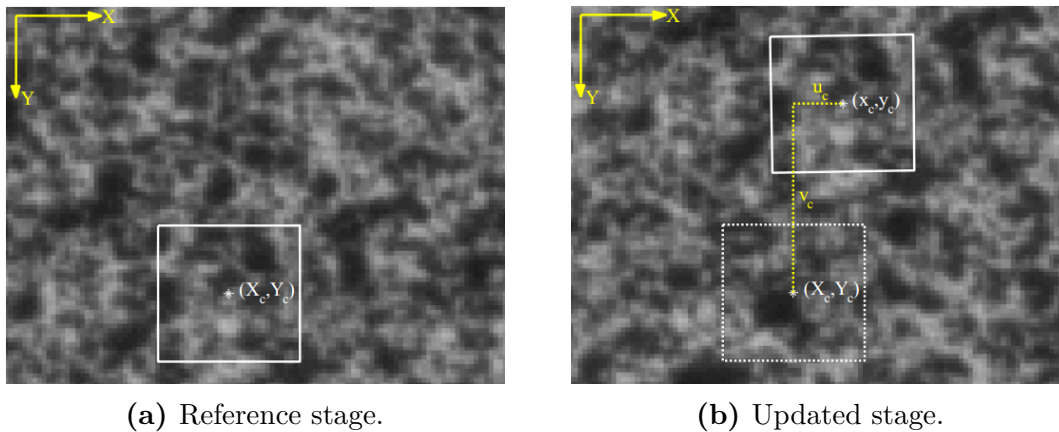
Figure 2.13: Principle of subset-based DIC [37].

Chapter 3

Experimental setup

In this chapter the experimental setup is presented in detail. Material tests were performed for the extruded AA6063 material. Single connector tests were performed with both two- and three-layered specimens. Finally, a component test was performed. The term single connector is used for connections where two or more aluminium plates are connected using a single FDS. The single connector and component specimens were assembled of both AA6063 T6 and AA6016 T4 material. All parts of the same aluminium alloy were made from the same batch. The plates made of AA6016 were machined from sheets with thickness 2 mm. The plates made of AA6063 were machined from hollow extruded sections with thickness 2 mm. All tests were carried out under quasi-static conditions.

Three different single connector tests were performed for both two- and three-layered connections. The term two-layered connection is used when the screw connects two aluminium plates, three-layered is used for the connection of three plates. The test program consisted of cross, peeling and lap-joint tests. The cross tests were applied pure normal, pure shear and a combination of normal and shear force to calibrate the macroscopic models, and to investigate the behaviour of the connection. Lap-joint and peeling tests were performed to validate the models. The component test was performed to validate the models for a complex loading situation. All connections were assembled by Honda R&D Americas, Inc. All tests were conducted using standard Instron and Zwick tensile test machines. Detailed descriptions of the test setups are presented in Appendix A.

3.1 Material tests

To be able to create a reliable material model, experimental data was needed. The results from uniaxial tension and disc compression tests were used to calibrate the material model. Plane strain tension and in-plane single shear were used for validation.

A number system was created to distinguish between the tests. The numbers are written on the form XX6063_YY_ZZ. XX represents the test type; UT for uniaxial tension, PST for plane strain tension and ISS for in-plane single shear, disc for the disc compression tests and screw for the uniaxial tension tests of the screw material. 6063 refer to the aluminium alloy. YY represents the angle between the extruded direction and the longitudinal direction of the specimen. ZZ represents the repetition number. As an example, UT6063_45_02 is the second uniaxial tension test specimen cut with an angle of 45 degrees. Length measurements are given in mm for all figures. An overview of the material tests is presented in Table 3.1.

Table 3.1: Overview of material tests.

Test type	Material angle	Repetitions	Date
UT	0, 15, 30, 45, 60, 75, 90	3	10.02.2014
PST	0	3	10.02.2014
ISS	0	3	10.02.2014
Disc	0	6	11.02.2014
Screw	0	10	29.04.2014

3.1.1 Uniaxial tension

The nominal geometry of the test specimen is shown in Fig. 3.1a. Measurements done before and after the tests are presented in Table B.1. The tests were conducted with a crosshead velocity of 1.2 mm/min, to ensure quasi-static conditions. For UT6063_00_01, a gauge length of 10 mm was set on the extensometer. For the rest of the UT tests, a 15 mm gauge length was chosen. The test setup is shown in Fig. 3.1b.
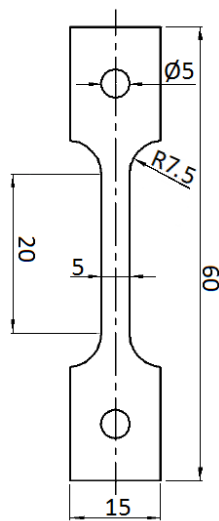
(a) Geometry of UT test specimen.　　　**(b)** UT test setup.

Figure 3.1: Geometry and setup for the uniaxial tension tests.

3.1.2 Plane strain tension

The nominal geometry of the test specimen is shown in Fig. 3.2a. Measurements of the specimens are presented in Table B.2. The tests were conducted with a crosshead velocity of 0.6 mm/min, to ensure quasi-static conditions. The gauge length of the extensometer was 20 mm. Measurements were conducted to ensure that an equal part of 20 mm of the specimens were clamped in each test. The setup for the PST tests is shown in Fig. 3.2b.

3.1.3 In-plane single shear

The nominal geometry of the test specimen is shown in Fig. 3.3a. Measurements of the specimens are presented in Table B.3. The specimens were applied a coating of black and

white paint using an airbrush, for the application of DIC. A Prosilica GC2450 camera was used, taking 5 pictures/second. All tests were conducted with a crosshead velocity of 0.6 mm/min, which ensured quasi-static conditions. The gauge length of the extensometer was 30 mm. The test setup is shown in Fig. 3.3b.
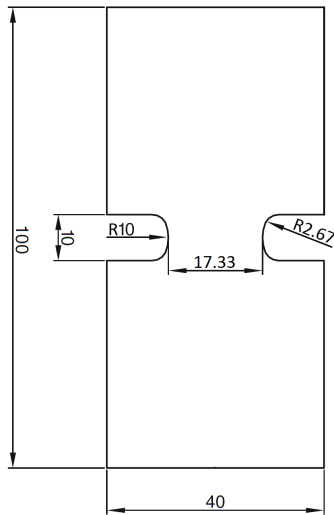
(a) Geometry of PST test specimen.   **(b)** PST test setup.
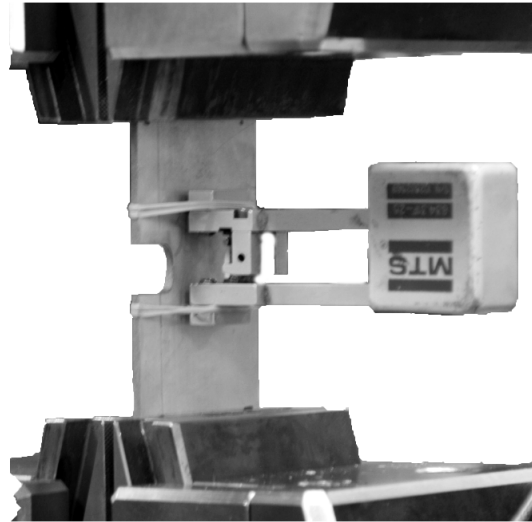
Figure 3.2: Geometry and setup for the plane strain tension tests.
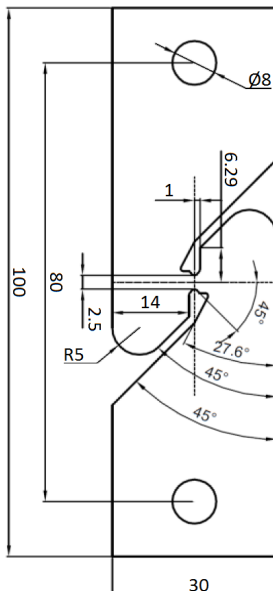
(a) Geometry of ISS test specimen.   **(b)** ISS test setup.
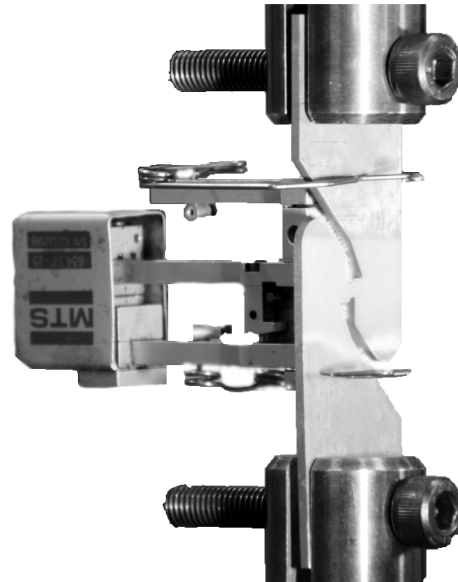
Figure 3.3: Geometry and setup for the in-plane single shear tests.

3.1.4 Disc compression

The discs had a nominal diameter of 14 mm, and a thickness of 2 mm. Measurements done before and after the tests are presented in Table B.4. All disc compression tests were conducted with a loading rate of 20 kN/min up to 70 kN, where the force was kept constant for 1 minute. To avoid friction in the transverse direction of the disc, a lubricant was applied on both sides of each specimen before testing. The tests setup from the disc compression tests is shown in Fig. 3.4b
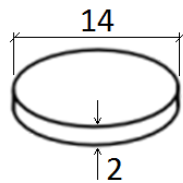
(a) Geometry of the disc specimen.   **(b)** Disc compression test setup.

Figure 3.4: Geometry and setup for the disc compression tests.

3.1.5 Uniaxial tension test of screws

The screws used for the single-connector and component tests were tested in uniaxial tension. Axisymmetric uniaxial test specimens were machined from screws with nominal geometry as shown in Fig. 3.5a. The measured diameter of each test specimen is presented in Table B.5. All tests were conducted with a cross head velocity of 0.66 mm/min, which ensured quasi-static conditions. The gauge length on the extensometer was 8.5 mm. The test setup is shown in Fig. 3.5b.
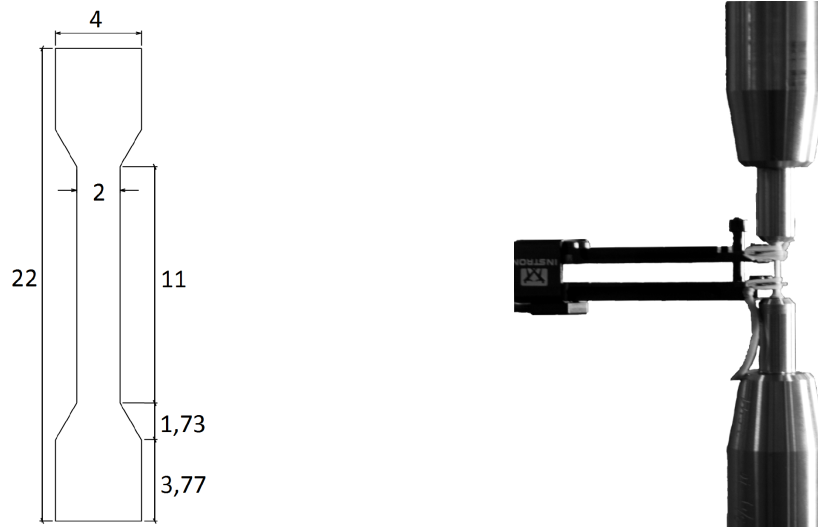
(a) Geometry of the UT screw specimen.

(b) UT screw test setup.

Figure 3.5: Geometry and setup for the uniaxial tension screw tests.

3.2 Single connector tests

To be able to obtain and validate a reliable point connector model, and to investigate the experimental behaviour, connector experiments were conducted. A number system was created to distinguish between the tests. The numbers are written on the form XX_YY_ZZ. XX represents the test type; C for cross, LJ for lap-joint and P for peeling tests. The three-layered lap-joint and peeling tests are named 3LJ and 3P, respectively. The three-layered cross tests had two different configurations. The configuration with two top plates was named C21, while the configuration with two bottom plates was called C12. YY represents the loading angle. Pure pull-out is represented by 0, while 90 represents pure shear loading of the specimen. ZZ represents the repetition number. As an example, C12_45_02 is the second cross test specimen with one top plate and two bottom plates, loaded at an angle of 45 degrees.

In the figures with nominal dimensions, the extruded/rolled direction of each aluminium plate is shown with stippled lines. The AA6016 sheets are presented in blue, while the AA6063 extrusions are green. All AA6016 sheets were pre-drilled, while all AA6063 extrusions were pierced with the FDS. Measured geometry of every specimen is listed in Appendix B. Measurements $m1$ and $m2$ in the tables correspond to the placement of the screw in each connection. Length measurements are given in mm for all figures. An

overview of the connector tests is presented in Table 3.2.

Table 3.2: Overview of connector tests.

Test type	Loading direction	Repetitions	Date
LJ	0	4	03.03.2014
3LJ	0	3	03.03.2014
P	0	5	03.03.2014
3P	0	4	03.03.2014
C	0, 45, 90	5	03.03.2014
C12	0, 45, 90	5	04.03.2014
C21	0, 45, 90	5	05.03.2014
Component	0	3	27.03.2014

3.2.1 Two-layered cross

The top parts of the cross specimens were cut in the transverse direction, while the bottom parts were cut in the longitudinal direction, as seen by the stippled lines in Fig. 3.6. Nominal dimensions of the plates are shown in Fig. 3.6. Nominal values of $m1$ and $m2$ were 20 mm and 60 mm, respectively. The holes in the specimens were needed to clamp the specimen properly. To obtain the different loading modes a special designed clamping rig was used. The principle of the rig is shown in Fig. 3.7a, and a picture of the setup is shown in Fig. 3.7b. By rotating the lock plate the loading angle was altered. When the ends of the lock plate were fastened to the pull bar, pure tension or pure shear forces could be applied to the specimens. To get a combination of tensile and shear forces, the loading angle was set to 45 degrees. The tests were conducted with a cross head velocity of 10 mm/min, to ensure quasi-static conditions. Measurements of each specimen as well as average values are shown in Table B.6.
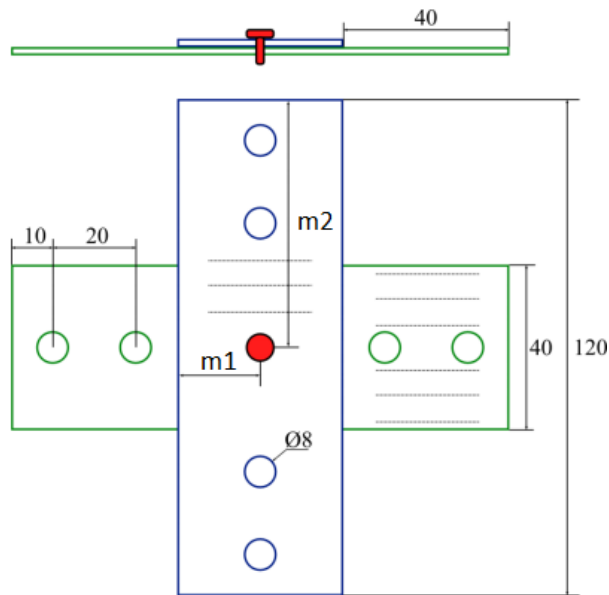
Figure 3.6: Nominal dimensions of the single cross specimen.

(a) Principle of the cross test rig.
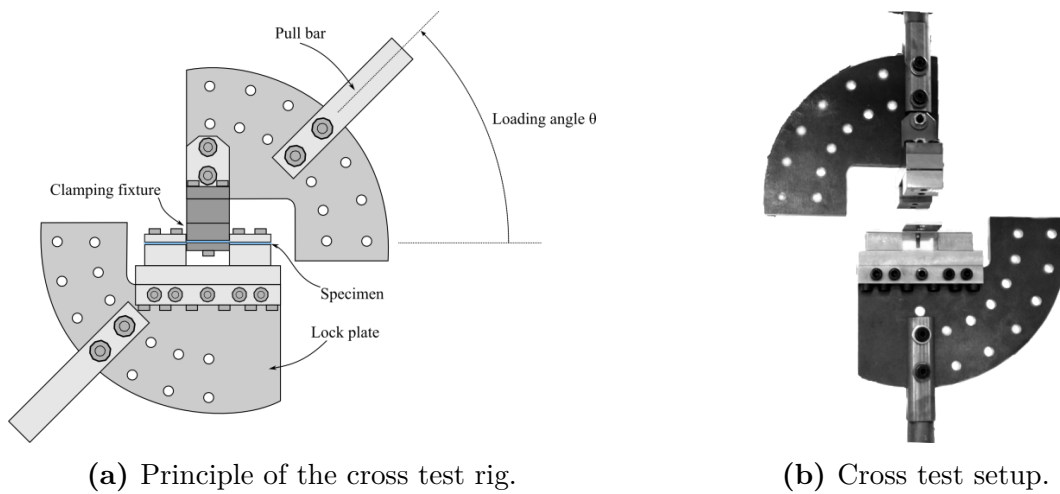
(b) Cross test setup.

Figure 3.7: Principle and setup for the cross tests.

3.2.2 Two-layered lap-joint

The nominal geometry of the test specimen is shown in Fig. 3.8a. Nominal values of $m1$ and $m2$ were both 20 mm. The tests were conducted with a cross head velocity of 10 mm/min, to ensure quasi-static conditions. To ensure a rigid setup, 40 mm of both ends of the specimen were clamped in each test. The clamping of the specimen is shown in Fig. 3.8b. Measurements of each specimen as well as average values are shown in Table B.7.
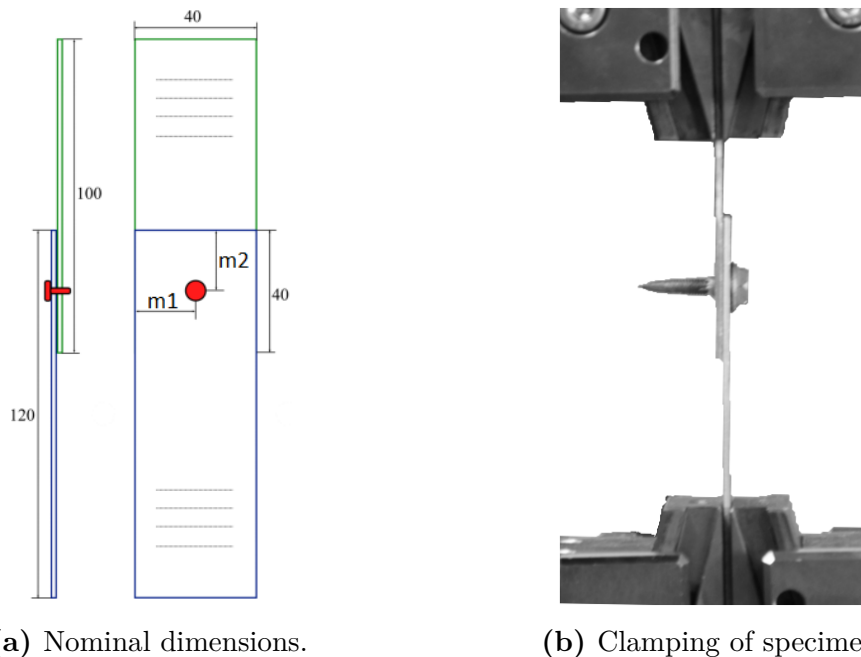
(a) Nominal dimensions.

(b) Clamping of specimen.

Figure 3.8: Dimensions and setup for the two-layered lap-joint tests.

3.2.3 Two-layered peeling

In Fig. 3.9a the nominal geometry of the test specimen is shown. Nominal values of $m1$ and $m2$ were both 20 mm. The clamping of the specimen is shown in Fig. 3.9b. To ensure a rigid setup, 40 mm of both ends of the specimen were clamped in each test. The tests were conducted with a crosshead velocity of 10 mm/min, to ensure quasi-static conditions. Measurements of each specimen as well as average values are shown in Table B.8.

(a) Nominal dimensions.

(b) Clamping of specimen.
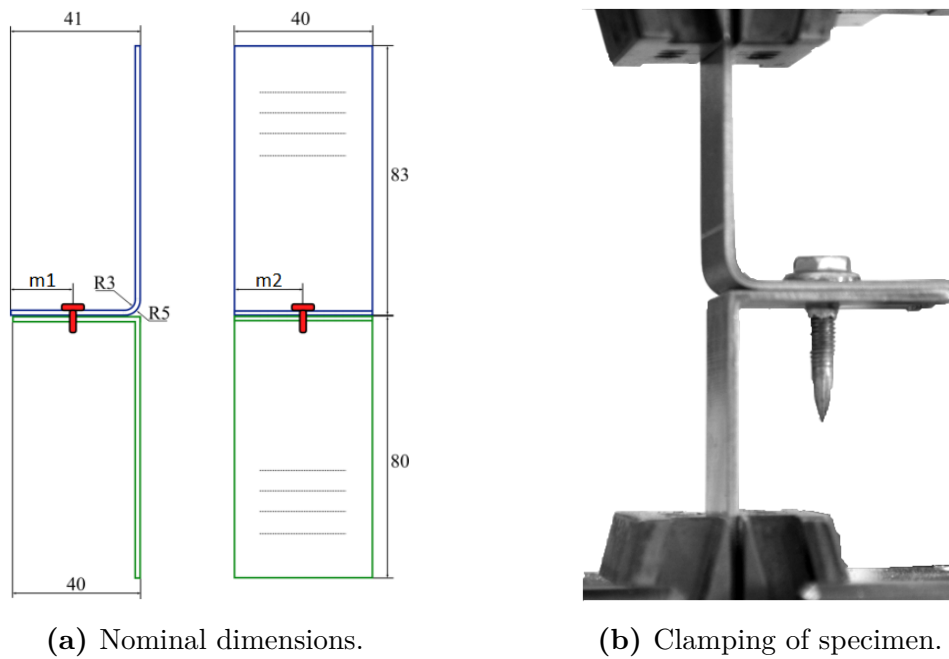
Figure 3.9: Dimensions and setup for the peeling tests.

3.2.4 Three-layered cross

Two different configurations of three-layered cross specimens were used. Nominal dimensions of the plates are shown in Fig. 3.10. Nominal values of $m1$ and $m2$ were 20 mm and 60 mm, respectively. The same test setup as for the two-layered specimens was used. The material in the top and bottom plate was the same, and was oriented like the two-layered crosses. The middle plate was made of AA6016, and oriented different in the two configurations. For cross type 2, shown in Fig. 3.10a, the material orientation was 90 degrees with respect to the longitudinal direction. For cross type 3, shown in Fig. 3.10b, the material orientation was 0 degrees with respect to the longitudinal direction. Measurements of each specimen as well as average values are shown in Table B.9 and Table B.10.
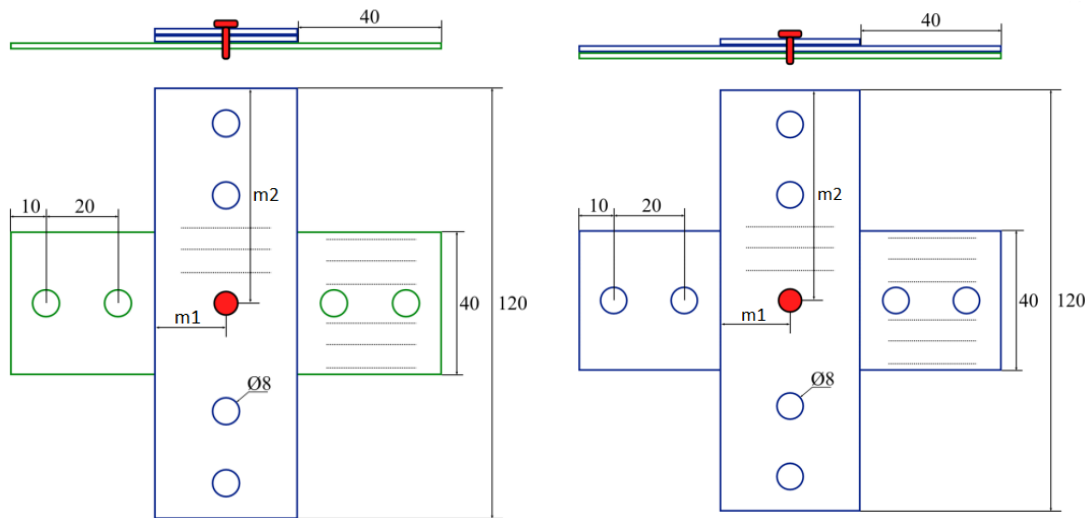
(a) Cross type 2 specimen.

(b) Cross type 3 specimen.

Figure 3.10: Nominal dimensions of the three-layered cross specimens.

3.2.5 Three-layered lap-joint

Nominal dimensions of the specimens are shown in Fig. 3.11. Nominal values of $m1$ and $m2$ were both 20 mm. Measurements of each specimen as well as average values are shown in Table B.11. The same test setup as for the two-layered specimens was used.
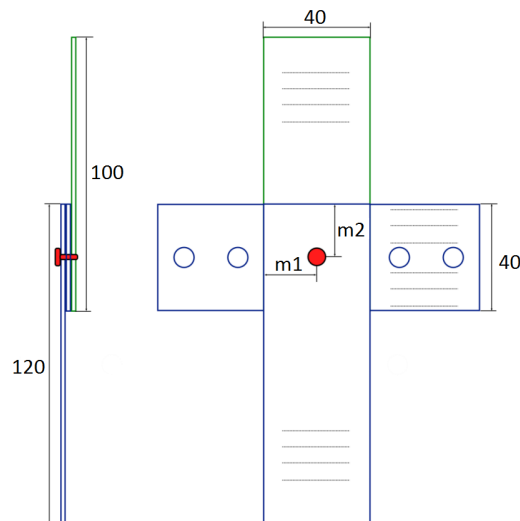
Figure 3.11: Nominal dimensions of the three-layered lap-joint specimen.

3.2.6   Three-layered peeling

Nominal dimensions of the specimens are shown in Fig. 3.12. Nominal values of $m1$ and $m2$ were both 20 mm. Measurements of each specimen as well as average values are shown in Table B.12. The same test setup as for the two-layered specimens was used.
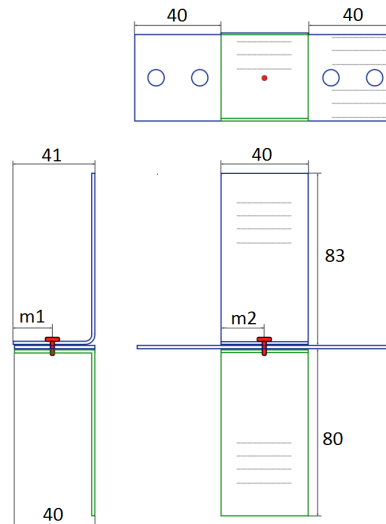
Figure 3.12: Nominal dimensions of the three-layered peeling specimen.

3.3   Component test

The component used in this thesis was made from two aluminium profiles connected together by six screws. The top part was an AA6016 T4 sheet, bent into a hat profile. The bottom part was an extruded AA6063 T6 U-profile cut from a hollow section. Nominal geometry of the parts is shown in Fig. 3.13a. The hat section was screwed on top of the U-section, as shown in Fig. 3.13b. From this point, the component is referred to as the T-component. The test setup is shown in Fig. 3.14a. Measured dimensions of both parts of the T-component are given in Table B.13. The placement of each screw was measured, and is presented in Table B.14, together with Fig. B.1 for illustration. For other configurations and other load cases of similar components using self-piercing rivets, the article by Hoang et al. [21] is recommended.

(a) Nominal dimensions.

(b) Assembly of the T-component.
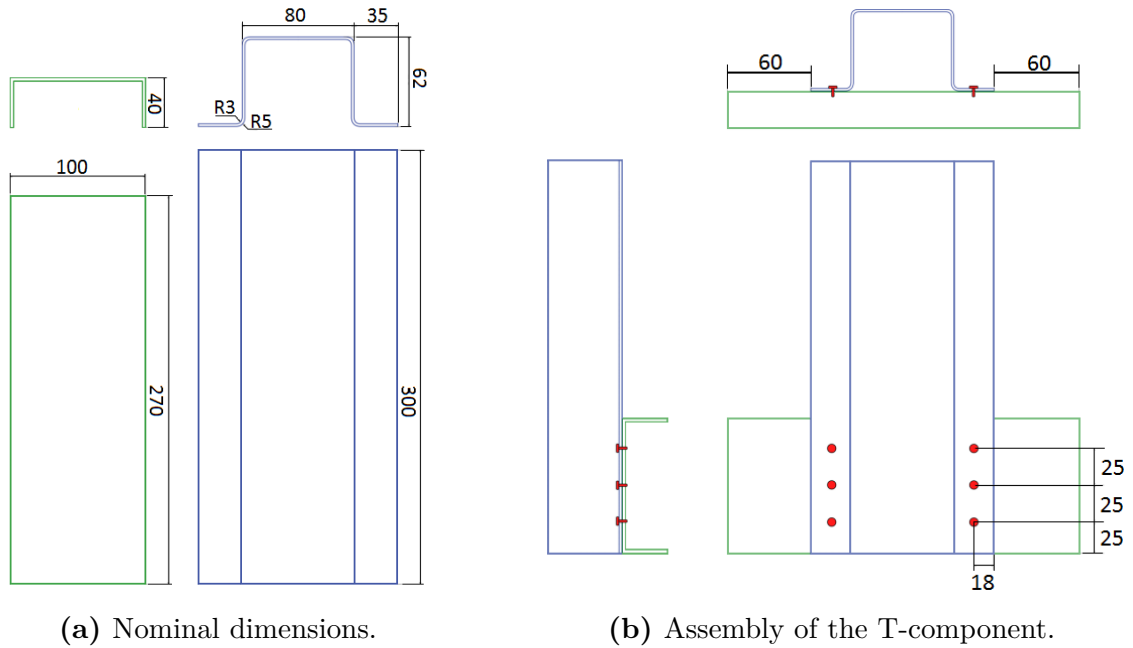
Figure 3.13: Nominal dimensions and assembly of the T-component.

To avoid scatter in the test results, rigid clamping of the specimen for all tests were necessary. The extruded U-profile was held in place by three bolts with a clamping block on each side. To minimise rigid body displacement, the bolts were tightened using a torque wrench with a torque of 90 kNm. The U-profile was also kept in place by blocks over and under the profile as seen in Fig. 3.14b. Force was applied to the free end of the hat profile as pure tensile loading. Two moment free hinges were applied between the load cell and the specimen. Six bolts in the top flange transferred the force from the test machine through a steel plate. The hinges and the clamping in the top is shown in Fig. 3.14a.

The tests were conducted with a crosshead velocity of 2.5 mm/min to ensure quasi-static behaviour. In addition to measuring the cross head displacement, 3D DIC was applied both on the front and back of the specimens. Earlier experiments with similar test setup showed good results from the DIC analysis.

(a) Front of the test setup.

(b) Back of test rig.

Figure 3.14: Experimental test setup for the T-components.

Chapter 4

Experimental results

In this chapter the experimental results are presented. The material tests were performed for the extruded AA6063 T6 material, while the single connector tests and component tests were performed on connections between AA6063 T6 and AA6016 T4 material.

For the single-connector tests, the term top plate refers to the plate with the screw head. This term is also used for the component test, where it refers to the flanges of with the screw head.

4.1 Material tests

Results from the uniaxial tension tests are given in terms of engineering stress and strain curves, where the engineering strain is defined as

$$\epsilon_{eng} = \frac{\Delta L}{L_0} \tag{4.1}$$

Here $\Delta L = L - L_0$, and L and L_0 are lengths in the deformed and original configuration respectively. The engineering stress is defined as:

$$\sigma_{eng} = \frac{F}{A_0} \tag{4.2}$$

F is the load and A_0 is the cross-sectional area in the original undeformed configuration.

The engineering strain was calculated by use of Eq. (4.1), where L and L_0 was taken directly from the extensometer, while the engineering stress was calculated from Eq. (4.2), where F is the load from the test machine in use.

Results from plane strain tension are presented as extensometer displacement versus force. The in-plane single shear is presented both as extensometer versus force and displacement from DIC versus force.

4.1.1 Uniaxial tension

The representative curves from the uniaxial tension tests are shown in Fig. 4.1. Results from all UT experimental tests are presented in Appendix C. As seen, the material showed some anisotropy with respect to flow stress. The scatter in each direction was negligible compared to the scatter in Fig. 4.1. The Young's modulus of each test was very similar, and approximately $70\,000\,\text{MPa}$.
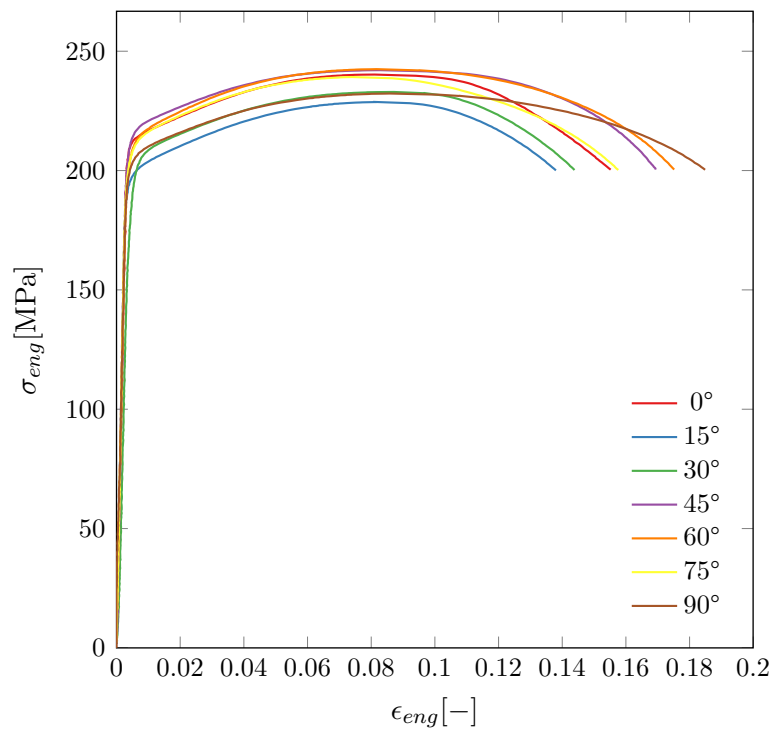
Figure 4.1: Representative curves for UT-specimen.

4.1.2 Plane strain tension

The test results from the PST experiments are presented in Fig. 4.2. The results showed high repeatability, with a maximum load of 8 kN, and a maximum displacement of 1.4 mm. Similar elastic and plastic behaviour were observed for all tests.
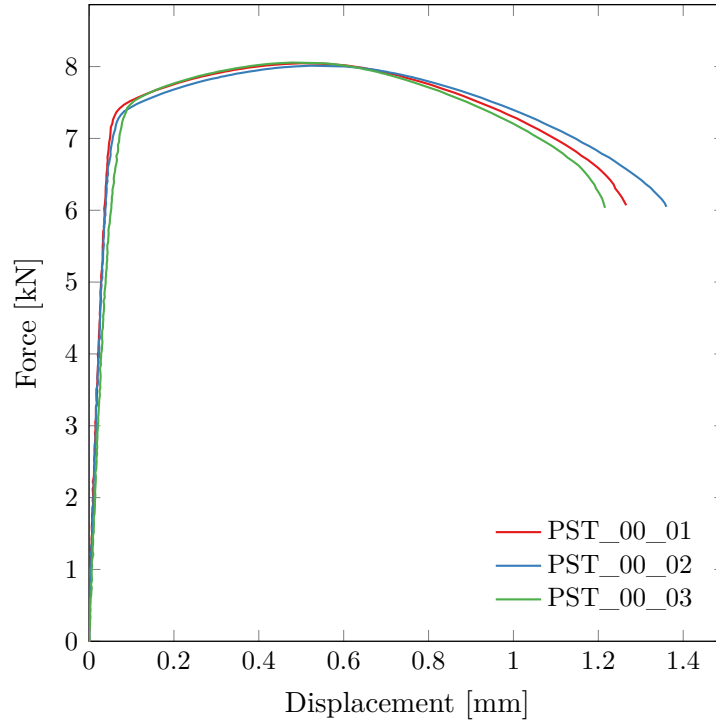
Figure 4.2: Experimental results from PST tests.

4.1.3 In-plane single shear

Results from the in-plane single shear tests are shown in Fig. 4.3. In addition to extensometer, DIC was applied for deformation field measurements. The curve in Fig. 4.3a is plotted using deformation from the extensometer, while the curve in Fig. 4.3b is plotted using deformation from the DIC analysis. Fig. 4.4a shows the mesh used in the DIC analysis of the ISS specimen, with the nodes used to measure relative displacement marked. Relative displacement was calculated in the direction of applied loading. The mesh had an element size of 25×25 pixels which is equivalent to $0.0935 \, \text{mm} \times 0.0935 \, \text{mm}$. A field map of the displacement during the DIC analysis is shown in Fig. 4.4b.

More scatter was observed than for the UT and PST tests, but the repeatability was

still considered acceptable. The maximum load observed for the tests was approximately 0.75 kN. The tests showed low deviation in maximum displacement, especially in the results from DIC. A maximum relative displacement of approximately 1.4 mm was measured. By using DIC, displacement of the shear area could be measured accurately. Comparing the two plots, it is clear that the DIC displacement led to a higher stiffness than the extensometer. This was expected, since strains in the specimen outside the shear area were omitted. The objective of the DIC analysis was to validate the ISS-tests with better accuracy, as well as investigating the possibility of using DIC on the T-component. The results from the analysis were satisfying, showing good repeatability.

(a) Extensometer displacement.

(b) DIC displacement.
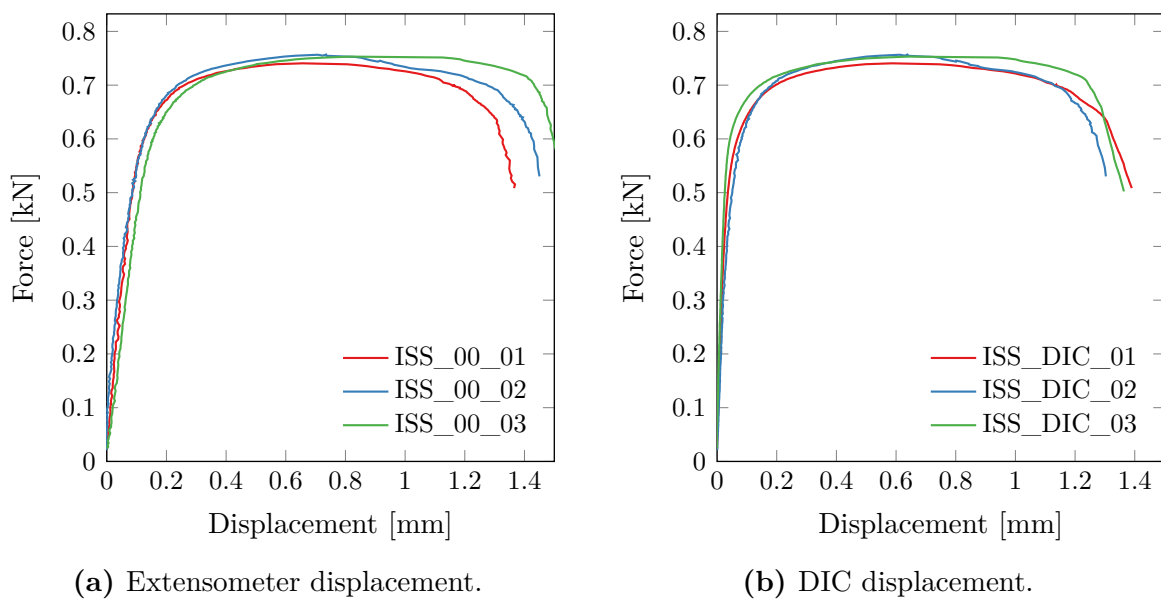
Figure 4.3: Experimental results from ISS tests.

(a) DIC mesh for the ISS specimens.

(b) Displacement field, scale in mm.
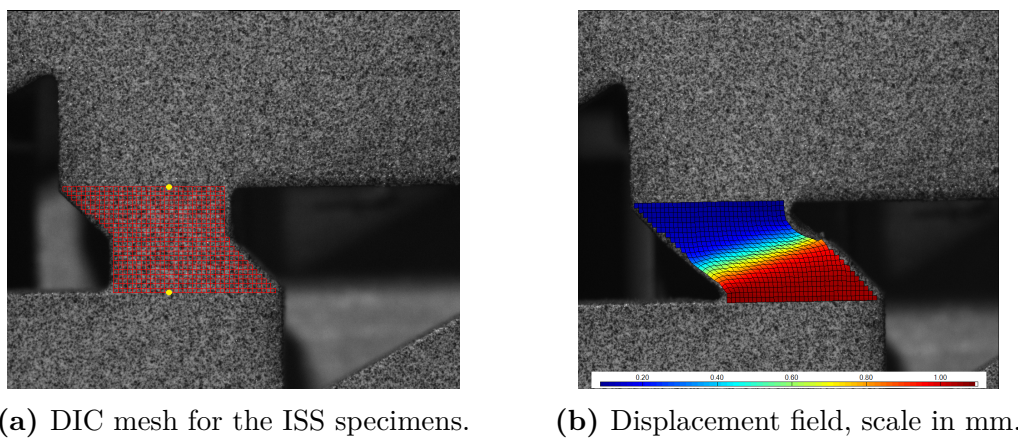
Figure 4.4: Use of DIC on the ISS specimens.

4.1.4 Uniaxial tension test of screws

Uniaxial tension results from the screw tests are shown in Fig. 4.5. In Fig. 4.5a only results up to necking are shown since results after necking are not valid. As can be seen, the stress at necking showed little scatter, the deviation was in the range of 3%. From Fig. 4.5b it is evident that the screws showed a highly ductile behaviour, with little hardening. Maximum stress observed in the tests was 1161 MPa, with a yield stress of 1105 MPa. The failure in the screws was a typical cup-cone failure which is a failure mode often observed in ductile materials [39]. This concludes the material investigation conducted in this study.

(a) Results up to necking.   **(b)** Complete results.
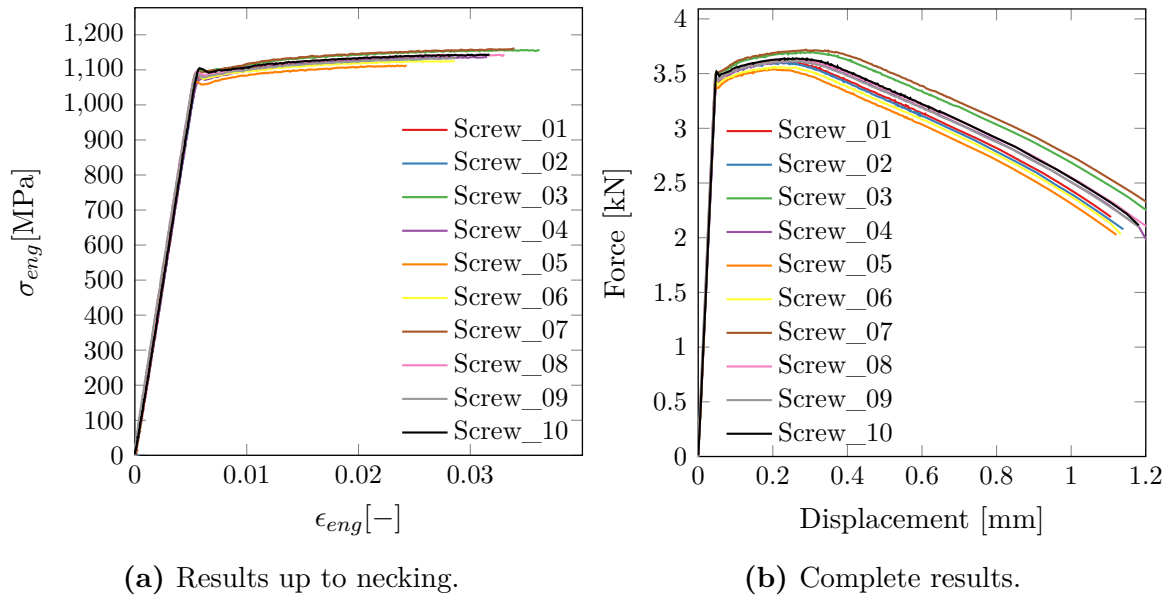
Figure 4.5: Experimental results from UT screw tests.

4.2 Two-layered single connector tests

In this section the results from the two-layered single connector tests are presented. The results are given in terms of force-displacement curves, where both the displacement and force are obtained from the test machine.

It is important to understand that the force-displacement responses presented herein are global responses. The terms "pure tensile load", "pure shear load" and "mixed tensile and shear load" are merely from a global perspective, as the force and displacement are measured globally. The actual, local, loading condition on the connector itself is complex and unknown. However, it is reasonable to assume that the global loading condition is a good indication of the local situation, at least in the beginning of the tests. For instance in the "pure shear" tests; the screw is loaded in shear in the start, but after a while the screw starts to rotate, which introduces tensile forces in the screw, even though the loading is "pure shear" from a global perspective.

4.2.1 Cross

In Fig. 4.6 all results from the two-layered cross tests are shown. The results from tension loading are presented in Fig. 4.6a, while in Fig. 4.6b and Fig. 4.6c the results from the shear and mixed loading are shown, respectively. In Fig. 4.6d a comparison between all curves from the tests is presented.

Acceptable repeatability was obtained for all two-layered cross tests. As seen, the specimen subjected to tension exhibited the lowest forces and lowest ductility of approximately 3 kN and 8 mm, while the shear mode experienced the highest, approximately 6 kN and 20 mm, respectively. In the mixed mode a combination of relatively low forces and high ductility was observed, approximately 4 kN and 20 mm.

The tensile loaded response can be divided into two nearly linear parts, the first from 0 mm to 2 mm and the second from 2 mm to maximum load at 8 mm. The connection failed almost immediately after maximum load was reached.

The forces in the shear loaded specimens showed a near linear response up to about 90% of maximum load, after which the force-displacement curve showed similarities with yielding and hardening in aluminium materials up to maximum load. The linear part is assumed

to be related to a highly elastic deformation, while yielding in the plates and the screw led to the second part of the curve. After maximum load was reached, the force dropped approximately 50% and was then kept constant for 2 mm to 5 mm of displacement. The first drop in force is assumed to be due to pull-out of the screw from the bottom plate. However, since the global loading was pure shear, the threads on one side of the screw were still in contact with the hole in the bottom plate, resisting the deformation.

Specimen C11_90_02 and C11_90_03 experienced slipping between the top and bottom plate at approximately 1 kN force. This is assumed to be caused by sliding between the plates due to higher forces than the friction resistance between them. The top sheet was pre-drilled, and the holes were slightly bigger than the diameter of the screw, enabling a small distance of relative sliding.

Mixed loading results showed a linear elastic behaviour up to about 1.5 kN, then a partly plastic elastic behaviour was observed up to maximum load. After maximum load the force rapidly dropped approximately 60%, where the force again increased alternating up to 55% of maximum load. Failure occurred shortly after. The first drop in forces was due to the initial pull-out of the screw from the bottom plate. However, since the loading direction was 45 degrees, the threads of the screw were still in contact with one side of the hole in the bottom plate. This led to the increase in force, where each small drop in force indicates that a thread passed the bottom sheet.

(a) Tension loading.

(b) Shear loading.

(c) Mixed loading.

(d) Comparison.
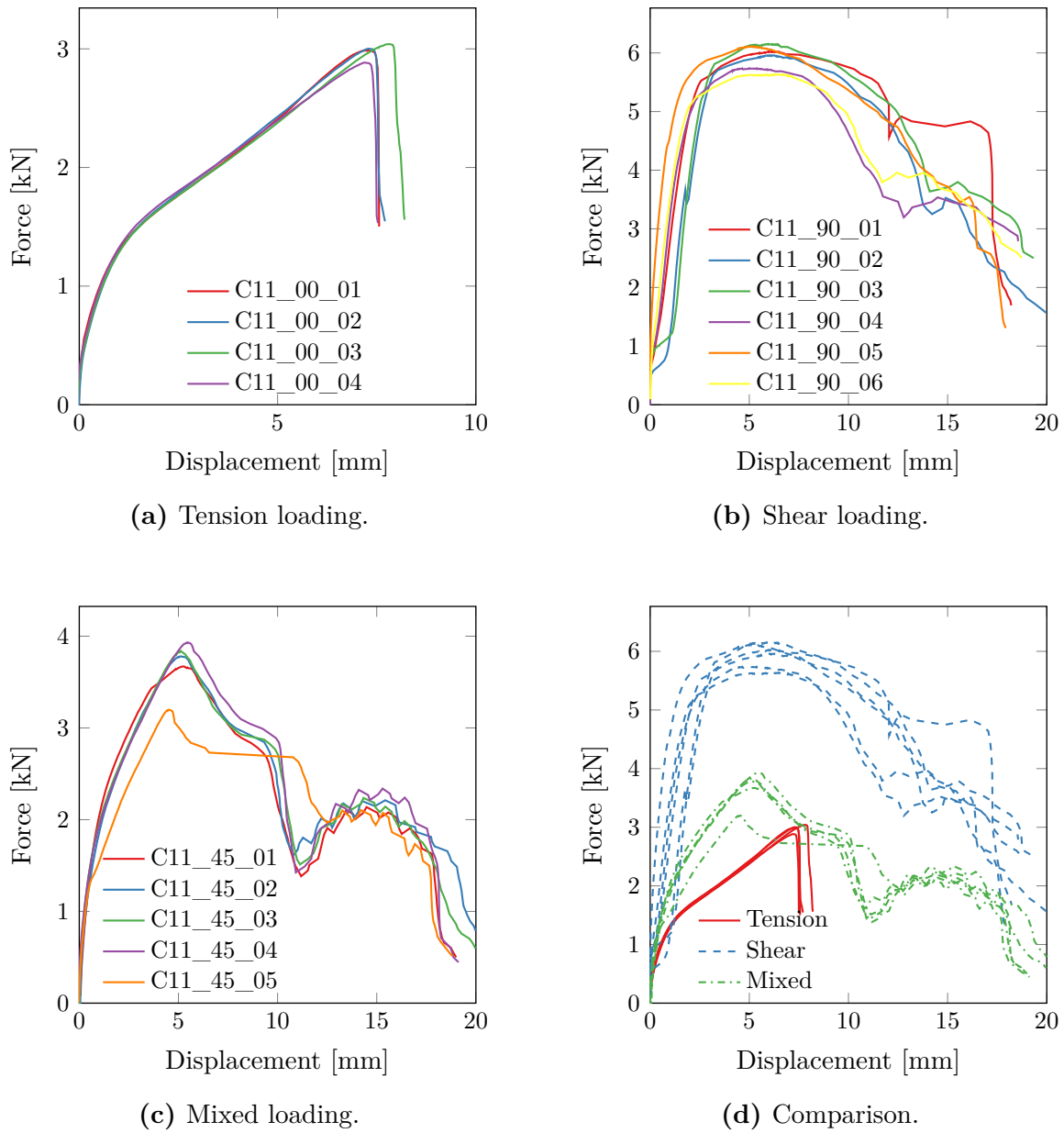
Figure 4.6: Experimental results from two-layered cross test.

In Fig. 4.7 a representative deformed specimen from the tension loaded tests is depicted. The specimen deformation in tensile loading started with bending of both plates, localised around the screw see Fig. 4.7a, and failed in the end by thread stripping from the bottom plate. Fig. 4.7b shows a top view of the deformed specimen. The initial high stiffness observed in the tensile mode was due to the bending of the plates.

(a) Side view. **(b)** Top view.
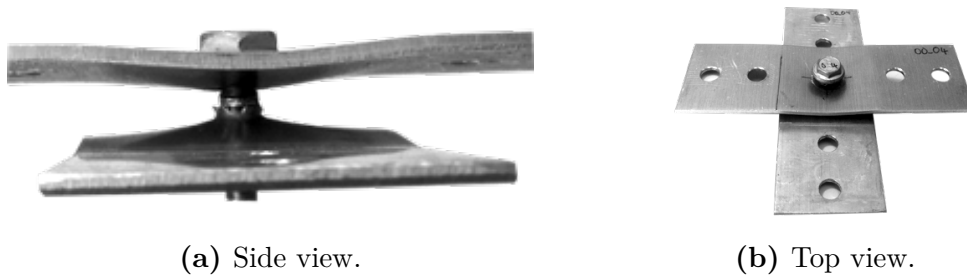
Figure 4.7: Deformation of cross specimen under tensile loading.

A deformed specimen after pure shear loading can be seen in Fig. 4.8. For the shear mode specimen, the deformation started with severe rotation of the screw, see Fig. 4.8a and Fig. 4.8b. The rotation resulted in one side of the head of the screw penetrating the top sheet, in addition to engagement of the threads only on one side of the hole. The connection failed in the end by one-sided thread stripping, combined with material fracture of the bottom plate. This is observed in Fig. 4.8c and Fig. 4.8b, were the fractured material can be seen still connected to the screw. Contrary to the tensile and mixed loading tests some plastic deformation of the screw was observed in the shear tests.

(a) Top view.

(b) Side view close-up. **(c)** Side view.
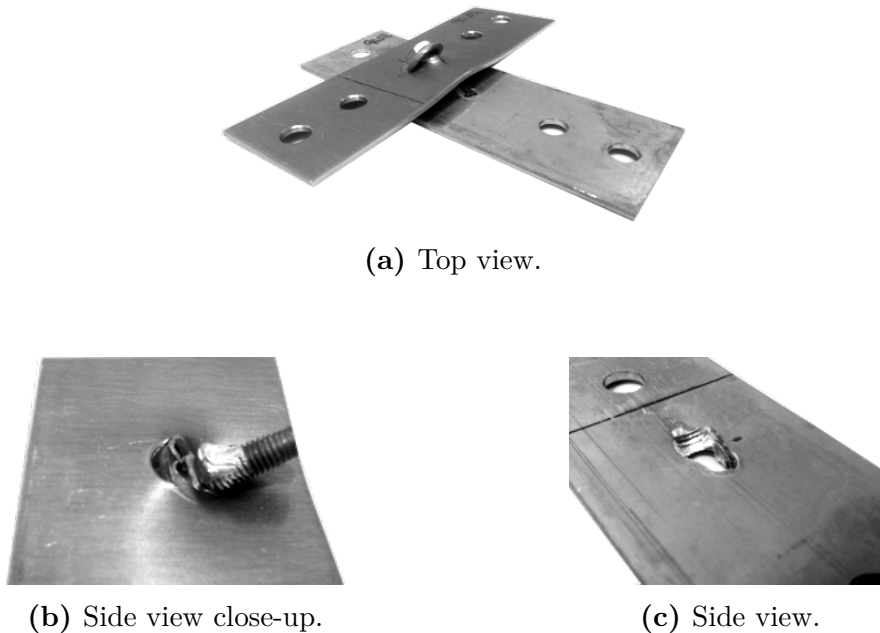
Figure 4.8: Deformation of cross specimen under shear loading.

A deformed specimen after being exposed to mixed loading is shown in Fig. 4.9. Under mixed loading, a combination of the two other failure modes were observed. The rotation

of the screw was not as prominent as for pure shear, but the threads of the screw only engaged on one side of the hole in the bottom plate, and the connection failed due to one-sided thread stripping. From Fig. 4.9a it is clearly seen that bending of the plates around the screw has occoured, in Fig. 4.9b the rotation of the screw is obvious.

(a) Side view.   (b) Top view.

Figure 4.9: Deformation of cross specimen under mixed loading.

4.2.2 Lap-joint

Test results from the two-layered lap-joint experiments are presented in Fig. 4.10. Some scatter was observed in the post peak behaviour. Despite the scatter, the differences in maximum load were in the range of approximately 3%. If specimen LJ_00_01 and LJ_00_04 were excluded, the differences in maximum displacement was in the range of approximately 1.5%. The maximum load observed was approximately 6 kN and the maximum displacement was about 13 mm. Slightly sliding of some of the specimens was also observed in these tests, due to the pre-drilled hole in the top plate.
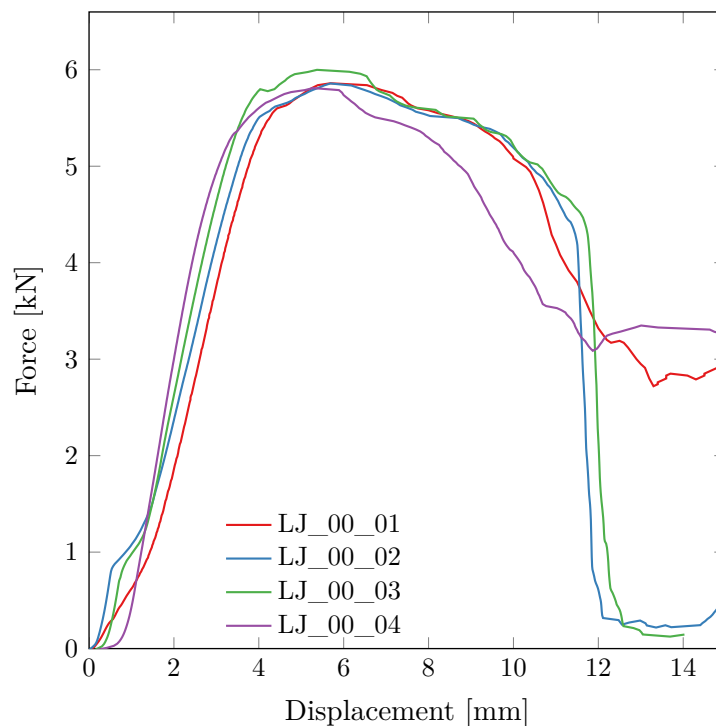
Figure 4.10: Experimental results from lap-joint tests.

The different stages in the failure of the lap-joint connection are presented in Fig. 4.11, where an undeformed specimen is shown in Fig. 4.11a. The specimen deformation showed similarities with the two-layered cross tests in pure shear loading, and started with bending of both plates in combination with rotation of the screw, as seen in Fig. 4.11b. The bottom plate was only bent in the beginning, while the top plate continued with bending combined with rotation of the screw out of the bottom plate, see Fig. 4.11c. As for the two-layered cross in pure shear loading, the lap-joint connection failed due to one-sided thread stripping in combination with more or less material fracture of the bottom plate.

(a) Beginning.   **(b)** Middle.   **(c)** End.

Figure 4.11: Deformation progress for the lap-joint.

The two different failure modes observed are shown in Fig. 4.12. In Fig. 4.12a a deformed specimen that failed with material fracture in the bottom plate is depicted. It is evident that the material in the bottom plate has fractured, as the fractured material remained connected to the screw. From Fig. 4.12b the other failure mode is clearly thread stripping from the bottom plate. It is seen that the material that fractured in Fig. 4.12a is still connected to the bottom plate (seen as a material peak in the right hand side of the hole). The plastic deformation of the screw is also clearly shown in the figure.

(a) Material fracture.   **(b)** No fracture.
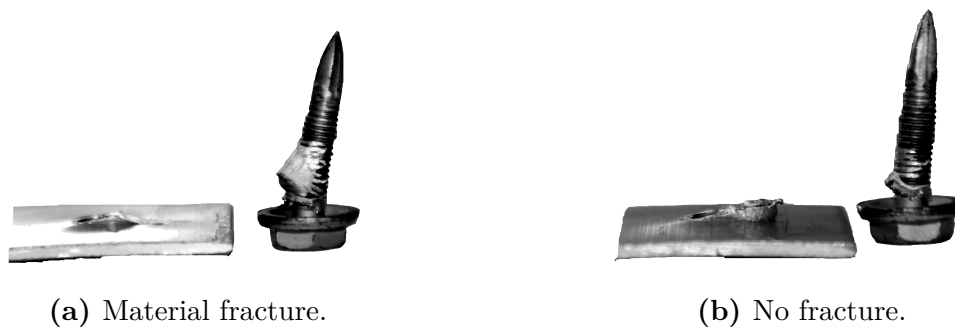
Figure 4.12: Fracture of material in lap-joint tests.

4.2.3 Peeling

Experimental results from the peeling tests are presented in Fig. 4.13. Some scatter was observed in the experiments, but the repeatability is still considered acceptable. The

maximum load and displacement was similar in all tests, approximately 3.3 kN and 30 mm to 35 mm respectively.
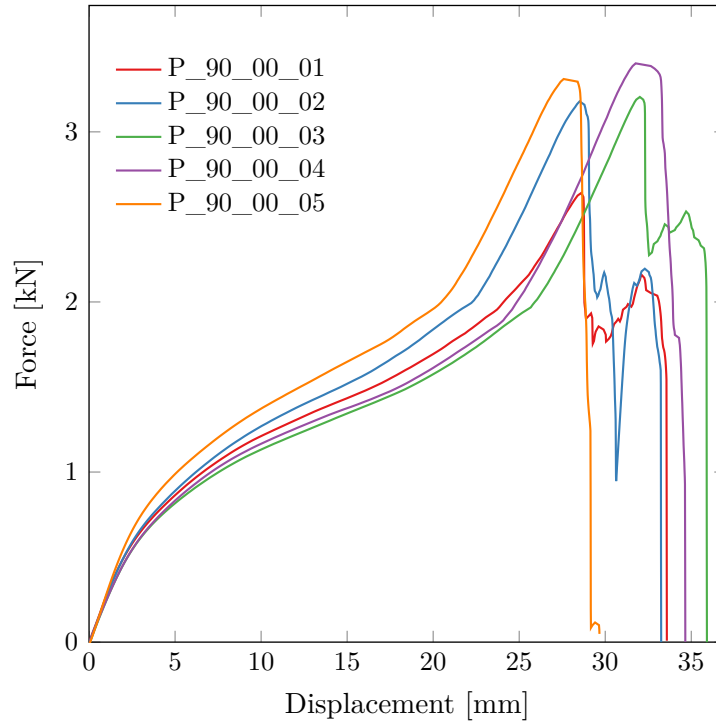
Figure 4.13: Experimental results from peeling tests.

The force-displacement curves can be divided into three near linear parts that corresponds to the three deformation stages depicted in Fig. 4.14, where the undeformed specimen is shown in Fig. 4.14a. The initial stiffness (up to approximately 5 mm displacement) was caused by the L-shaped plates that were stretched out, resulting in new bends around the screw. This resulted in stage two of the deformation, rotation of the screw in combination with continued stretching of the plates, see Fig. 4.14b. This occurred between 5 mm and 20 mm. The asymmetry in bends around the screw is assumed to be partly a result of the different material properties and the fact that the screw head stiffened the top plate. The final stiffness was a result of the screw rotating so far that the tip of the screw came in contact with the bottom plate, shown in Fig. 4.14c, resulting in higher stiffness and increased bending of the top sheet. This corresponds to the sudden steep inclination of force prior to the peak force in Fig. 4.13. The connection failed in the end due to thread stripping from the bottom plate.

(a) Beginning.   **(b)** Middle.   **(c)** End.
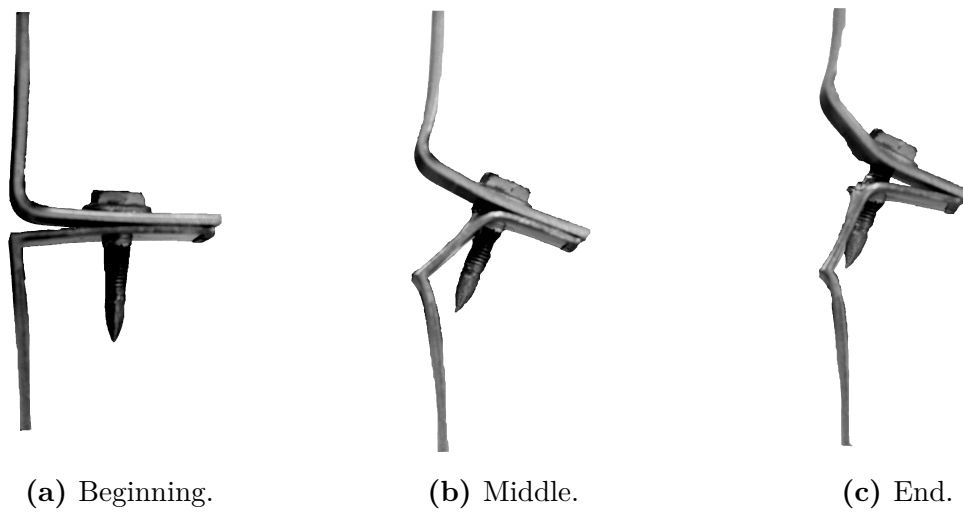
Figure 4.14: Deformation progress in the peeling test.

The loading in the peeling tests was assumed to be tensile dominated. Comparing the results with the tensile loaded cross tests presented in Fig. 4.6a, it is seen that the maximum loads were similar, but severe differences were observed for the displacement. This comes as a result of the stretching of the L-shaped plates, which leads to large displacements without introducing high tensile forces in the screw. This may be avoided if the responses could be measured locally instead of globally.

4.3   Component test

Results from the component tests are shown in Fig. 4.15. Since DIC was applied in the component tests, the results are plotted both as force versus crosshead displacement, and force versus displacement obtained from the DIC analysis. In Fig. 4.15a the results with crosshead displacement are shown, and in Fig. 4.15b the results with DIC displacement are presented. High repeatability was observed, and the maximum load and crosshead displacement in all tests was approximately 33 kN and 27 mm, respectively.

Fig. 4.16a shows the mesh used in the DIC analysis of the component, with the nodes used to measure relative displacement marked. Relative displacement was calculated in the direction of applied loading. The mesh had an element size of 30×30 pixels which is equivalent to $1.95\,\text{mm} \times 1.95\,\text{mm}$. A field map of the strains at the time of maximum force is shown as an example in Fig. 4.16b.

(a) Cross head displacement.
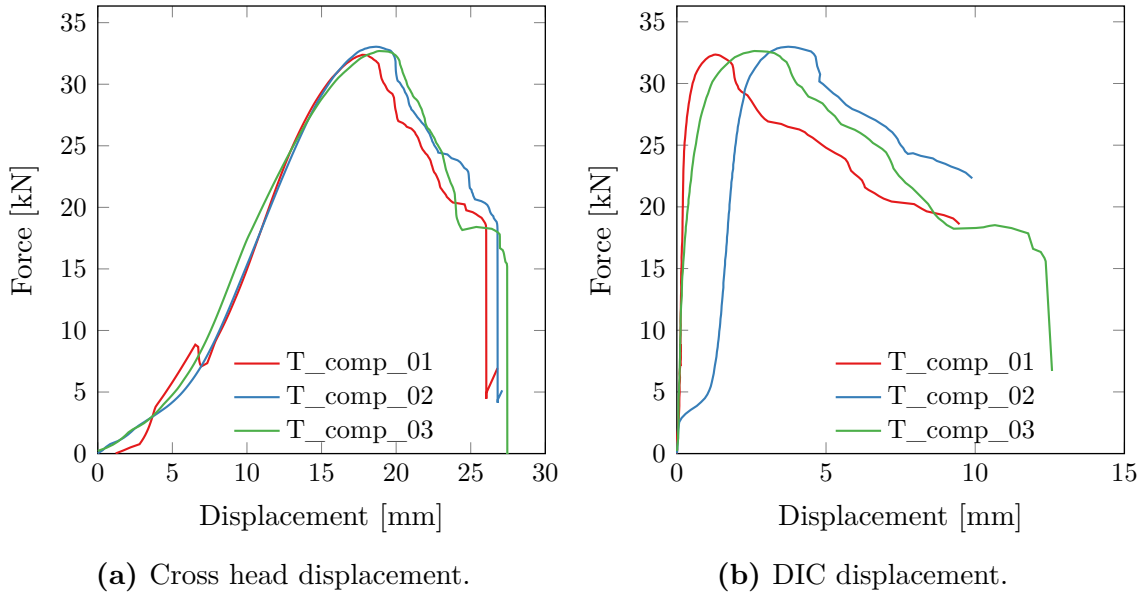
(b) DIC displacement.

Figure 4.15: Results from T-component test.

The results from the DIC analysis were significantly stiffer, which was expected since only the deformation in a small area was taken into account. Using crosshead displacement, deformation in the whole specimen and the test setup was registered, resulting in softer curves. The DIC measurements were necessary when the experimental results were to be compared to numerical simulations.

As seen from the DIC results, specimen T_comp_02 had a decrease in stiffness at 3 kN force. This was due to relative slipping between the top and bottom layer in the connections caused by the pre-drilled holes in the top layer. This was in accordance with observations done for the single connector tests exposed to shear dominated loading. The slipping cannot be seen in the two other tests. The reason for this is that failure of the test rig occurred early in test number 01 and 03. The failure of the rig happened during elastic deformation for both tests, after 25 kN and 15 kN, respectively. The tests were repeated as the specimens showed no plastic deformation, but slipping in the connection had already occurred. The stiffness and maximum force did not appear to be affected, but more component tests should be performed to conclude. Results including the failed tests are shown in Fig. C.2 in Appendix C.

(a) DIC mesh.   **(b)** Strain field during experimental test.
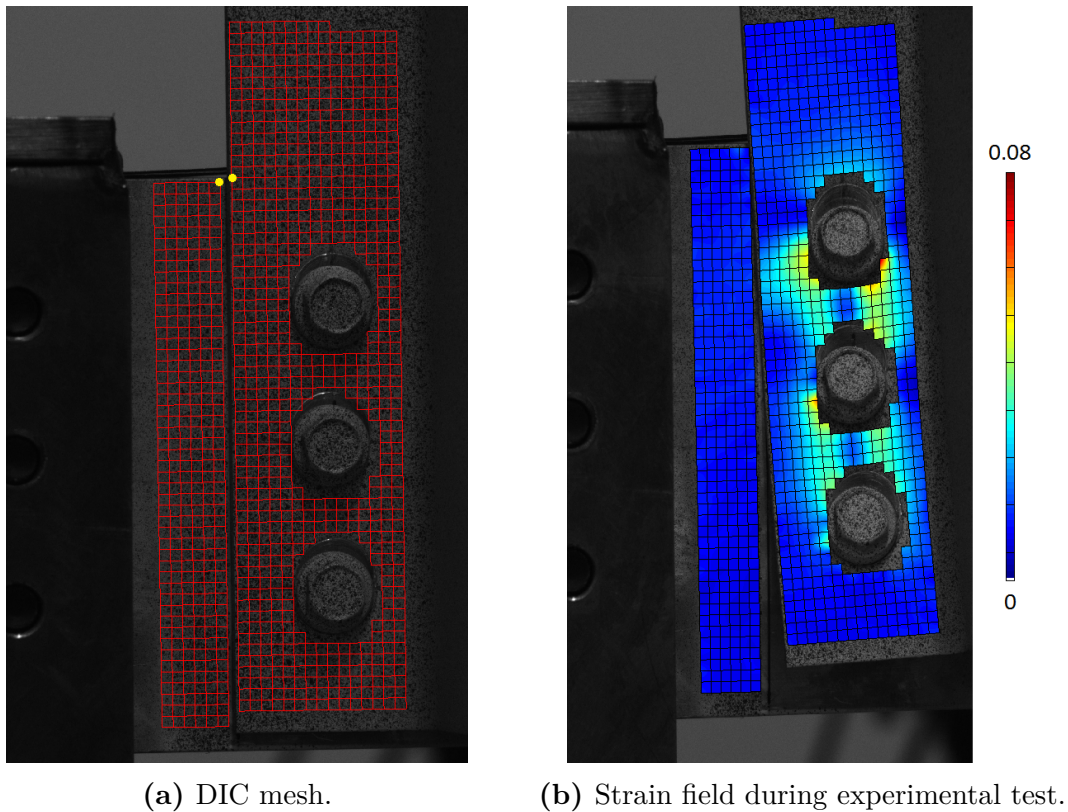
Figure 4.16: Application of DIC on the T-component.

In Fig. 4.17 deformed component specimens are displayed. The deformation of the T-component started with a small deformation of the webs at the top of the hat section around the clamping device, shown in Fig. 4.17a. As seen, the webs have diverged during the test. This is assumed to be caused by the force transfer from the clamping device in the top flange to the screws in the bottom flanges through the webs. The test continued with rotation of the screws and increased tensile forces until the connections failed by one-sided thread stripping in combination with more or less material fracture in the bottom layer. The rotation of the screws led to engagement of the threads on only one side of the bottom layer, similar to what was observed in the shear cross tests and the lap-joint tests. From Fig. 4.17b it is evident that the bottom screw failed first, followed by the two others. Only the screws on one side failed in each test.

(a) Top view.
(b) Back view.
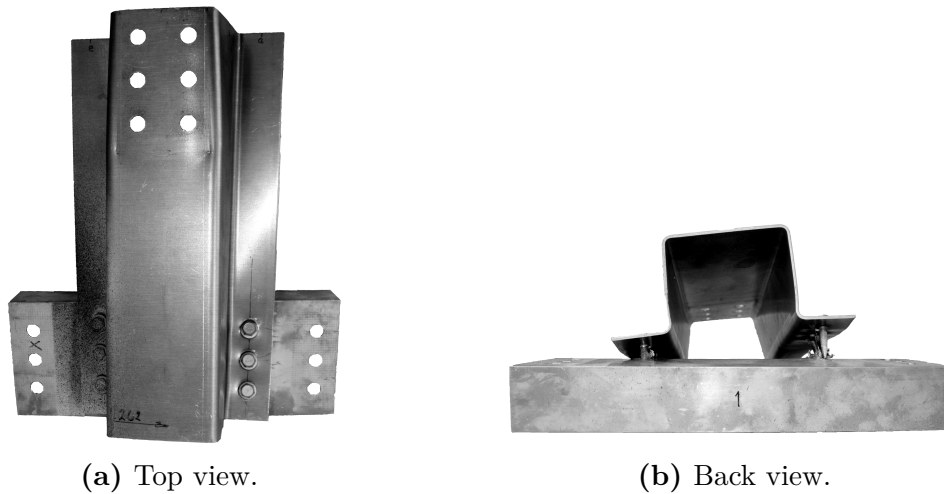
Figure 4.17: Deformed component specimen.

In Fig. 4.18 examples of one sided thread stripping are depicted. As seen in Fig. 4.18a it is evident that the threads of the screw only were engaged at one side of the hole. Fig. 4.18b shows a top view of one hole, photographed from two different directions. The threads have been smeared out, combined with pull-out of material on one side. The threads on the opposite side are still intact.

(a) Bottom view.
(b) Top view of a screw hole.
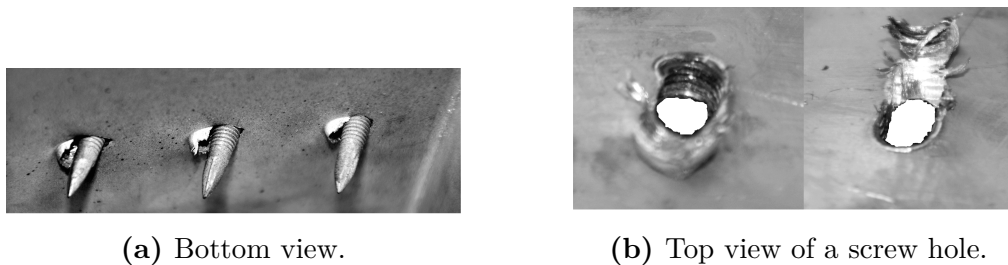
Figure 4.18: One sided thread stripping.

A comparison between the deformed specimens from the component, the lap-joint (Fig. 4.11) and the pure shear loaded cross (Fig. 4.8) tests show similarities in deformation and failure. It is evident that rotation introduced tensile forces in the connector in all tests. Additionally all tests failed in thread stripping from the bottom plate or thread stripping in combination with material fracture. However, the plastic deformation of the screw observed in the lap-joint and pure shear cross did not occur in the component tests.

4.4 Three-layered single connector tests

In this section the results from the three-layered single connector tests are presented. The results are given in terms of force-displacement curves, where both the displacement and force were obtained from the test machine. Recall from Section 4.2, it is important to understand that the force-displacement responses presented herein are global responses, and that the actual loading condition locally on the connector itself is complex and unknown.

4.4.1 Cross type 2

Results from the cross type 2 tests are presented in Fig. 4.19. Tension loaded tests are presented in Fig. 4.19a, while the shear- and mixed loaded results are presented in Fig. 4.19b and Fig. 4.19c, respectively. In Fig. 4.19d all curves are shown as a comparison between the different loading directions.

As for the results in two-layered cross tests, the highest forces were seen for the shear load, approximately 8 kN. However only the second highest displacement were observed for the shear tests, about 13 mm. The tensile loaded tests showed the lowest forces and displacement with about 3 kN and 6 mm. The mixed loaded specimens only experienced slightly higher forces than the tensile loaded tests, yet the highest ductility was observed in these tests, approximately 4 kN and 16 mm.

The specimen C_21_45_04 showed a sliding plateau at approximately 1 kN force. This is assumed to be caused by relative sliding between the bottom and the top layers, due to the pre-drilled hole in the top layers with a slightly bigger diameter than the diameter of the screw.

(a) Tension loading.

(b) Shear loading.

(c) Mixed loading.

(d) Comparison.
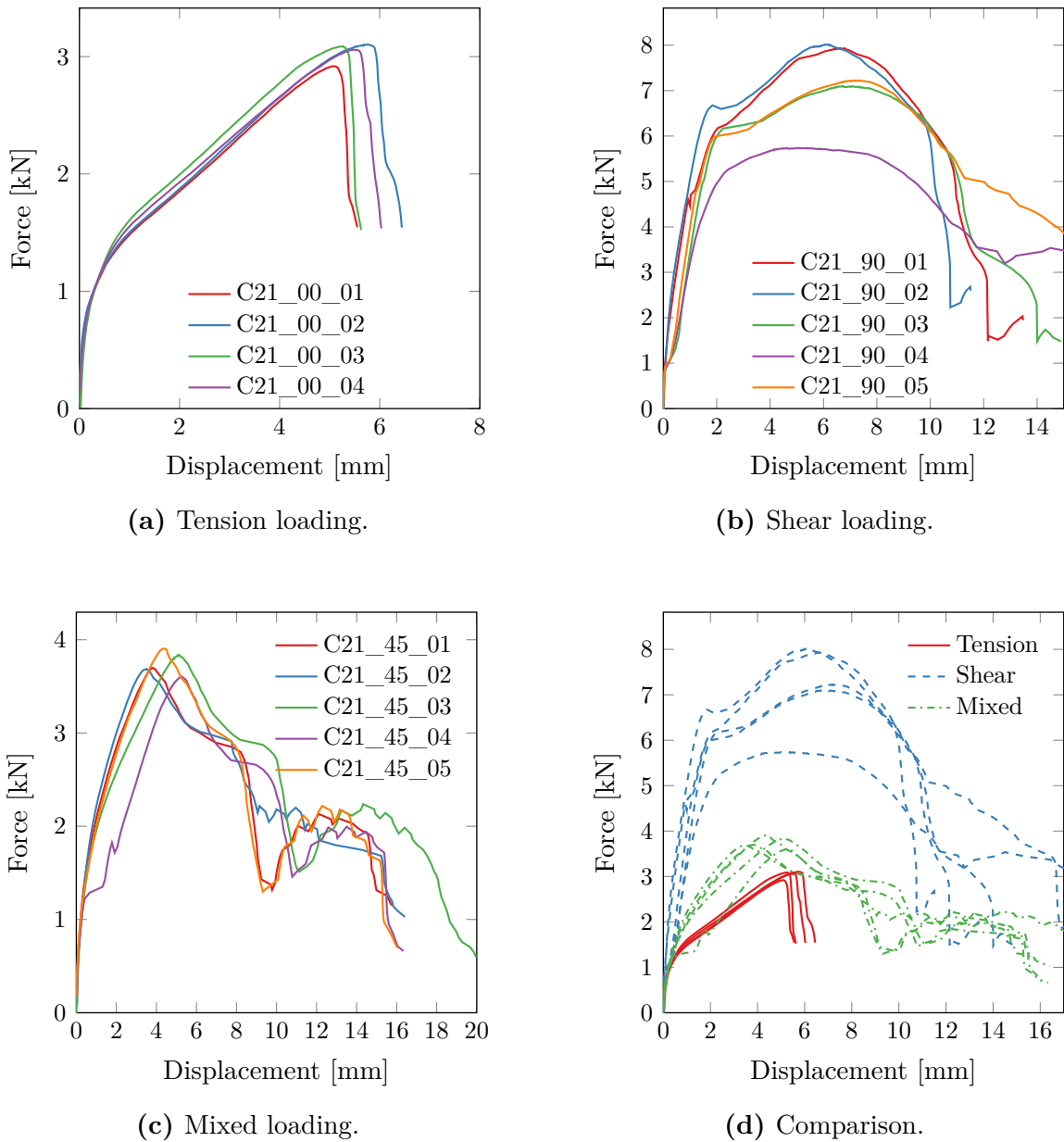
Figure 4.19: Experimental results from cross type 2 tests.

For the results from tensile load, the repeatability was good, as the differences in maximum load and displacement were in the range of approximately 6%. As for the two-layered tensile loaded cross tests, the deformation and the force progression may be divided in two nearly linear parts. Fig. 4.20 shows a deformed cross specimen after being loaded in tension. In Fig. 4.20a a top view of the specimen is presented.

(a) Top view.   **(b)** Bottom view.
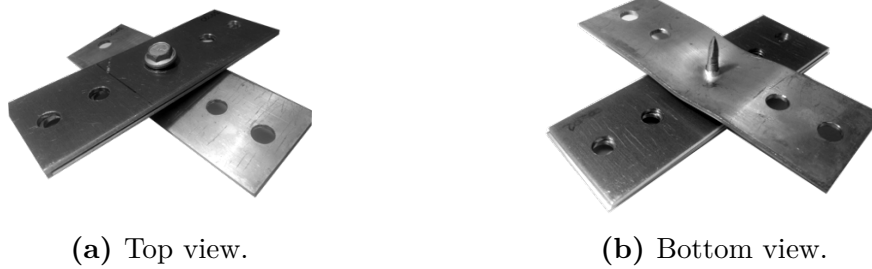
Figure 4.20: Deformation of cross specimen under tensile loading.

The two linear parts of the force-displacement curve relates to Fig. 4.20 in the sense that it is evident that bending of the bottom plate has taken place, see Fig. 4.20b. This corresponds to the second part of the curve (from about 1 mm displacement to maximum load). The first part, up to approximately 1 mm displacement, correspond to elastic deformation. The connection failed due to thread stripping from the bottom plate.

Deformation of the pure shear loaded cross type 2 was different from the two-layered. In the two-layered shear test the deformation started with rotation of the screw, which led to a successful attempt from the screw head to penetrate the top sheet. On the contrary, in the pure shear tests for cross type 2, the high stiffness of the two top plates enforced plastic deformation of the screw itself, instead of the plates. This led to bending of the screw between the bottom and the top layers. The connection failed in the end by fracture of the screw itself, between the bottom and the top layers.

A specimen in deformed configuration exposed to shear loading is presented in Fig. 4.21. As seen from Fig. 4.21a and Fig. 4.21b, the failure mode is fracture of the screw itself near the head, due to a combination of shear and bending forces. From Fig. 4.21c a high degree of rotation and pull-out is obvious.

(a) Top view.

(b) Top view of bottom plate.

(c) Bottom view close-up.
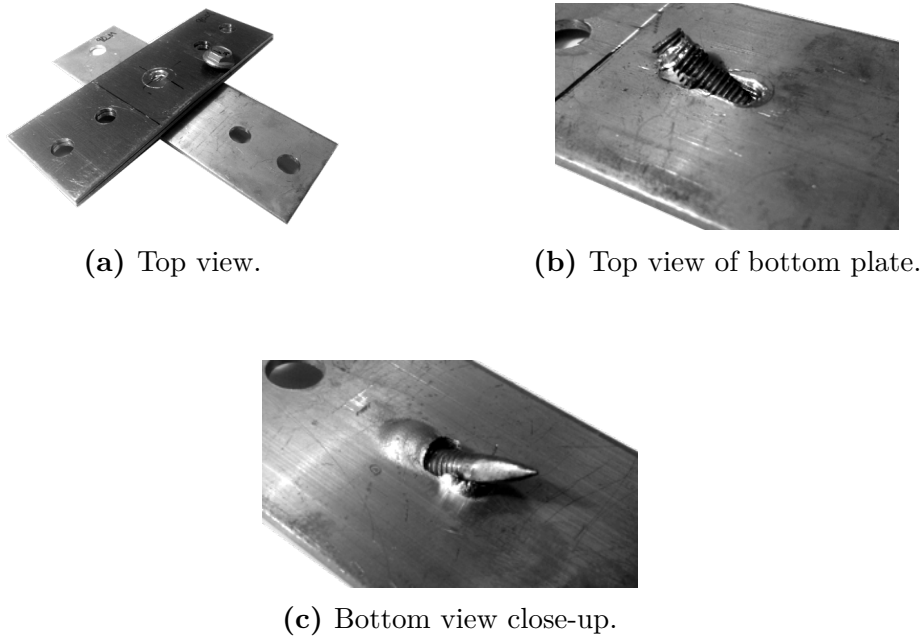
Figure 4.21: Deformation of cross specimen under shear loading.

The force-displacement curve for the tests in pure shear loading, shows that the force increased rapidly up to approximately 85% of maximum load, and then dropped approximately 1% before increasing to maximum load. The force then dropped to approximately 70%, where the connection failed. It is assumed that the first drop was caused by yielding in the screw due to combined shear and bending, and that the hardening after was a result of continued rotation of the screw, combined with bending and material pull-out in the bottom sheet.

Fig. 4.22 shows a deformed specimen from mixed loading, where Fig. 4.22a shows a top view. The type 2 cross specimen in mixed loading failed by one-sided thread stripping. This was a result of rotation of the screw and loss of thread engagement on one side of the screw as shown in Fig. 4.22b. There has also been a slight bending of the bottom plate around the screw hole. This is very similar to what was observed for the two-layered cross tests exposed to mixed loading. No deformation of the top plates was observed during the tests.

(a) Top view.

(b) Close-up view of bottom plate.
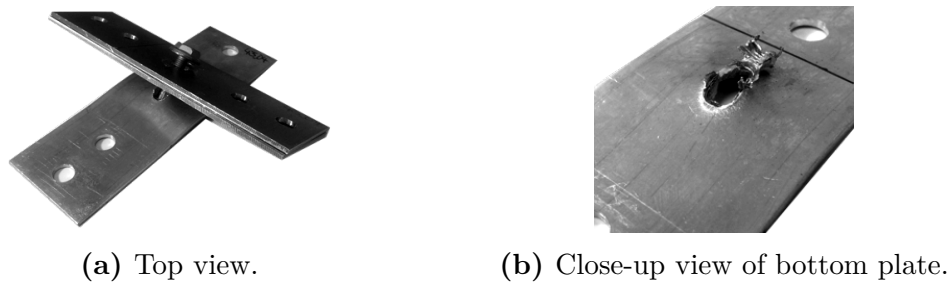
Figure 4.22: Deformation of cross specimen under mixed loading.

The mixed loaded cross results showed a nearly linear elastic behaviour up to about 2 kN, then a partly plastic elastic behaviour was observed up to maximum load. After maximum load the force rapidly decreased approximately 60%, where the force again increased, alternating up to 55% of maximum load. Failure occurred shortly after. The first drop in forces was due to the initial pull-out of the screw from the bottom plate. However, since the loading direction was 45 degrees, the threads of the screw were still in contact with one side of the hole in the bottom plate. This led to the increase in force, where each small drop in force indicates that a thread passed the bottom plate. This is the same observation done for the mixed loaded two-layered cross specimen.

4.4.2 Cross type 3

Results from the type 3 cross tests are presented in Fig. 4.23. Results from the tension loaded specimens are presented in Fig. 4.23a, the pure shear loaded specimens in Fig. 4.23b, and the mixed loading results in Fig. 4.23c. All type 3 cross results are shown in Fig. 4.23d, to compare the different load angles.

The tension and mixed loaded specimens experienced the lowest forces, approximately 4.5 kN, and the lowest maximum displacement of approximately 8 mm. The specimens in pure shear loading experienced forces of approximately 9 kN and displacement of 17 mm to 20 mm. The maximum force reached in the shear tests was approximately twice as high as for tension and mixed loading.

Some relative sliding between the top and bottom layers was also observed in the shear tests. The relative sliding was a result of the pre-drilled hole in the middle and top plate with a diameter slightly bigger than the diameter of the screw, enabling a small distance of relative sliding.

(a) Tension loading.

(b) Shear loading.

(c) Mixed loading.

(d) Comparison.
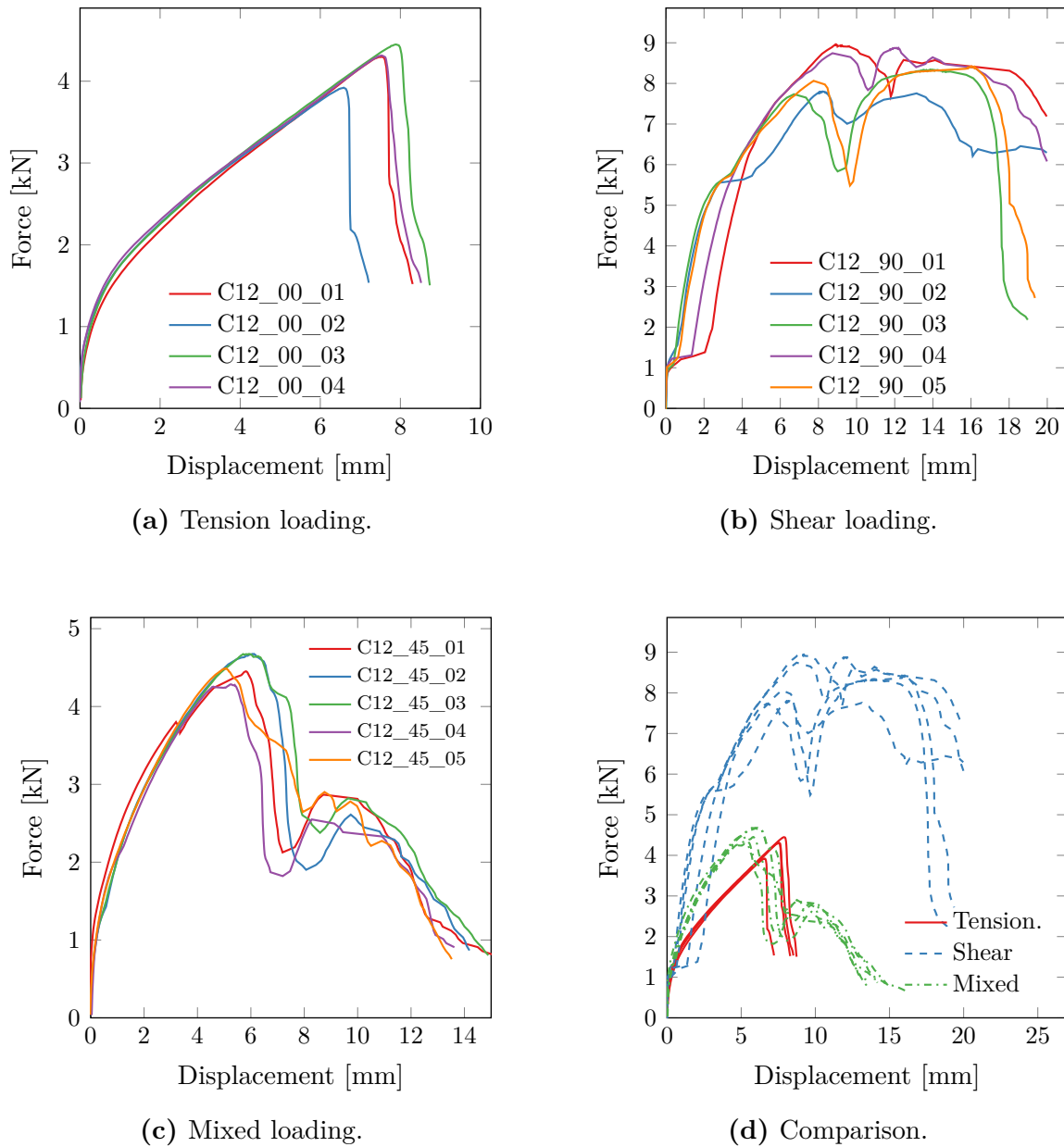
Figure 4.23: Experimental results from cross type 3 test.

In Fig. 4.24 a deformed specimen from tension loaded cross type 3 tests is shown. The deformation of the tension specimen was very similar to what was observed for the two-layered and the cross type 2 tests. As seen in Fig. 4.24a and Fig. 4.24b it is evident that bending occurred in all sheets. The force displacement curve may again be divided into two nearly linear parts, whereas the first part, up to about 1 mm displacement, corresponds to elastic deformation. The second part, from 1 mm to maximum load, corresponds to the bending of the plates. The connection failed due to thread stripping from the bottom

layer.

(a) Side view.

(b) Top view.

Figure 4.24: Deformation of cross type 3 specimen under tensile loading.

For the cross type 3 shear tests, failure occurred in the material in the top sheet. The connection failed in end tear-out as can be seen in Fig. 4.25. This is a failure mode consisting of shear failure in the plate material along the loading direction [40]. Fig. 4.25a shows a top view of a deformed specimen. The deformation of the shear loaded specimen started with rotation of the screw, indicated in Fig. 4.25b. The rotational resistance of the screw was higher than for the two-layered tests due to the increased distance between the bottom plate and the screw head. This led to a high pressure on the edge of the screw hole in the top sheet, and to failure due to tear-out, seen in Fig. 4.25c.

(a) Top view.

(b) Side view.

(c) Side view close-up.
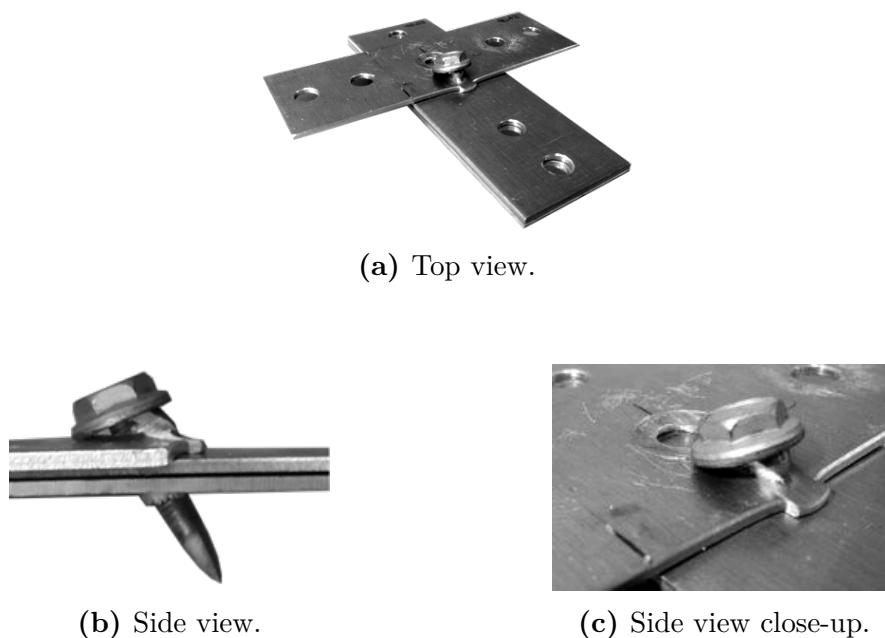
Figure 4.25: Deformation of cross type 3 specimen under shear loading.

A deformed type 3 cross specimen exposed for mixed loading is shown in Fig. 4.26. De-

formation started with bending of the plates and failed due to thread stripping from the bottom plate. Fig. 4.26a and Fig. 4.26b show that the bending is most prominent in the top sheet, which is expected since there are two plates in the bottom layer.

(a) Top view.

(b) Side view.

Figure 4.26: Deformation of cross type 3 specimen under mixed loading.

4.4.3 Lap-joint

Experimental results from the three-layered lap-joint tests are presented in Fig. 4.27. As seen, there is a clear plateau where the force is kept constant between 2 mm and 4 mm. This is assumed to be caused by relative sliding between the plates due to the pre-drilled holes in the top sheets. Maximum force and displacement were similar in all tests. The first experiment had an initial slip in the clamping device that gave a constant deviation in displacement from the other results. The maximum force and displacement were approximately 5.8 kN and 13 mm to 15 mm, respectively in all tests.

In Fig. 4.28 a specimen during different stages of the deformation process is shown. The undeformed specimen is shown in Fig. 4.28a. The deformation started with bending of both end plates, shown in Fig. 4.28b. This continued until yielding in the screw occurred. Bending of the plates induced rotation of the screw, and an attempt from the head of the screw to penetrate the top layer. This again led to the plastic bending of the screw between the top sheet and the middle sheet, see Fig. 4.28c. In two out of three tests the connection failed due to fracture of the screw itself. By analysing pictures taken during the tests, it is assumed that the plastic deformation of the screw occurred when the load reached 5 kN and at a total crosshead displacement of about 7 mm. This corresponds well with the decrease in stiffness from the force-displacement curves.
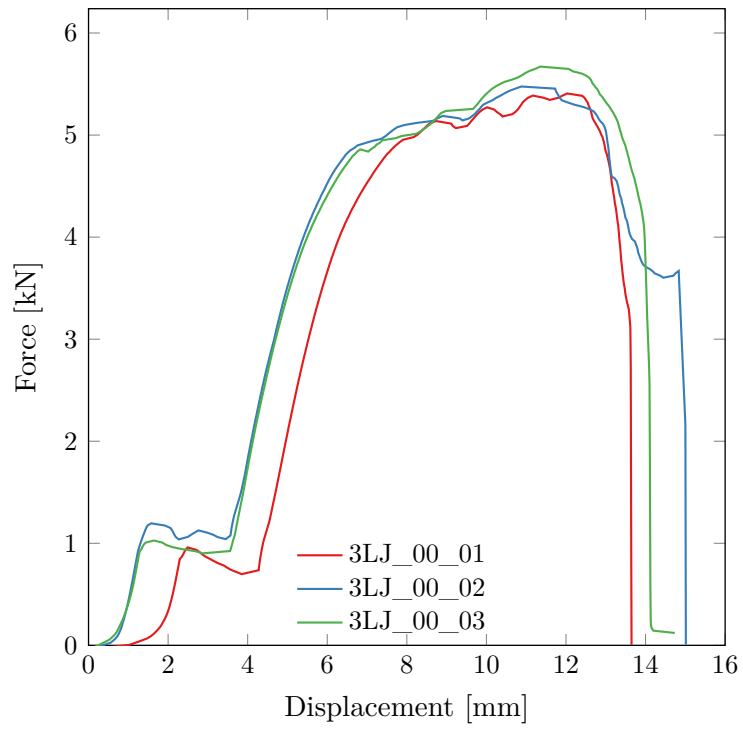
Figure 4.27: Experimental results from three-layered lap-joint.

(a) Beginning.　　　　　(b) Middle.　　　　　(c) End.
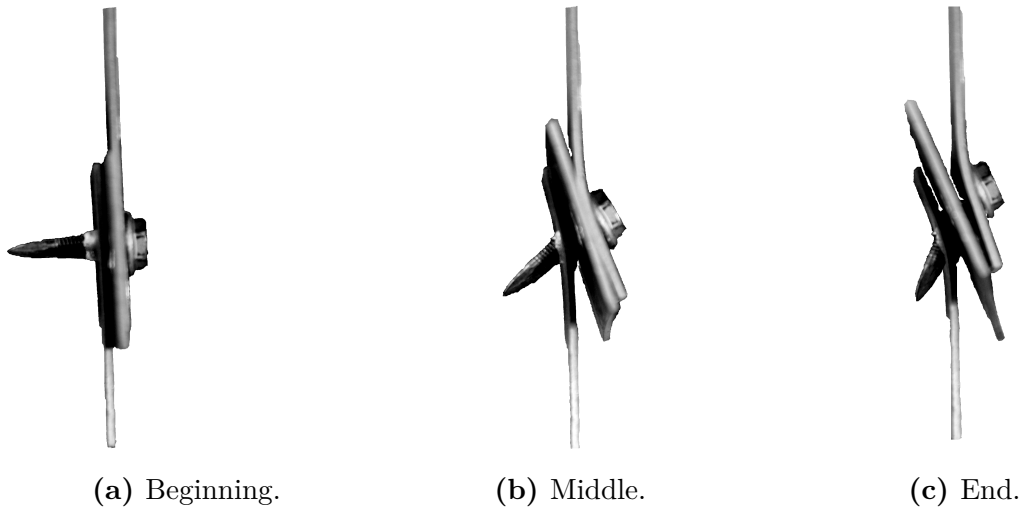
Figure 4.28: Deformation progress of a three-layered lap-joint test.

4.4.4 Peeling

Results from three-layered peeling test are presented in Fig. 4.29. If test 03 is omitted, the repeatability is good. The maximum forces and displacements in the three representative tests were about 3.3 kN and 33 mm.
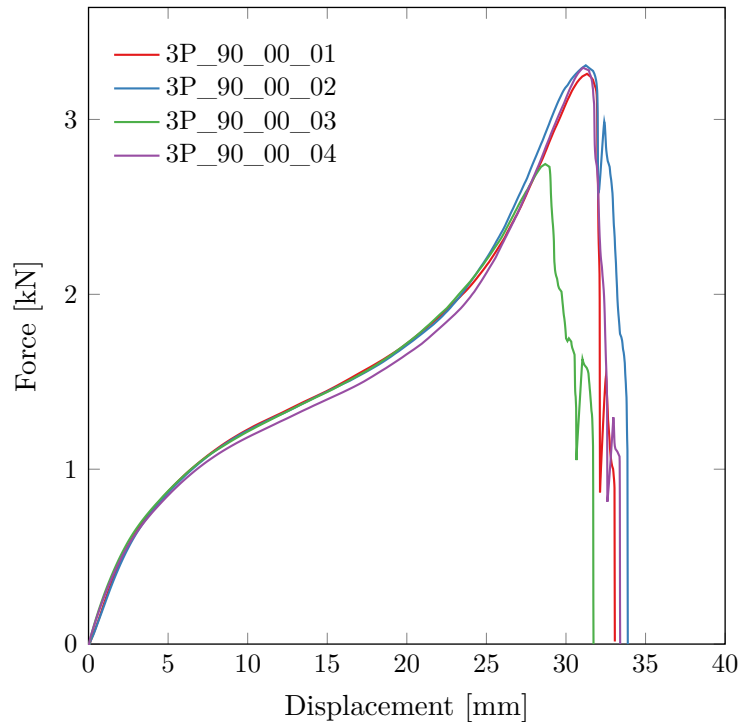
Figure 4.29: Experimental results from three-layered peeling tests.

Similar to the two-layered peeling, the curves can be divided into three nearly linear parts, that correspond with the different stages of the deformation progress shown in Fig. 4.30. Fig. 4.30a shows a specimen in the beginning of a test. The first linear part (up to about 5 mm) is assumed to be elastic deformation. The deformation progress started with bending of both end plates. The bottom plate showed the most severe deformations, see Fig. 4.30b. The bending resulted in rotation of the screw, which in turn led to increased stiffness of the top plate due to the area of the screw head. This correspond to the second linear part from about 5 mm to 25 mm. The third linear part from 25 mm to maximum load, is a result of the tip of the screw coming in contact with the bottom plate due to high rotation, seen in Fig. 4.30c. The connection failed because of thread stripping.

(a) Beginning.   (b) Middle.   (c) End.
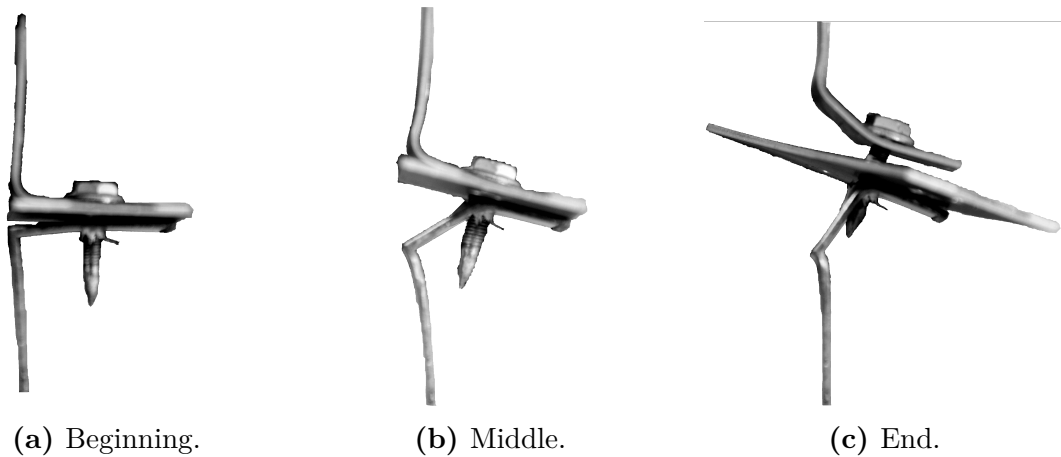
Figure 4.30: Deformation progress of a three-layered peeling test.

4.5 Comparison of two- and three-layered tests

To clearly show the differences between the single connector tests with two and three layers, results from the different tests investigated are plotted together in this section.

4.5.1 Cross

All results from the cross tests are plotted together in Fig. 4.31. Results from different loading directions are plotted in their own figures so that the differences between the specimen types are more visible.

For the tension loaded specimens, presented in Fig. 4.31a, the type 3 tests showed the highest forces, and the highest ductility. The two-layered cross showed the same ductility but significantly lower forces than the type 3 tests. The type 2 cross showed the same forces as the two-layered tests but with lower ductility. The repeatability was acceptable for all the tension loaded cross tests.

The three-layered tests had a higher initial stiffness than the two-layered. This initial linear part of the force-displacement curve up to 1 mm displacement is assumed to be related to elastic deformation. In the three-layered tests, the middle plate stiffens the area around the screw hole, which increases the stiffness of the connection.

Recall, cross type 2 had two plates in the top layer, while type 3 had two plates in the

bottom layer. Both types failed due to thread stripping, but higher forces were registered in type 3 tests. This may be due to the increased stiffness around the hole in the bottom plate, which in order increase the thread stripping resistance.

Pure shear loaded test results are presented in Fig. 4.31b. More scatter was observed for the shear tests than for tension tests, but the trends are still discernable. The type 3 cross showed the highest forces. This is assumed to be related to the middle plate that increase the thread stripping resistance in the type 3 tests. The increased thread stripping resistance results in higher bearing pressure in the top plate which in order leads to end tear-out failure. It is observed that the ductility was slightly higher in type 3. This is also assumed to be caused by the increased thread stripping resistance and corresponding failure mode. The type 2 showed the lowest ductility, but the second highest forces. The type 2 failed due to fracture in the screw. The low ductility but high forces is assumed to be caused by the plastic work and fracture of the screw itself. The two-layered specimens showed low forces, but high ductility.

Deformation of the mixed type 2 cross tests were almost identical to the two-layered tests. Fig. 4.22 compared to Fig. 4.9 show the similarities. As seen in Fig. 4.31c the force-displacement curves for the two tests were similar. In the mixed loading tests the highest forces were registered for the type 3 specimens. This was expected since the type 3 showed the highest forces for the other two configurations as well, and is assumed to be related to the middle plate that increase the thread stripping resistance of the connection.
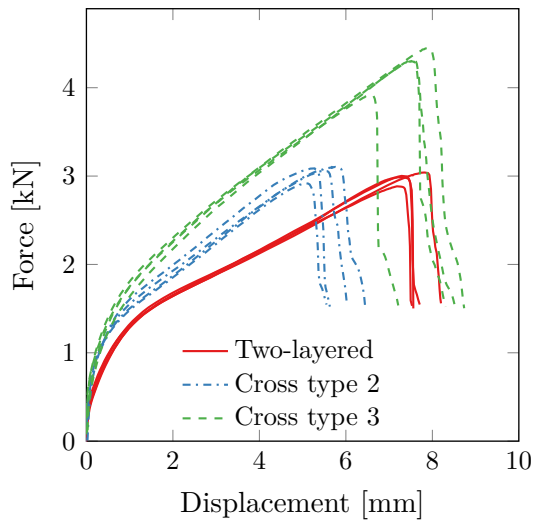
(a) Tension.
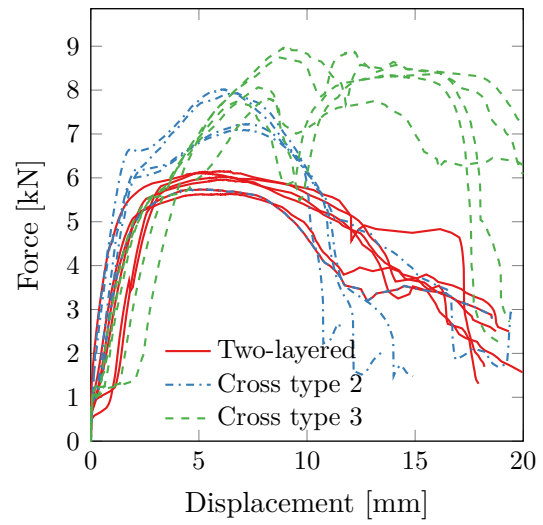
(b) Shear.
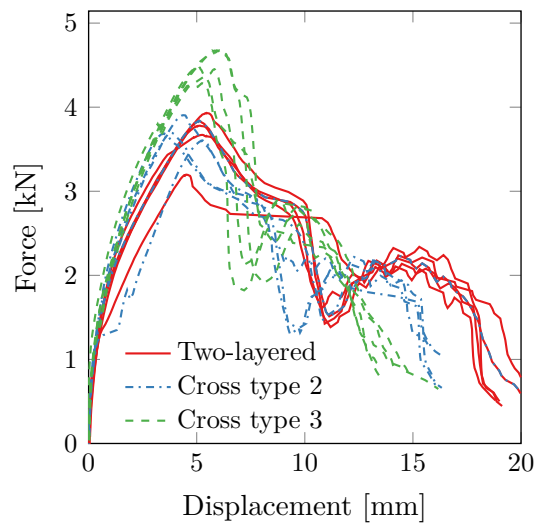
(c) Mixed.

Figure 4.31: Comparison of all cross tests.

4.5.2   Lap-joint

In Fig. 4.32 results from all lap-joint tests are presented. The three-layered tests showed a obvious slipping plateau, where the force was kept constant between 1 mm and 4 mm. Otherwise the tests were very similar. Similar initial stiffness and maximum force were reached and the displacement was the same for both, if the slipping in the three-layered tests was omitted.

A difference in how the two tests reached maximum force was observed. The two-layered steadily increased the force until maximum load was reached, before it slowly decreased to approximately 75% of maximum load, where the connection failed due to thread stripping. The three-layered tests, if the slipping phase is omitted, steadily increased up to about 80% of maximum load, before the force slowly increased up to maximum load, where the connection failed due to fracture of the screw itself. This difference is assumed to be related to the plastic deformation of the screw. The screw in both tests had plastic deformations, but only the three-layered fractured. It is likely that the increased distance between the head of the screw and the bottom plate in combination with the stiffness contribution from the middle plate introduced higher bending forces in the screw. This led to earlier yielding in the screw.
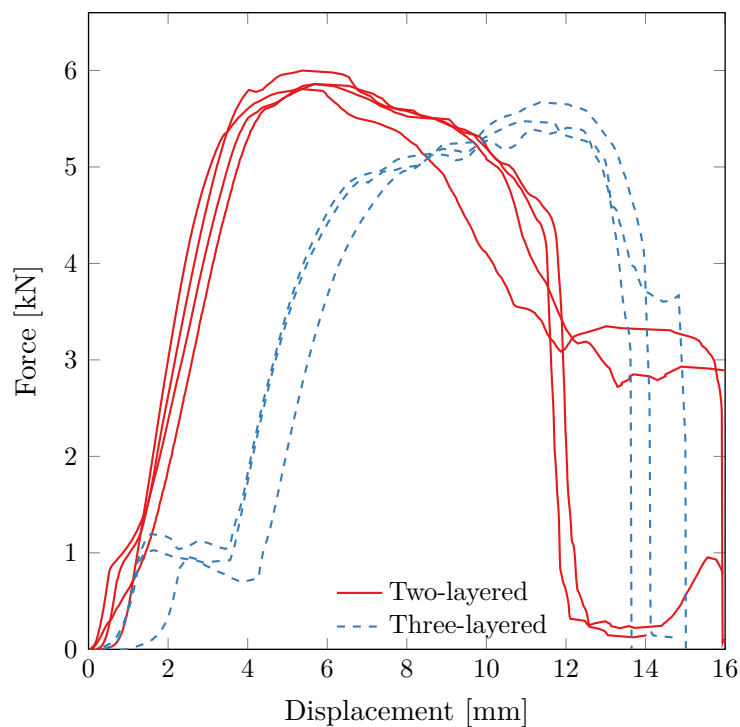
Figure 4.32: Comparison between two- and three-layered lap-joint.

4.5.3 Peeling

The results from both two- and three-layered peeling tests are plotted together in Fig. 4.33. The similarities are evident, both in terms of force and displacement, and the deviation within each test type were higher than the deviation between the different types. The deformation was also very similar, as can be seen by comparing Fig. 4.14 and Fig. 4.30.
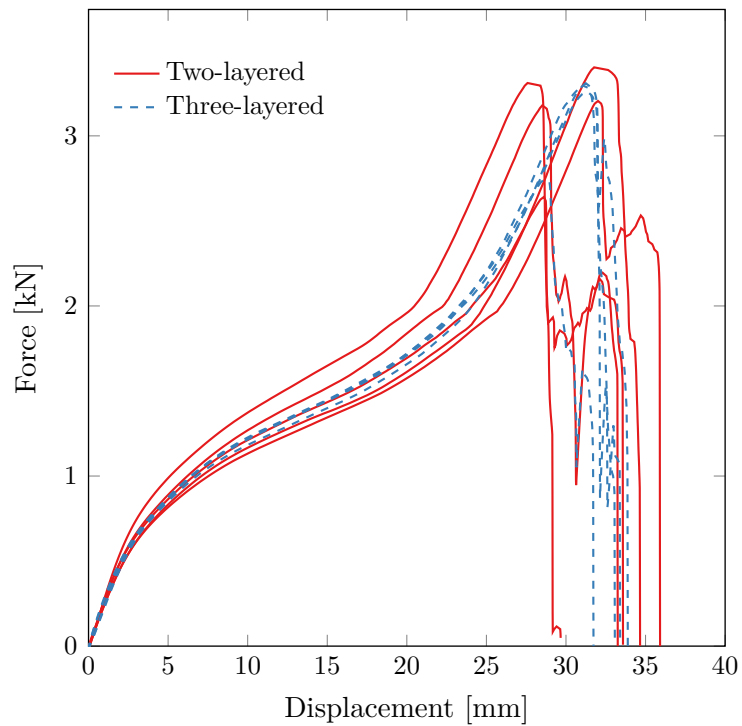
Figure 4.33: Comparison between two- and three-layered peeling tests.

4.6   Concluding remarks

Material tests

- Uniaxial tension tests in seven material directions, plane strain tension and in-plane single shear tests were performed on the extruded aluminium alloy 6063 in T6 condition.

- High repeatability and little scatter were generally observed in all tests.

- In the UT tests some anisotropy in flow stresses and plastic flow was observed.

- DIC results from ISS tests validated the method and the extensometer results.

Uniaxial screw tests

- Uniaxial tension tests of the Flow-Drilling Screw used in the experiments were performed.

- The tests showed that the screw had a high tensile yield strength of 1105 MPa, little hardening and high ductility.

Single connector tests

- Three different cross test types in three different loading configurations, lap-joint and peeling tests with both two and three layers were carried out.

- Generally little scatter were observed in the tests, and the repeatability was acceptable.

- Shear dominated loading situations gave generally higher forces than tensile dominated loading.

- In two-layered cross tests, the pure shear loaded specimens experienced twice as high forces as the tensile loaded.

- The tensile dominated specimens generally failed in thread stripping.

- Cross type 2 in pure shear and three-layered lap-joint failed due to fracture of the screw itself between the top and middle plate.

- Type 3 cross tests in pure shear failed in end tear-out as the top layer yielded.

- The type 3 cross tests showed the highest forces of all cross tests in all loading configurations.

- Generally comparing results from two- and three-layered tests the same trends are discernable.

- Very similar results were registered for lap-joint and peeling tests comparing two- and three-layered tests.

- Relative sliding between the top and bottom layer was observed for the shear and mixed loaded tests due to the pre-drilling of the top sheet.

Component tests

- A component with six screw connections was tested. Little scatter was observed, and the repeatability was acceptable.

- All screws in the connections experienced both rotation and one-sided thread stripping.

- Failure occurred in the bottom screw first, and the two others on the same side failed shortly after. Only the screws on one side failed in each test.

- Failure of the test rig occurred in two of the tests. The tests showed no sign of plastic deformation, and were repeated with good results. More component tests should be conducted to validate the tests done in this thesis.

Chapter 5

Material model

The YLD2004-18p anisotropic yield criterion of Barlat et al. [28] together with the Voce isotropic hardening rule was used to represent the material behaviour of the alloy. The constitutive model was calibrated to fit the experimental data of the extruded and heat treated aluminium alloy 6063. The SIMLab developed software MatPrePost was used to perform the calibration. The parameter identification and validation procedure is described in the following.

5.1 Parameter calibration

In this section the yield function and initial hardening parameters are obtained. Theory on the yield function is presented in Section 2.4.1, and the Voce isotropic hardening law is presented in Section 2.4.2.

To calibrate the material model and hardening parameters, force-displacement curves from the seven different directions of UT tests were imported to MatPrePost together with width and thickness measurements of the specimens prior to, and after the tests. After evaluating all material tests, a Young's modulus, $E = 70\,000\,\mathrm{MPa}$ and a Poisson's ratio, $\nu = 0.35$ were chosen for all calibrations.

The calibration of yield function parameters is an optimisation problem. The MatPrePost algorithm finds local minima of an error function. Whether or not the parameters for the local minimum gives a physically admissible yield surface is merely up to the user to

73

evaluate. Three sets of parameters were obtained that were all local minima of the error function, and that were evaluated to be physically admissible. The parameters for each calibration can be seen in Table 5.1. A comparison of the yield surfaces of the different calibrations is shown in Fig. 5.1 and Fig. 5.2. The red dots in the figures represent r-values, and the respective arrows indicate the R-values for the actual test direction. The biaxial plastic strain ratio, R_b, calculated from Eq. (2.25), was set to 2.16 for all calibrations. The effect of this can be seen in Fig. 5.1, as the gradient in the equibiaxial point (the green dot) is clearly affected. The equibiaxial point value was constrained to 1 for all calibrations.
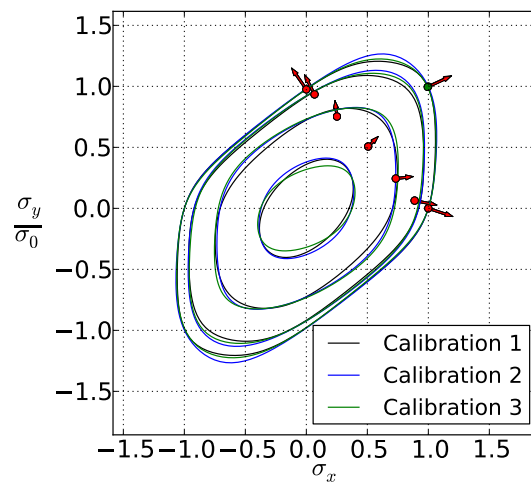
Figure 5.1: Yield surfaces for intersections at constant shear stress σ_{xy}.
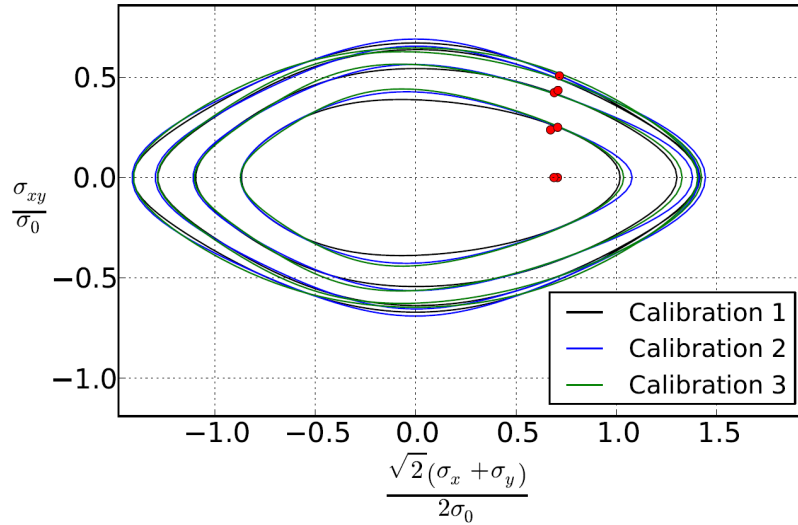
Figure 5.2: Yield surfaces for intersections of planes with normal vectors, in the direction of the line $\sigma_x + \sigma_y = 0$.

R-values, calculated using geometrical measurements before and after the uniaxial tensile tests in Eq. (2.22), are shown as red dots in Fig. 5.3, along with continuous strain ratio functions proposed by MatPrePost. MatPrePost calculates the uniaxial tension flow stress ratios from the experimental data, shown in Fig. 5.4. The anisotropy in flow stress is clearly visible. It is also evident that the r-values evolve during plastic work, which is not in accordance with the assumption of isotropic hardening. The average flow stress ratios, calculated from Eq. (2.23), as well as the calibrated functions are presented in Fig. 5.5.

Calibration 3 was chosen to represent the material in the single-connector simulations. Criteria when choosing calibration for the material model were firstly how well the R- and r-ratios were estimated. The physical appearance of the yield surface was also evaluated. The chosen yield surface is shown in Fig. 5.6 and Fig. 5.7. A comparison between the chosen yield surface and the von Mises' yield surface is shown in Fig. 5.8.

Initial hardening parameters of the Voce isotropic hardening rule were calibrated. The representative curve from the 0-direction was used, and the same hardening parameters were applied to all calibrations. The hardening parameters were optimised using LS-OPT, a design optimisation software with interface for LS-DYNA. The parameters are optimised by comparing simulations of the UT tests with the experimental force-displacement curves. For more information on the optimisation algorithm, the interested reader is referred to [41]. Initial as well as optimised hardening parameters are shown in Table 5.2. In the optimisation, parameters Q_{R3} and C_{R3} are set to 0, because the third part of the Voce

equation did not affect the results.

Table 5.1: Material model parameters.

Calibration	1	2	3
a	8	8	8
c'_{12}	1.5121	0.9896	0.8522
c'_{13}	-1.3195	1.9660	1.0751
c'_{21}	0.8203	1.0480	-0.4526
c'_{23}	-0.1875	0.7198	0.5674
c'_{31}	2.2918	-0.8118	0.6819
c'_{32}	2.1796	-0.1172	-0.103
c'_{44}	0.5523	0.3187	1.0028
c'_{55}	1.0000	1.0000	1.0000
c'_{66}	1.0000	1.0000	1.0000
c''_{12}	0.9326	0.2142	1.3515
c''_{13}	-0.4659	1.8680	0.1048
c''_{21}	-0.7087	0.7262	0.6805
c''_{23}	-0.9203	1.7360	1.6428
c''_{31}	0.3878	-0.3315	0.9797
c''_{32}	1.6197	0.6899	0.5372
c''_{44}	1.0661	1.2300	0.6809
c''_{55}	1.0000	1.0000	1.0000
c''_{66}	1.0000	1.0000	1.0000
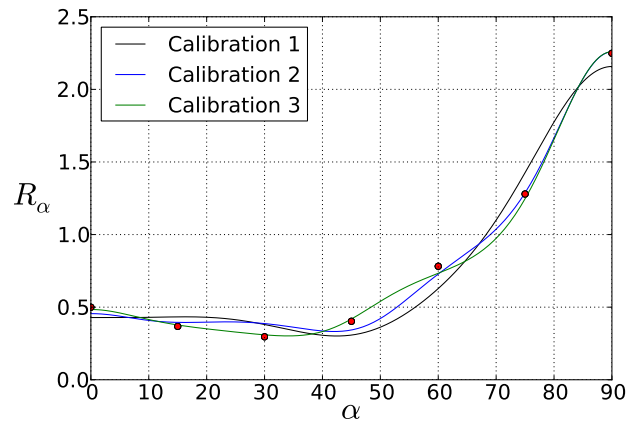
Figure 5.3: R-values as a function of material orientation.

Table 5.2: Hardening parameters used in the material model.

Parameter	Initial calibration	LS-OPT
σ_0	204.6 MPa	204.6 MPa
Q_{R1}	4.923 MPa	12 300 MPa
C_{R1}	1.005	7.986 x 10^6
Q_{R2}	70.84 MPa	1472.6 MPa
C_{R2}	1121	5.4972 x 10^7
Q_{R3}	1442 MPa	0
C_{R3}	-0.0011	0
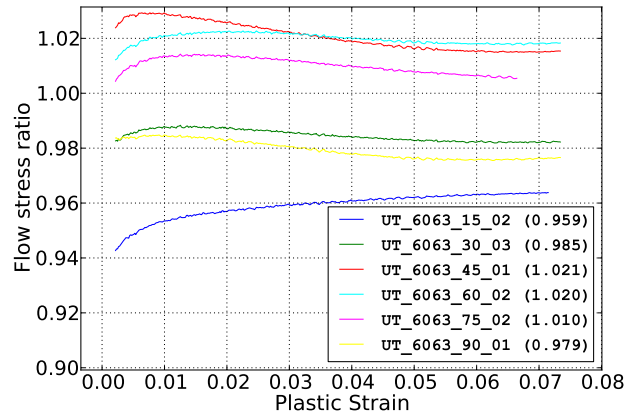
Figure 5.4: Uniaxial tension flow stress ratio as a function of plastic strain. Average value in parentheses.
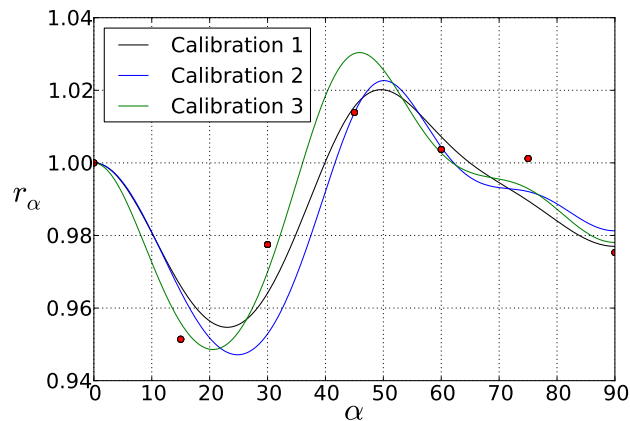
Figure 5.5: Uniaxial flow stress ratios as a function of material orientation.
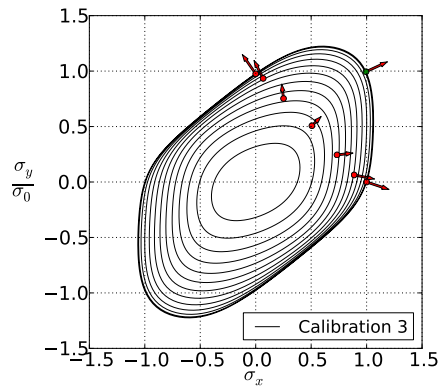
Figure 5.6: Yield surface for intersection at constant shear stress σ_{xy} for calibration 3.
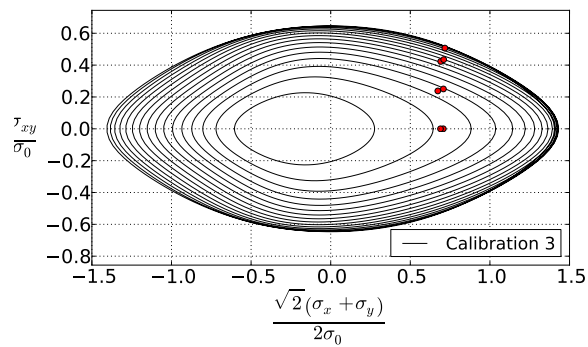
Figure 5.7: Yield surface for intersection of planes, with normal vectors along the line $\sigma_x + \sigma_y = 0$ for calibration 3.
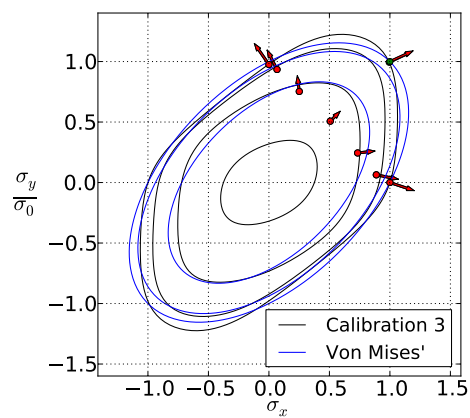
Figure 5.8: Comparison between chosen yield surface and von Mises'.

5.2 Validation

To validate the constitutive model, numerical simulations of UT, PST and ISS were performed. The material model was calibrated using UT experimental results. The PST and the ISS represented validation of the constitutive model. All numerical analyses were performed with the finite element code LS-DYNA. In all simulations, reduced integration was applied. Time scaling was applied since the material model was rate independent. When time scaling is used, an energy check is necessary. The kinetic energy was compared to the internal energy, showing no significant kinetic energy in any simulation. Hourglass control number 6 was applied to all simulations, and monitored closely. No significant artificially introduced energy was observed in any of the simulations. For information on the hourglass control, the interested reader is referred to the LS-DYNA user's manual [42].

5.2.1 UT simulation

In the numerical model of the UT specimen nominal measures were applied. To save CPU costs both thickness and width symmetry were utilised, resulting in a model consisting of only one fourth of the specimen geometry. A visualisation of the model can be seen in Fig. 5.9.
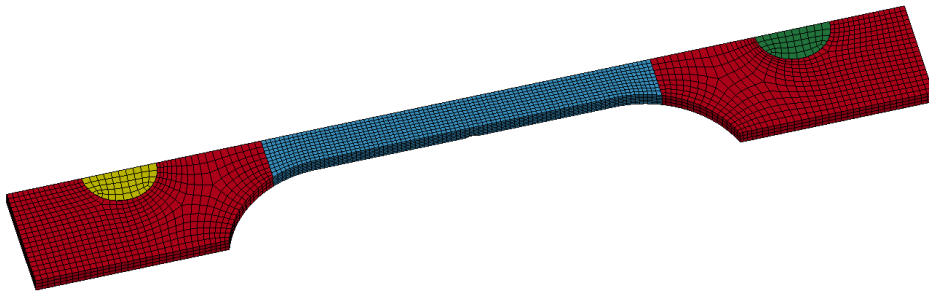
Figure 5.9: Finite element model of the UT specimen.

The pins were modelled as rigid (*MAT020), while the investigated material model was used in the specimen. Since a finer mesh was applied in the central part of the specimen, a surface to surface contact formulation was used to tie the parts together (*CONTACT_TIED_SURFACE_ TO_SURFACE). A contact formulation was also needed between the pins and the specimen, an automatic node to surface formulation was used

(*CONTACT_AUTOMATIC_NODES_ TO_SURFACE). The geometry was discretised using 9048 solid elements, where 5220 were localised in the middle part. The mesh of the UT specimen was coarser than the other models to save computational time in the optimisation of the material parameters. The smallest elements were approximately $0.31\,\text{mm} \times 0.16\,\text{mm} \times 0.25\,\text{mm}$ in the longitudinal, thickness and transverse direction, respectively. The load was applied as prescribed motion of one of the pins in the longitudinal direction of the specimen using a smooth curve. In Fig. 5.10 results from experiments and simulation are presented. As seen both stresses and strains were accurately reproduced in the simulation. This was expected since the material model was calibrated with respect to the UT tests.
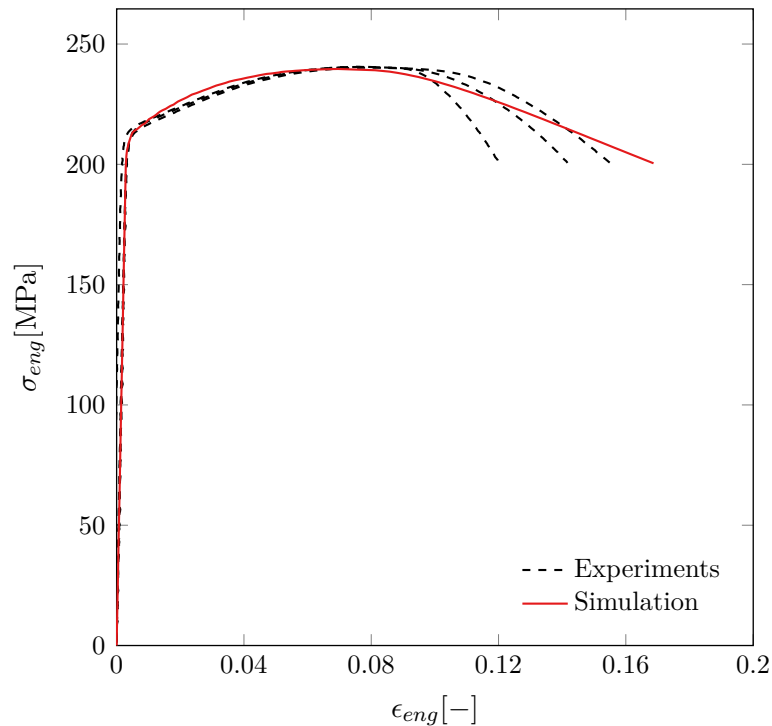
Figure 5.10: Results from UT experiments and simulations.

5.2.2 PST simulation

The nominal geometry was used in the numerical model of the PST specimen, shown in Fig. 5.11. As can be seen, transverse symmetry was used to model only half of the width, to reduce the number of elements needed in the analysis. Additionally through thickness symmetry was applied. This resulted in a model consisting of 21144 solid

elements, where 16224 elements were located in the middle part. The smallest elements were approximately $0.28\,\text{mm} \times 0.16\,\text{mm} \times 0.31\,\text{mm}$ in the longitudinal, thickness and transverse direction, respectively.
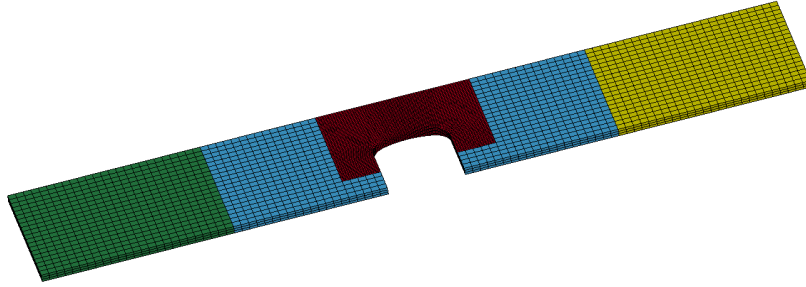
Figure 5.11: Finite element model of the PST specimen.

The end parts were modelled as rigid, corresponding to the part of the specimen clamped to the test machine. The deformable parts were modelled with the calibrated material model. The load was applied as prescribed motion of one of the clamped parts in the longitudinal direction of the specimen using a smooth curve. In Fig. 5.12 experimental and numerical PST results are plotted together. The simulation over-estimates the maximum load by approximately 2.5%, which is acceptable.
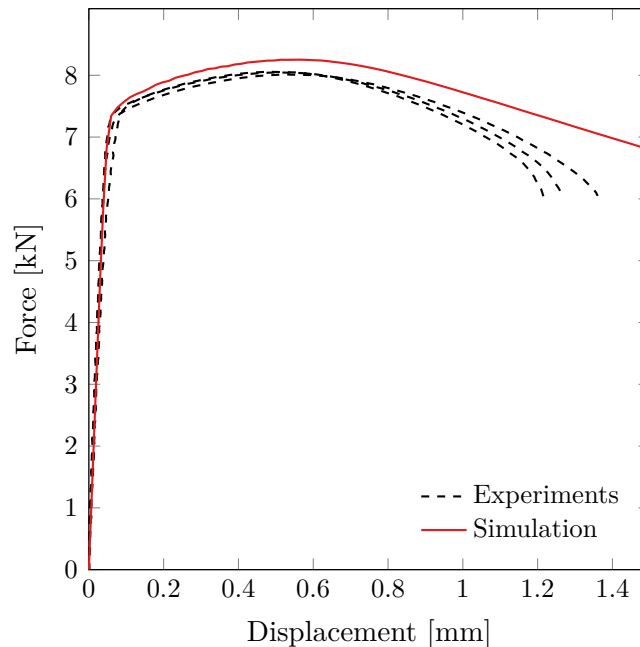
Figure 5.12: Results from PST experiments and simulations.

5.2.3 ISS simulation

The ISS specimen was modelled with nominal geometry. The finite element model of the specimen is shown in Fig. 5.13a, and a close-up of the centre is shown in Fig. 5.13b. The pins fastening the specimen to the test machine were modelled as rigid. The deformable parts were assigned the chosen material model. The geometry enforces the deformation to mainly occur in the central part of the specimen, thus a finer mesh was applied in the middle part, see Fig. 5.13b. A node to surface contact formulation was used to tie the deformable parts together (*CONTACT_TIED_NODES_ TO_SURFACE). The (*CONTACT_AUTOMATIC_NODES_TO_SURFACE) formulation was used to ensure force distribution from the pins to the specimen.
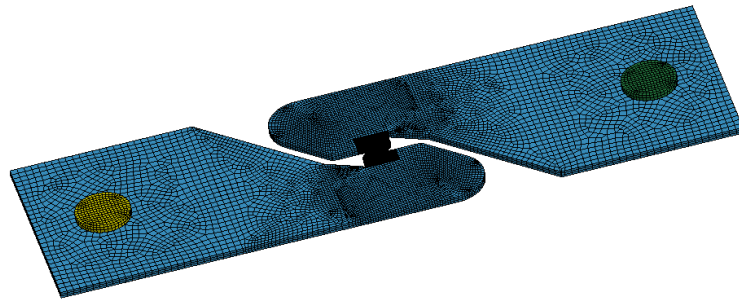
(a) Complete model.
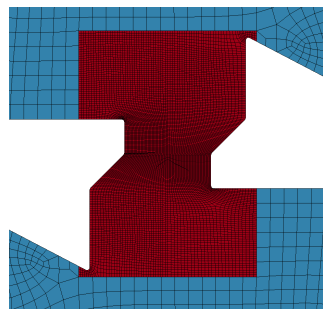
(b) Center part.

Figure 5.13: Finite element model of the ISS specimen.

The complete model consisted of 118842 solid elements, where 92960 were localised in the central part. The smallest elements were approximately $0.015\,\text{mm} \times 0.021\,\text{mm} \times 0.096\,\text{mm}$ in the longitudinal, transverse and thickness direction, respectively. The load was applied as prescribed motion of one of the pins in the longitudinal direction of the specimen using a smooth curve. In Fig. 5.14a force-displacement curves from simulation and the

experiments are shown. Displacement in the simulation was obtained from the same areas as the extensometer in the experiment.

In Fig. 5.14b results from DIC are plotted together with simulation results. The simulation displacement in this figure has been extracted from the same nodes as in the DIC analysis (see Fig. 4.4b), and the relative displacement between them has been calculated. This leads to a stiffer result compared to the results presented in Fig. 5.14a, as there is less material deformation between the measure points. The stiffness is well represented, but the force is over estimated in yielding. This indicates that the calibrated material model is inaccurate in the ISS part of the yield surface, shown in Fig. 2.10.

(a) Extensometer displacement.　　**(b)** Relative displacement.
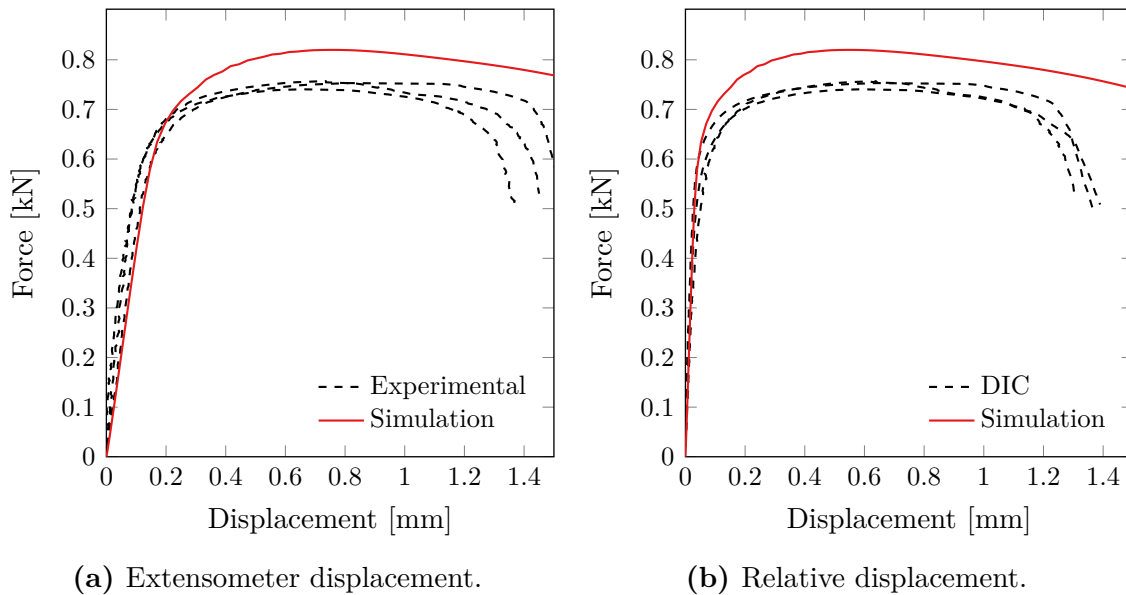
Figure 5.14: Results from ISS simulation.

5.3 Concluding remarks

- The yield function was calibrated to UT tests in seven directions and a disc compression test giving information of the plastic flow in equibiaxial tension. Three different calibrations of the yield function were compared, before one was chosen as the best representation of the material.

- The Voce hardening rule was calibrated to the representative UT test in the 0-direction, using the true stress-plastic strain curve from initial yield to necking.

- The chosen material calibration was validated using UT, PST and ISS experiments and simulations. UT and PST simulations showed satisfying results, while forces were over-estimated for the ISS test. This indicates that the yield surface is close to correct in the PST part shown in Fig. 2.10, but more inaccurate in the ISS part.

Chapter 6

Two-layered macroscopic models

The following chapters present calibration and validation of the different macroscopic models used in this thesis. The macroscopic models are presented in Section 2.2.

When reduced integration was used, the shear-dominated simulations suffered from oscillations, while tensile-dominated simulations were unaffected. Cross tests in tension and peeling tests were therefore simulated using reduced integration and with hourglass control number 4. Cross tests in shear and mixed loading, lap-joint and the component test were simulated using fully integrated shell elements and hourglass control number 8. Both hourglass controls are stiffness based, where number 8 is a control that only applies to fully integrated shell elements to avoid that warping of the element degrades the solution. No significant artificially introduced energy was observed in any simulation. The interested reader is referred to the LS-DYNA user's manual [42] for more information on hourglass controls.

Since time scaling was applied kinetic energy was compared to the internal energy, showing no significant kinetic energy in any simulation. A contact formulation (*CONTACT_AUTOMATIC_SURFACE_TO_SURFACE_ID) was applied between the plates to account for possible contact forces. The friction coefficient was set to 0.2.

6.1   FE models used for calibration

The models were calibrated to the results from the two-layered cross tests, both for the spr2 model and the spotweld model. The material parameters obtained in Chapter 5 were implemented for the sheet material as well as the material directions shown in Fig. 3.6.

The FE model of the cross specimen is shown in Fig. 6.1. The specimen was modelled using the nominal geometry shown in Fig. 3.6 and the measured thickness of the specimen. The model consisted of 2400 3D shell elements with five through-thickness integration points. For the simulations with the spotweld model, 16 solid elements were used for the connector. For each plate 400 elements were part of deformable sections, while 800 rigid elements represented the rigid part of the test setup. All parts were modelled using $2\,\text{mm} \times 2\,\text{mm}$ elements. Simulations of the tests in 45- and 90-degree load direction were done by rotating the mesh used for the pure tension tests.

The rigid parts of the bottom plate were fixed in all directions, while the top plate was given a velocity in the respective loading direction. A smooth curve defined the velocity of the moving part.
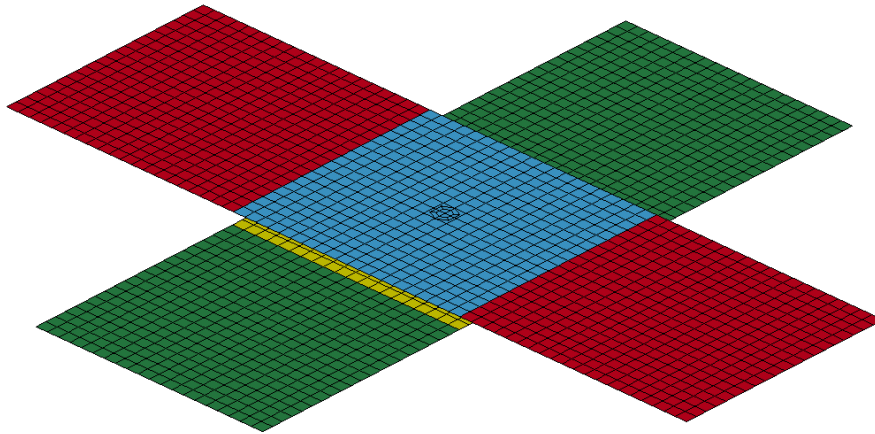
Figure 6.1: FE model of the Cross test specimen.

6.2   The spr2 point-connector model

Calibration of the connector model was done using the optimisation software LS-OPT. The software carried out simulations of the cross tests while varying the parameter values,

and optimising the parameters to fit the numerical force-displacement curves to the experiments. By running numerous simulations and comparing them with the experimental results, a new set of parameters were calculated. This was done in an iterative procedure until the results were satisfying. The results from the optimisation are presented in Table 6.1.

Table 6.1: Optimised parameters for the spr2 point-connector model for two-layered connections.

Parameter	Value	Unit	Description
f_n^{max}	2900	N	Maximum pure normal force
f_t^{max}	6000	N	Maximum pure shear force
δ_n^{fail}	5.2	mm	Deformation at failure for pure normal load
δ_t^{fail}	16	mm	Deformation at failure for pure shear load
ξ_n	0.72		Start of softening for pure normal deformation
ξ_t	0.45		Start of softening for pure shear deformation
$\alpha 1$	0.2		Initial value of the damage parameter α
$\alpha 2$	0.8		Value of α when softening starts
$\alpha 3$	1		Final value of α
d	12	mm	Diameter

In Fig. 6.2 simulation results with the calibrated connector model are presented. As seen, the connector model was able to reproduce both maximum load and failure in an accurate manner for tensile (Fig. 6.2a), shear (Fig. 6.2b) and mixed (Fig. 6.2c) loading condition. However, the model was not able to describe the two nearly linear parts of the force displacement curve from tensile load.
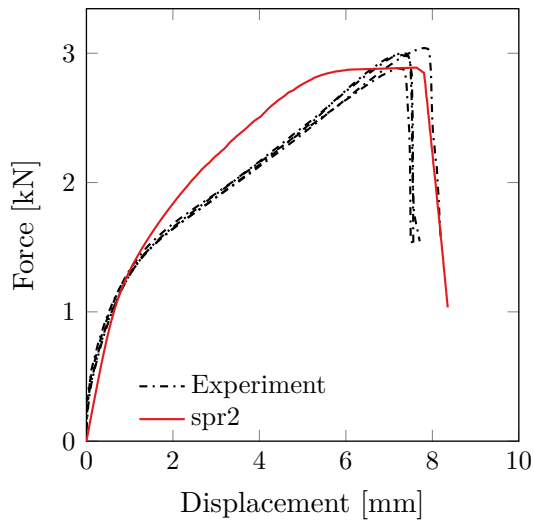
(a) Tension.
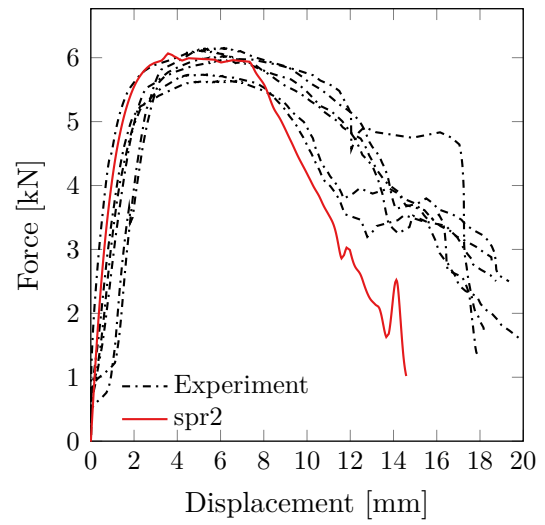
(b) Shear.
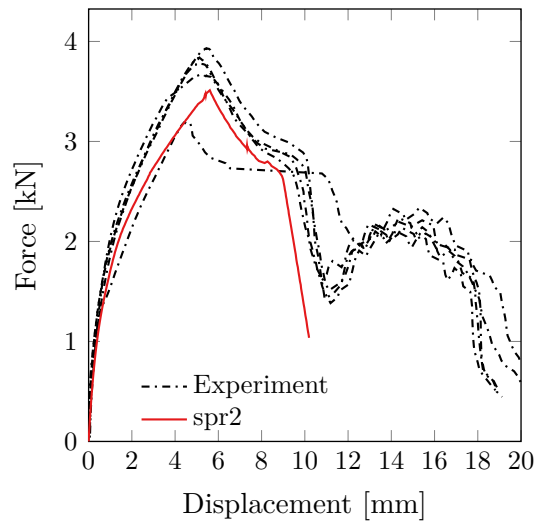
(c) Mixed.

Figure 6.2: Calibration results from the spr2 model.

6.3 The spotweld macroscopic model

In this thesis 16 element connectors are used for all simulations. Initial simulations showed no increase in computational time compared to the 8 element connector, and Malcolm et al. [23] states that even though the difference is small, the 16 element connector performs better than the 8 element connector.

6.3.1 Material parameter sensitivity analysis

Few studies regarding the parameters in the keyword file was found. In order to better understand the spotweld model, a sensitivity analysis covering material parameters of the connector and the connector diameter was conducted. To analyse the material parameters of the spotweld model, all failure criteria were excluded. The aim of the analysis was to understand the effects of the different parameters. The spotweld model was developed for spot welds and not screwed connections. Therefore, the effect of the parameters when used for screws were not certain. A default set of parameters was determined as a basis for the sensitivity analysis. The default parameter values were chosen as a steel screw with high yield stress, shown in Table 6.2. All parameter changes were done in both tension and shear, to see the combined effect of each parameter.

Table 6.2: Reference values for the spotweld macroscopic model.

Parameter	Reference value	Description
d	4 mm	Diameter
E	210 000 MPa	Young's modulus
E_t	500 MPa	Hardening modulus
σ	1000 MPa	Initial yield stress
ν	0.3	Poisson's ratio

Diameter of the connection

Fig. 6.3 shows the effect of changing the diameter of the connector. Smaller diameter led to a reduction in force for both tension and shear. This was expected, as a smaller connector will lead to greater stress in both the connector and the plate material, thus yielding will occur for a lower force. Apart from the reduction in forces, the simulation with the 3 mm connector in shear stood out. The connector yielded more abruptly than the other simulations. The yielding was similar to that of steel, while the others were similar to aluminium. It seems that the 3 mm connector in shear experienced yielding in the connector itself, while the other connectors experienced yielding in the sheet material. The linear increase in force observed after yielding in the 3 mm shear connector would then be the hardening of the connector material, before the sheet material yielded after about 5 mm displacement.
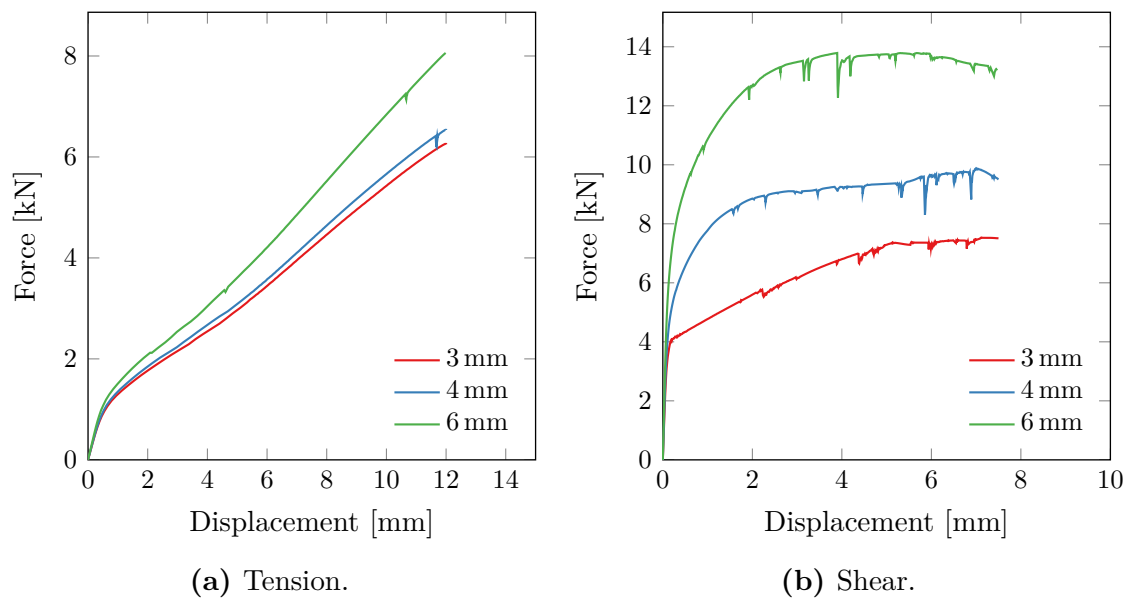
(a) Tension.

(b) Shear.

Figure 6.3: Sensitivety of diameter.

Young's modulus

The effect of changing the Young's modulus, E, is shown in Fig. 6.4. As can be seen in both shear and tension, no particular change in the force-displacement curves were observed, only a small reduction in stiffness in the shear simulation with $E = 50\,000\,\text{MPa}$. It is believed that both the elasticity and yield parameters of the aluminium sheets were the decisive factor in all simulations. To better observe the effect of change in Young's modulus in the connector, simulations should be conducted with parameters where the Young's modulus of the connector is decisive.

(a) Tension.

(b) Shear.
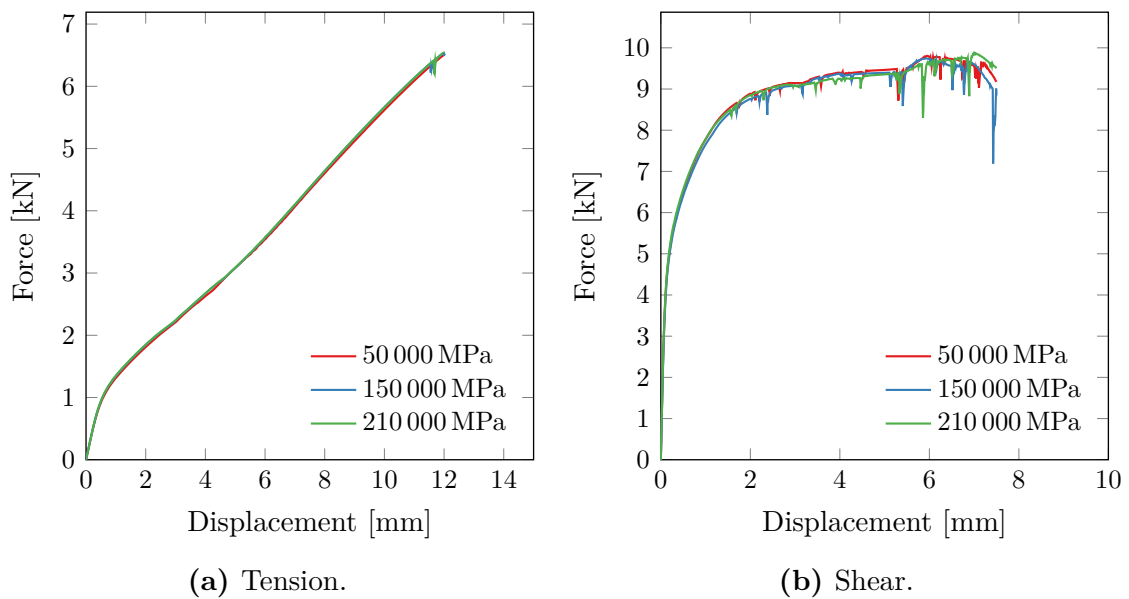
Figure 6.4: Sensitivety of Young's modulus.

Hardening factor

The comparison between different hardening factors are shown in Fig. 6.5. As for the Young's modulus, changes of the parameter gave very little indication of how the global behaviour was affected. In shear it can be seen that the hardening factor of $E_t = 100\,\mathrm{MPa}$ led to less hardening than in the two other simulations. In the tension simulations no difference was observed. The reason is probably the same as for the analysis of the Young's modulus, the material parameters of the plates were decisive for the behaviour.

(a) Tension.

(b) Shear.
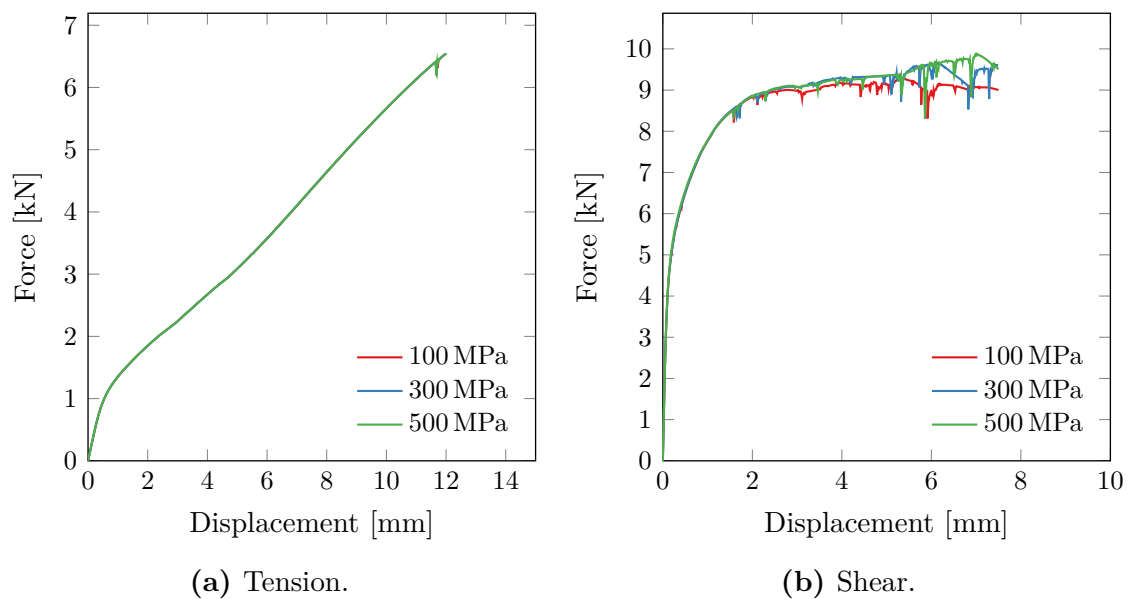
Figure 6.5: Sensitivety of hardening modulus.

Yield stress

Fig. 6.6 shows the impact of change in yield stress of the connector. As for the stiffness parameters, the tension simulation results were not affected as the yield stress of the connector was altered. For shear however, the change in yield stress showed a clear difference in the results. The increase to $\sigma = 1500\,\text{MPa}$ increased the force slightly, while the decrease to $\sigma = 500\,\text{MPa}$ showed a clear change in the force-displacement curve. As for the decrease in diameter, the form of the curve was similar to a steel material with a high hardening factor. This indicates that yielding occured in the connector for $\sigma = 500\,\text{MPa}$, and in the sheet material for the other values. As in the analysis of the diameter, the connector experienced hardening until yielding in the sheet material occurred.

(a) Tension.

(b) Shear.
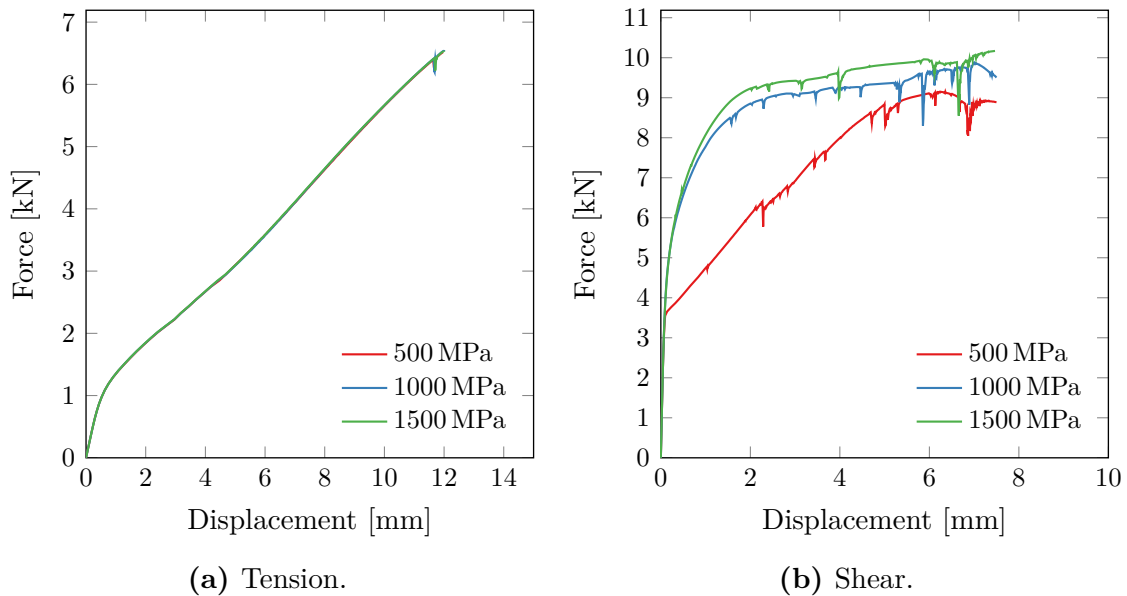
Figure 6.6: Sensitivety of yield stress.

6.3.2 Optimisation of the spotweld model

An optimisation was conducted to find a set of parameters that would give an accurate representation of the experimental tests. Simulations with varying parameters in the macroscopic model were carried out to fit the force-displacement curves from the experiments. For the spotweld model this was done manually unlike the optimisation of the spr2 model. The result of the optimisation is shown in Table 6.3.

Table 6.3: Optimised parameter values for the spotweld macroscopic model.

Parameter	Optimised value	Description
d	$1.5\,\mathrm{mm}$	Diameter
E	$10\,000\,\mathrm{MPa}$	Young's modulus
E_t	$50\,\mathrm{MPa}$	Hardening modulus
σ	$5200\,\mathrm{MPa}$	Initial yield stress
ν	0.3	Poisson's ratio
ϵ_{fail}	0.1	Effective plastic strain in weld material at failure.
N_{rr}	$250\,\mathrm{N}$	Axial force resultant at failure
N_{rs}	$800\,\mathrm{N}$	Shear force resultant at failure
N_{rt}	$800\,\mathrm{N}$	Shear force resultant av failure

In Fig. 6.7 simulation results with the calibrated spotweld macroscopic model are presented. As seen from the tension results in Fig. 6.7a, the model with the failure criterion was able to reproduce both forces and displacement with acceptable accuracy. The difference in behaviour with and without the failure criterion enabled was only observed at and after failure. The results from the pure shear loading analysis are presented in Fig. 6.7b. In these simulations the stiffness and the force were under-estimated. The failure criterion was too strict, as failure occurred too soon. Fig. 6.7c shows the simulation results from the mixed loading. It is seen that the spotweld model slightly over-estimated the forces in this configuration, but the accuracy is arguably acceptable. Failure of the connection occurred too soon, as for the shear loaded cross test.
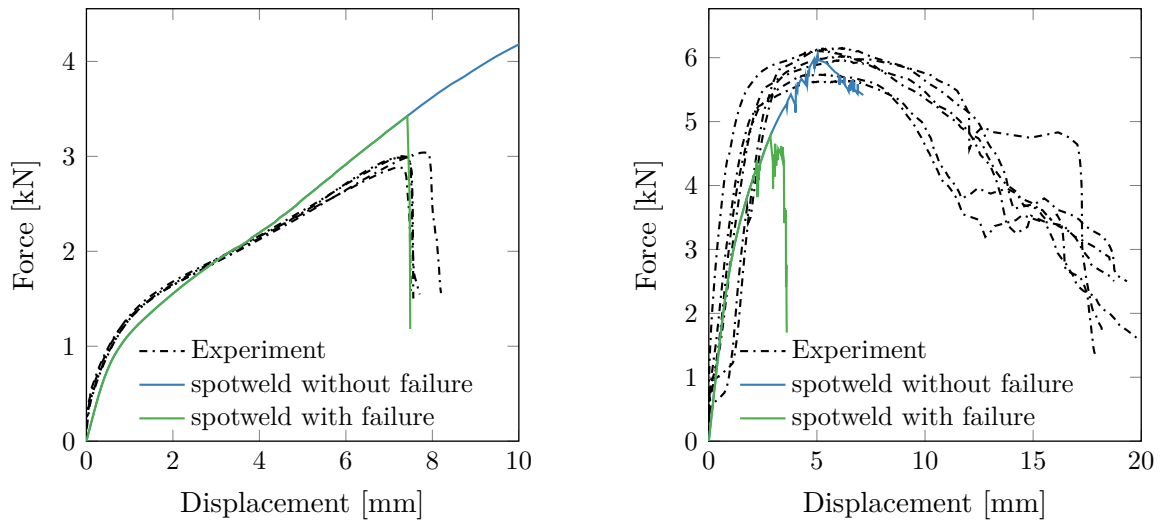
(a) Tension.

(b) Shear.
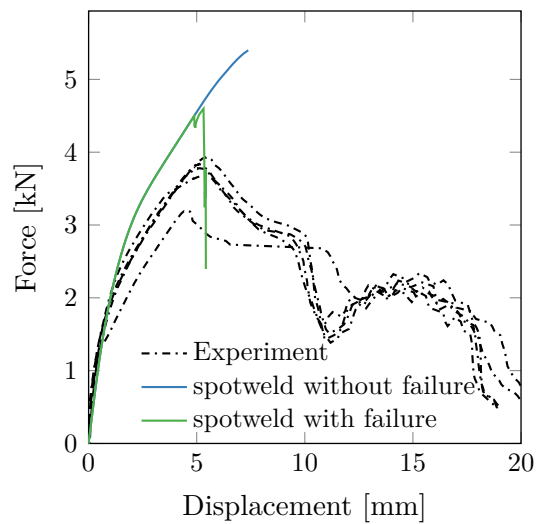
(c) Mixed.

Figure 6.7: Calibration results from the spotweld model.

Even though no changes were seen in the sensitivity analysis for different values of Young's modulus and hardening factor, an effect of the stiffening factors was observed in the optimisation. When the material of the connector yielded first, a stiffer behaviour after yielding was observed when an increased hardening factor was applied. Also, when Young's modulus of the connector material was decisive for the initial stiffness, a higher stiffness was observed for higher Young's modulus. An analysis conducted with the optimised parameters as a reference could give more answers to how the parameters affect the connection. This could in turn lead to better knowledge of how to make a better optimisation, and is suggested for future work.

6.4   Comparison between the macroscopic models

To clearly show the differences between the calibrations of the connector models, all results are presented in Fig. 6.8. In Fig. 6.8a simulation results from tension loaded specimens are shown, while the shear and mixed configurations are presented in Fig. 6.8b and Fig. 6.8c, respectively. As seen, the spr2 point-connector produced best results in all configurations. Both maximum load and displacement at failure were better reproduced with this model. Sommer et al. [24] observed similar results in their work. One reason to this is assumed to be due to the optimisation process. The spr2 point-connector model was optimised with use of LS-OPT while the spotweld model was optimised manually. An optimisation of the spotweld model using LS-OPT is proposed for future work.

(a) Tension.

(b) Shear.

(c) Mixed.
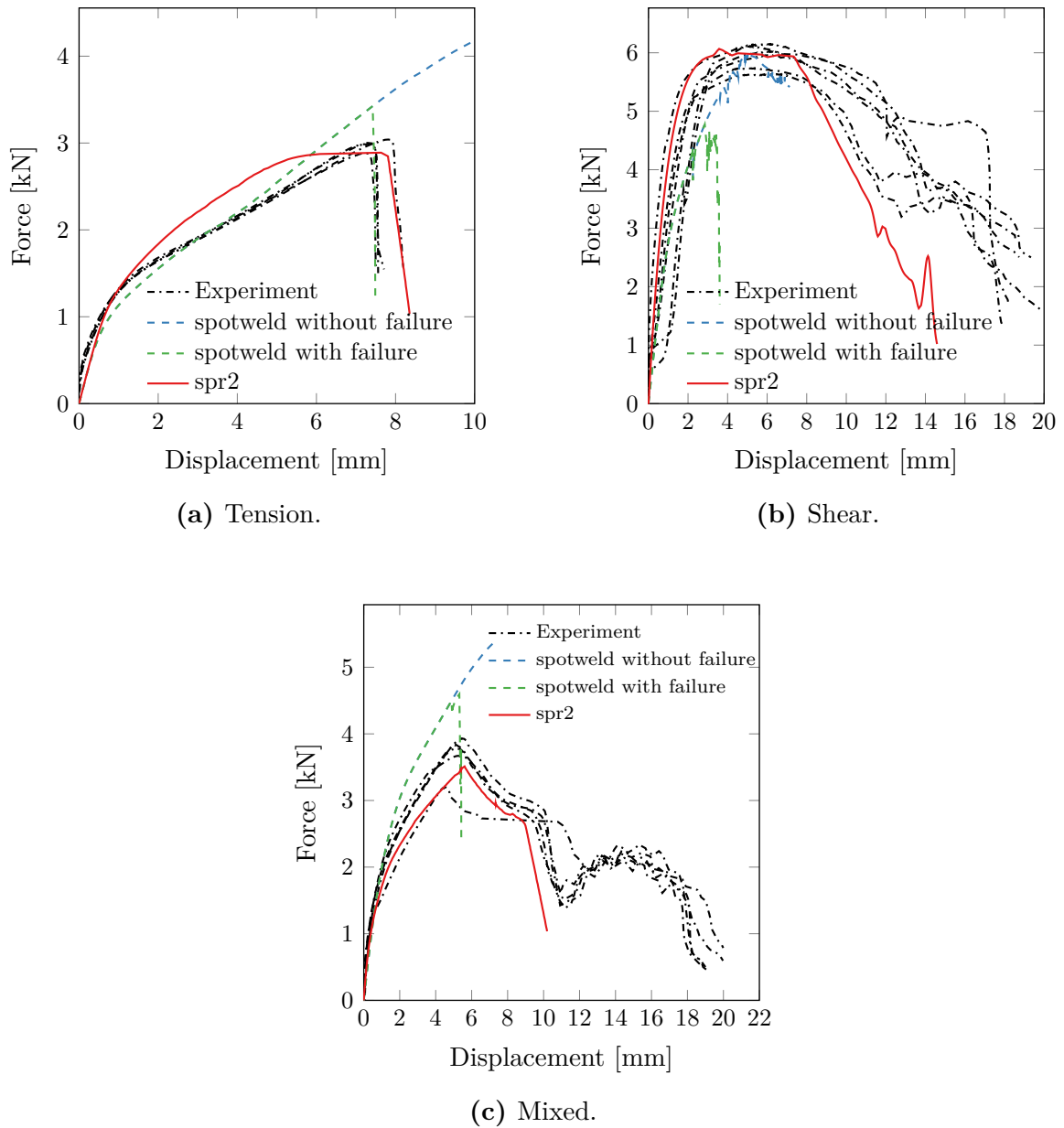
Figure 6.8: Comparison between calibrated models.

6.5 Validation of two-layered macroscopic models

In this section the calibrated macroscopic models for the two-layered connections are validated. Validation was done using the lap-joint, peeling and component tests. The results from both the spr2- and the spotweld models are plotted together, to highlight the difference between the models.

6.5.1 Lap-joint

The FE model is shown in Fig. 6.9. The specimen was modelled using the nominal geometry shown in Fig. 3.8 and the measured thickness. The model consisted of 1720 3D shell elements with five through-thickness integration points, where 1400 elements were part of deformable sections and 320 elements were part of rigid sections. The clamping in the experiments was represented by the rigid parts, with 40 mm of each plate modelled as rigid. This corresponded to the clamped parts in the experiments. The rigid parts were modelled using $2\,\text{mm} \times 5\,\text{mm}$ elements, while the deformable parts were modelled using $2\,\text{mm} \times 2\,\text{mm}$ elements. One of the ends was fixed in all directions, while the other was given a velocity in the longitudinal direction. A smooth curve was used to apply the velocity.
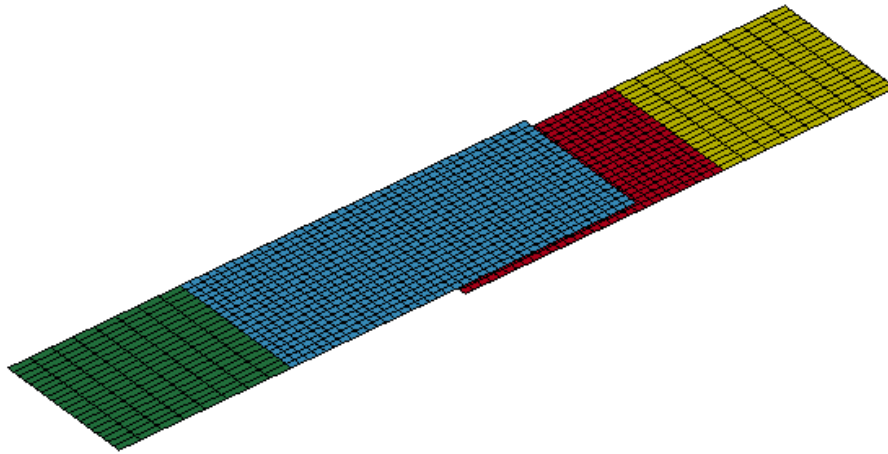
Figure 6.9: FE model of lap-joint specimen.

Results from the lap-joint simulations compared to the experiments are shown in Fig. 6.10. Both simulations over-predicted the force early in the test. This was due to flexibility in the test set-up as well as the relative sliding discussed earlier. Accounting for this, the stiffness was well represented. The spr2 model was able to represent acceptable yield and failure in the connection, while the spotweld model failed too early. The early failure in the spotweld model was likely caused by rotation of the connector, leading to tensile forces. Since the capacity in tension was lower than in shear, the failure function reached the total capacity too early. A model using a connector with larger diameter could avoid this problem. A bigger connector would be less prone to rotation, because of the increased stiffness. In this thesis a small connector was used to lower the forces in the connection. A different set of parameters may have been able to increase the stiffness of the connection

while representing correct forces. The more sophisticated spr2 model includes mixed interaction parameters, which may explain the better results.
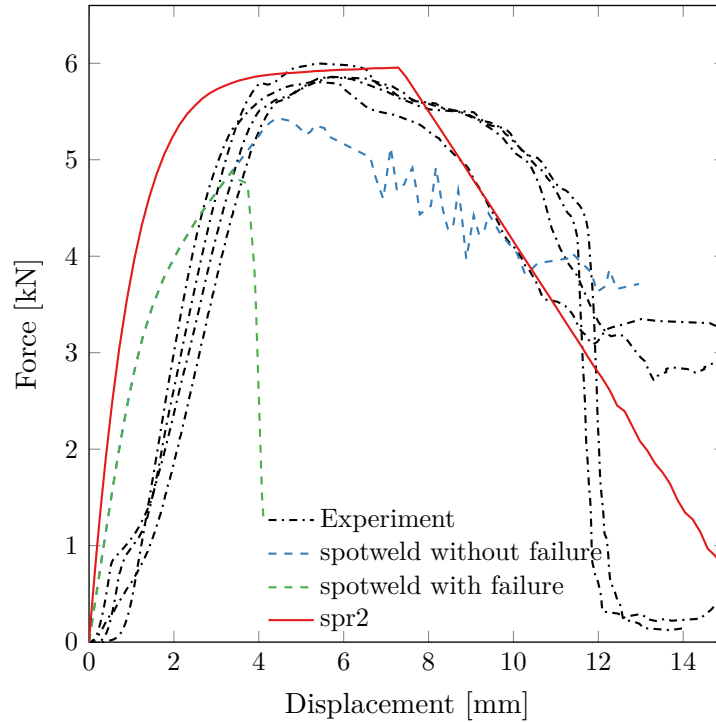
Figure 6.10: Simulation results from the lap-joint test.

6.5.2 Peeling

The FE model is shown in Fig. 6.11. The specimen was modelled using the the nominal geometry shown in Fig. 3.9 and the measured thickness. The model consisted of 2200 3D shell elements with five through-thickness integration points, where 1600 elements were part of deformable sections, and 600 elements were part of rigid sections. As in the peeling tests, the clamping was represented by the rigid parts, with 40 mm of each plate rigid, corresponding to the clamped parts in the experiments. Element sizes for rigid and deformable parts were the same as in the lap-joint model. One of the ends was fixed in all directions, while the other was given a velocity in the longitudinal direction. A smooth curve was used to apply the velocity.
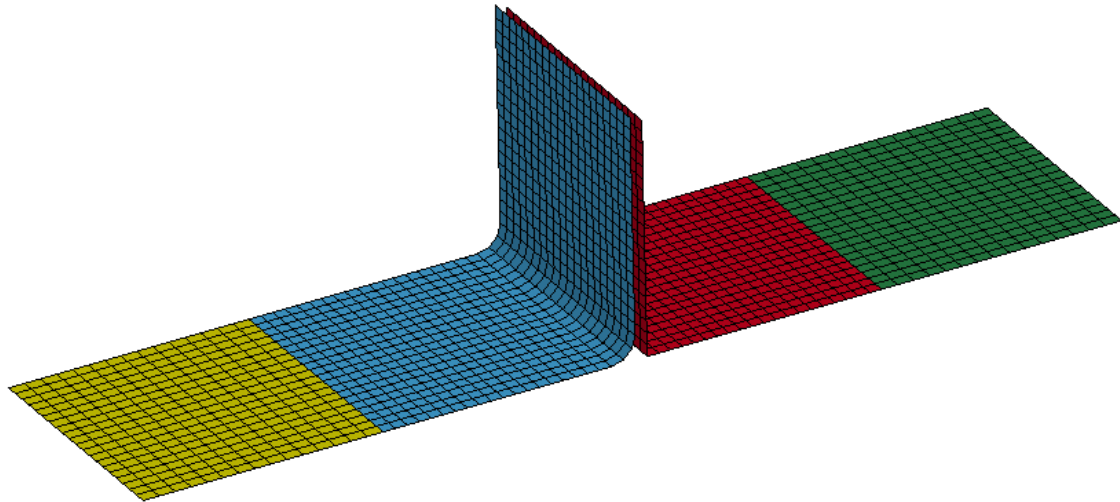
Figure 6.11: FE model of peeling specimen.

Because the rolled part of the specimen was bent during specimen machining, plastic strains occurred in the bent area. To account for this, plastic strains were obtained from a forming process simulation carried out by Sønstabø and Holmstrøm [19]. The obtained plastic strain and hardening parameter fields were mapped to the peeling model. The strains in the outermost integration point of the bend are shown in Fig. 6.12.
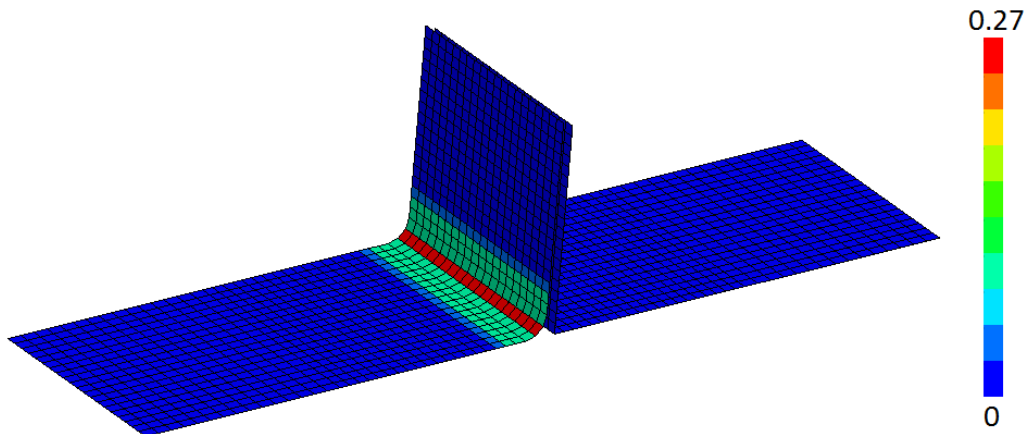
Figure 6.12: Mapped equivalent plastic strain field in the peeling specimen.

Results from the peeling simulations compared to the experiments are shown in Fig. 6.13. Both connector models showed good results during the first 15 mm of displacement. The spr2 model represented the experiments accurately up to 25 mm displacement, where premature failure occurred. The spotweld model without failure was capable of reaching

approximately the same force as the experiments, but the failure criterion was fulfilled too early. A reason for the early failure may have been the complex loading situation in the connector. As the test progressed, the plates was pressed together on one side of the connector, and torn apart on the other. This means that only one side of the connector transfered tensile forces in the connection. The elements at that side then failed prematurely because the force applied to each element exceeded the failure criteria.

As discussed earlier, the increased inclination of the force occurring in the experiments from about 22 mm to 25 mm displacement until failure was due to the screw tail hitting the bottom plate. This changed the physics of the deformation, and the effect was not captured in the simulations. It is not possible to determine if the failure would have been accurately predicted if the screw tail had not hit the plate.
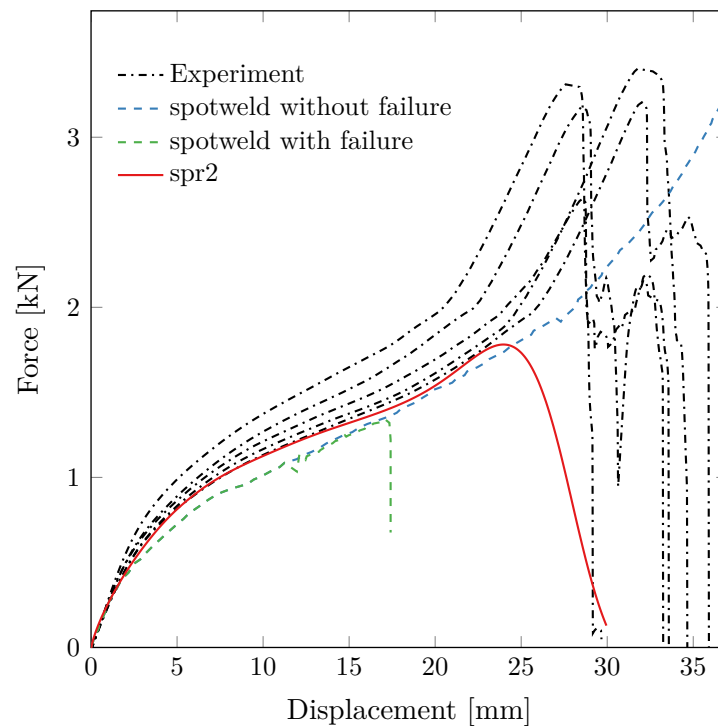
Figure 6.13: Simulation results from peeling tests.

Fig. 6.14 shows a comparison of an experimental specimen compared to the simulations after failure of the connection. Neither simulation has the same degree of deformation, although the spr2 model was a bit closer than the spotweld model. Both simulations show greater deformation in the top sheet than the experiment. This is because the simulations failed to represent the stiffening due to the screw-head.
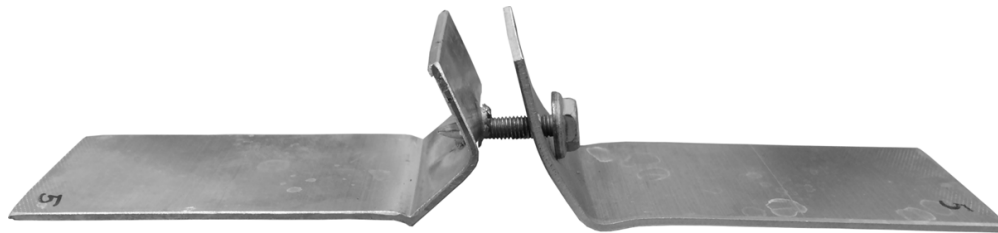
(a) Deformed peeling specimen after failure.
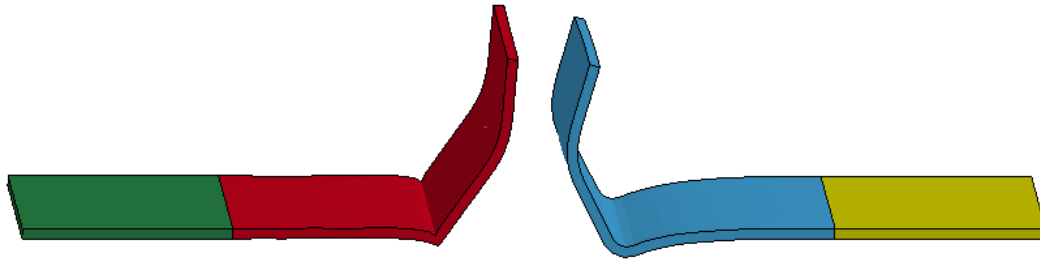
(b) Deformed peeling specimen after failure in the spr2 model validation.
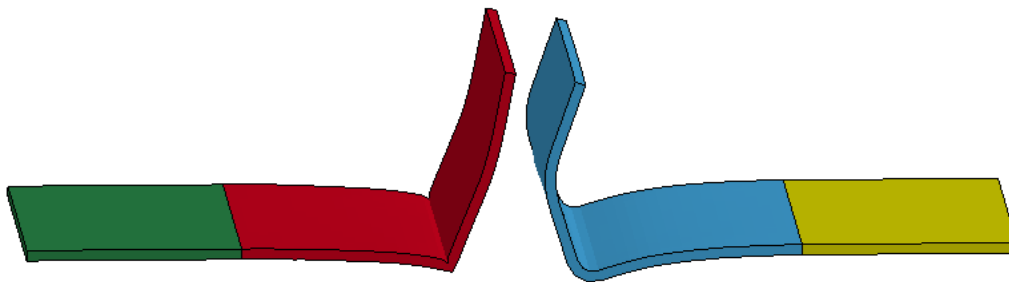
(c) Deformed peeling specimen after failure in the spotweld model validation.

Figure 6.14: Comparison between experiment and validation of the peeling specimen.

6.5.3 T-component

The FE model of the T-component is shown in Fig. 6.15. The specimen was modelled using the nominal measures shown in Fig. 3.13a. Transversal symmetry is used to model only half of the width, to reduce the number of elements needed in the simulation. The model consisted of 15802 3D shell elements with five through-thickness integration points. The rolled sheet profile on top consisted of 8950 deformable elements, and 800 rigid elements that simulated the top clamping of the specimen (the yellow part in Fig. 6.15). The extruded aluminium profile was represented by 5152 deformable elements, and 900 rigid elements simulating the bottom clamping of the component (the blue part in Fig. 6.15). All elements were $2\,\text{mm} \times 2\,\text{mm}$ in size. The rigid part of the extruded profile was fixed in all directions, while the rigid part of the rolled sheet material was given a velocity in

the longitudinal direction. A smooth curve was used to apply the velocity.
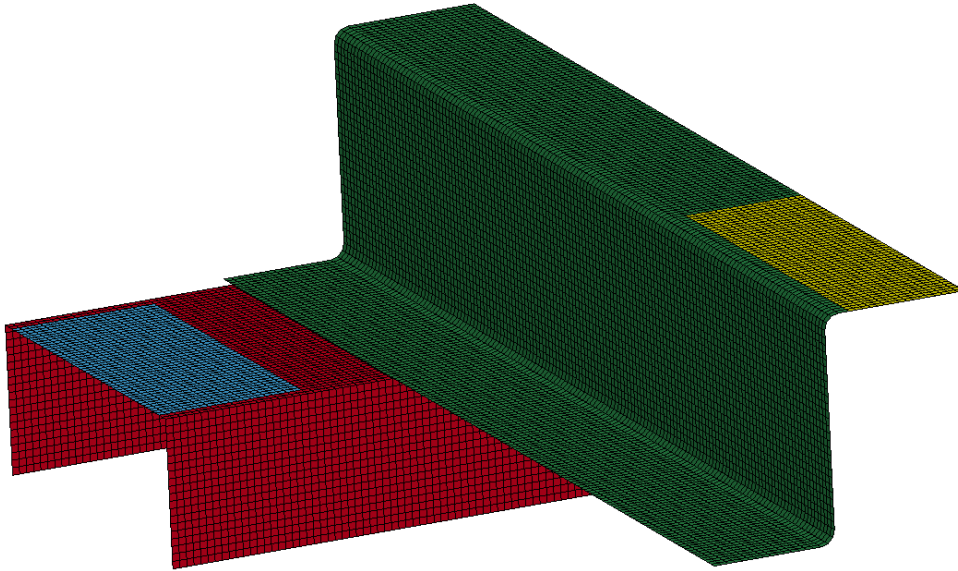
Figure 6.15: FE model of T-component.

As for the peeling specimen plastic strains in the bent sheet were extracted from a forming process analysis by Sønstabø and Holstrøm [19]. The equivalent plastic strain field prior to deformation is shown in Fig. 6.16.
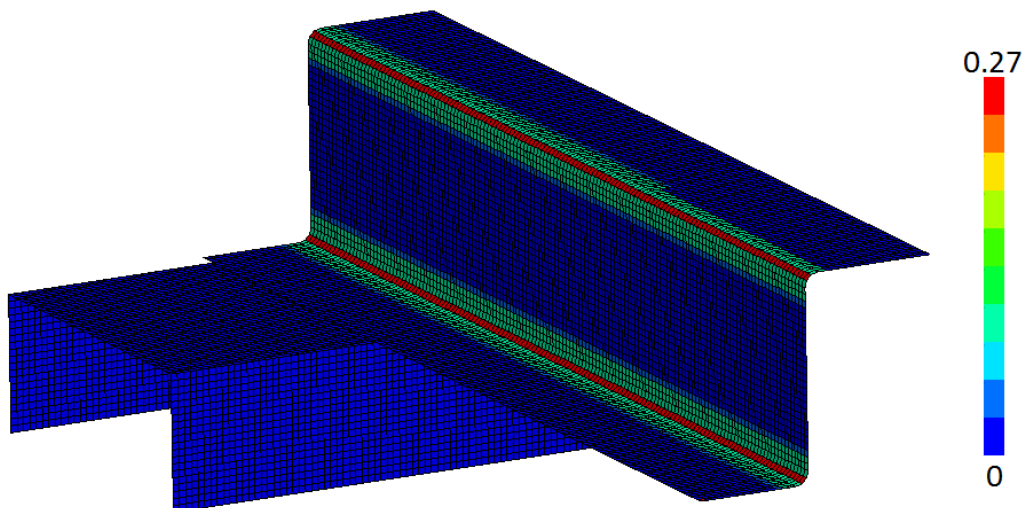
Figure 6.16: Mapped equivalent plastic strain field in the T-component specimen.

Results from the simulations of the T-component compared to the experimental results

are shown in Fig. 6.17. Relative displacement from the simulation was obtained from nodes with the same placement as in the DIC analysis, shown in Fig. 4.16a. The spr2 point-connector model showed too low stiffness. Maximum force was somewhat underestimated, while the relative displacement was better represented. The stiffness of the spotweld model was also lower than the results from the experiments, and the model failed too early. As for the lap-joint simulation, the connectors were rotated and failed due to a combination of tensile and shear forces. The T-component simulation confirms that a connector with a larger diameter should be used, to reduce the rotation of the connector. Interestingly, both macroscopic models showed similar behaviour until failure of the spotweld model, and both showed signs of too early yielding. The complex load situation seems to have caused some yielding in the connectors, which did not occur in the experiments.
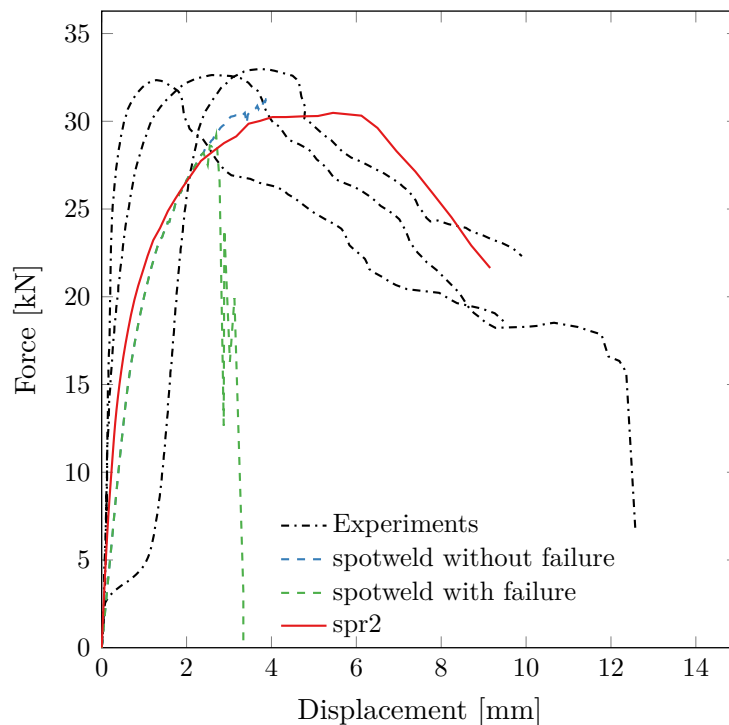
Figure 6.17: Simulation results from the T-component test.

Fig. 6.18 shows a comparison between the deformed T-component and the deformation from the simulations. As expected, a larger deformation was seen in the spr2 simulation than in the spotweld simulation as the spotweld failed too soon. Both simulations were able to represent the bending of the hat-profile due to the clamping in the top, but the spr2 simulation was closer to the experimental result.
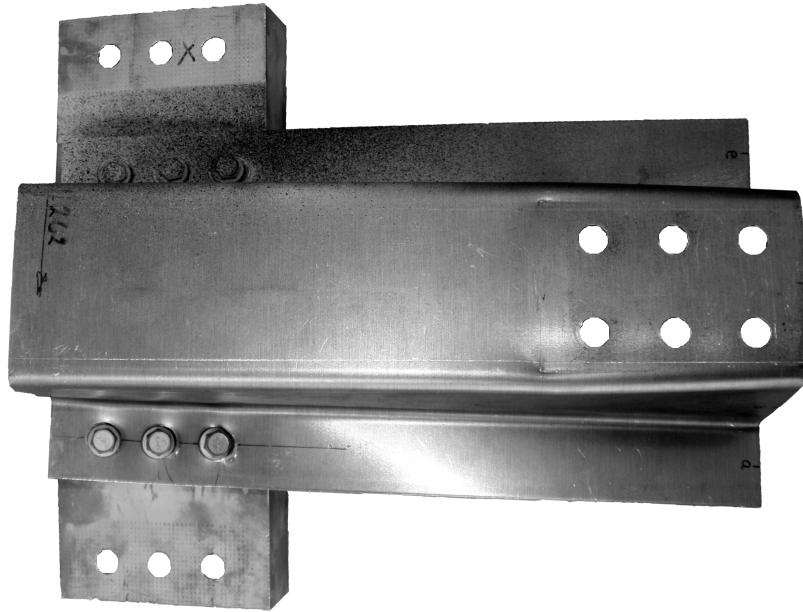
(a) Deformed T-component specimen after fracture.
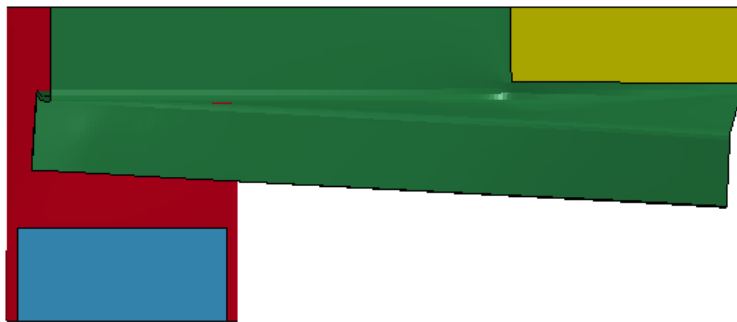
(b) Deformed T-component specimen after the spr2 model validation.
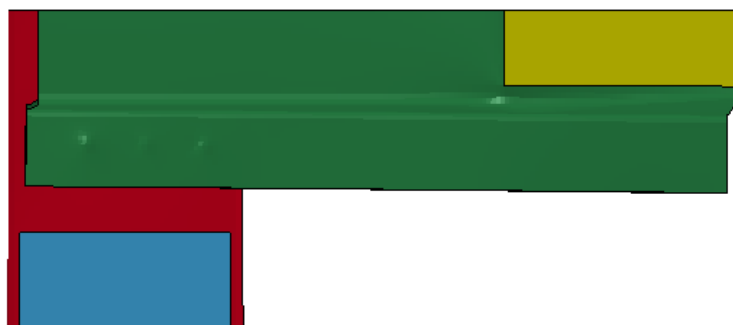
(c) Deformed T-component specimen after the spoteld model validation.

Figure 6.18: Comparison between experiment and validation of the T-component.

6.6   Concluding remarks

- A large-scale finite element model developed for self-piercing screws, the spr2 point-connector model, was calibrated for use with FDS using experimental results from the cross tests.

- A less investigated model consisting of solid elements tied between the sheets, the spotweld macroscopic model, was also calibrated using the same experimental results.

- A sensitivity analysis was conducted for the spotweld model. Changes in diameter and yield stress gave expected results for the spotweld macroscopic model. Smaller diameter and lower yield stress led to lower forces in the connection. For the lowest diameter and yield stress, yielding occurred in the connector itself rather than in the surrounding plates, resulting in a different global behaviour. Changes in Young's modulus and hardening factor did not reveal conclusive results. A new sensitivity analysis using other parameters as reference is proposed for future work.

- Optimisation of the spotweld model was done manually. Using optimisation software such as LS-OPT could identify model parameters that are closer to the experimental results.

- The optimised spr2 point-connector model was able to reproduce the cross test experimental results well. Validation using the lap-joint specimen showed accurate results, while peeling and the component tests were less accurate. In peeling the model represented the stiffness and deformation at failure well, but was not able to represent the maximum force observed in the experiments.

- The optimised spotweld macroscopic model was able to reproduce some parts of the experiments well, but needs further calibration. Validation of the model revealed too early failure for all tests.

- Because of the small diameter of the spotweld model, rotation may occurred too easily, thus increasing the normal force in the connector. This problem could be handled by using a larger diameter.

- For the peeling simulations it seems that having many elements in the spotweld connector leads to early failure in the connector. By using fewer and larger elements

in the connector, the stress in each element will be lower. This may lead to a better description of the failure of the connection.

Chapter 7

Three-layered point-connector model

As in Chapter 6, cross tests in tension and peeling tests were simulated using reduced integration and hourglass control number 4. Cross tests in shear and mixed loading and the lap-joint test were simulated using fully integrated shell elements and hourglass control number 8. No significant artificially introduced energy was observed in any simulation. Kinetic energy was compared to the internal energy, showing no significant kinetic energy in any simulation. The same contact formulation as for the two-layered models was applied between the plates to account for possible contact forces, with the friction coefficient set to 0.2.

7.1   Calibration of the three-layered spr2 model

The three-layered specimens were all modelled using the spr2 point-connector model. The purpose of this part was to investigate the possibility to develop reliable models for three-layered connections. Comparisons between the spr2 and the spotweld model was done with the two-layered specimen in Chapter 6, where it is shown that the spr2 model gave more accurate results. For this reason the spr2 model was chosen to model the three-layered specimen.

7.1.1   Cross type 2 and 3

The FE models are shown in Fig. 7.1. The specimens were modelled using the nominal geometry shown in Fig. 3.10 and the measured thickness. The model consisted of 3600 3D shell elements with five through-thickness integration points. For each plate 400 elements were part of deformable sections, while 800 rigid elements represented the rigid part of the test setup. All parts were modelled using $2\,\mathrm{mm} \times 2\,\mathrm{mm}$ elements. Simulations of the tests in 45 and 90 degree load direction were done by rotating the mesh used for the pure tension tests.

(a) Cross type 2.   **(b)** Cross type 3.
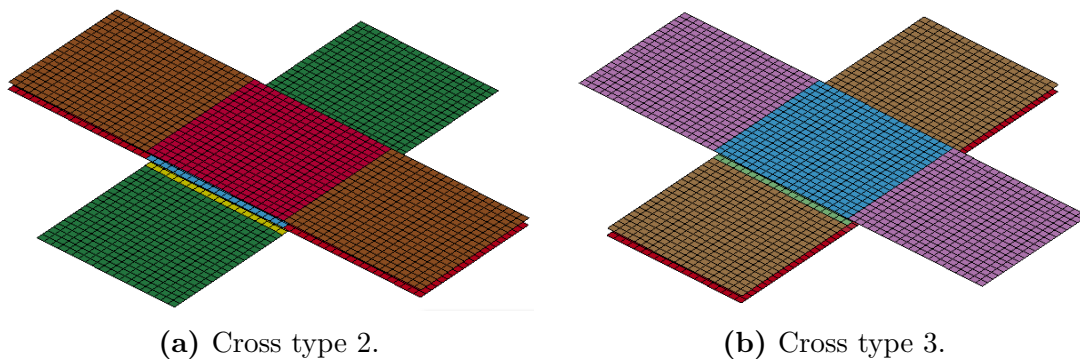
Figure 7.1: FE model of the three-layered cross specimens.

Calibration of the connector model was done using the same optimisation as for the two-layered spr2 model. One set of parameters was calibrated for the connection between the two top sheets, and one set was calibrated for the connection between the bottom plates. The results of the optimisation are presented in Table 7.1. The values in C12 are the parameters for the top part of the connection (near the screw head), calibrated from the cross type 2 tests. The values in C21 are the parameters for the bottom part of the connection, calibrated from the cross type 3 tests.

Table 7.1: Optimised parameters for spr2 point-connector model for three-layered connections.

Parameter	C12	C21	Unit	Description
f_n^{max}	2800	4000	N	Maximum pure normal force
f_t^{max}	7400	8000	N	Maximum pure shear force
δ_n^{fail}	3.2	3.2	mm	Deformation at failure for pure normal load
δ_t^{fail}	13	23	mm	Deformation at failure for pure shear load
ξ_n	0.82	0.82		Start of softening for pure normal deformation
ξ_t	0.6	0.7		Start of softening for pure shear deformation
$\alpha 1$	0.0766	0.3492		Initial value of the damage parameter α
$\alpha 2$	0.9735	0.8209		Value of α when softening starts
$\alpha 3$	814605	0.7027		Final value of α
d	12	12	mm	Diameter

Results of the calibration of the type 2 cross specimen are presented in Fig. 7.2. As seen from the results, acceptable accuracy was generally achieved for all type 2 cross simulations. From the results in tension presented in Fig. 7.2a it is evident that the connector model captured the maximum force and displacement in an acceptable manner, while it was not capable of capturing the two near linear parts of the deformation. For the shear loaded simulation results presented in Fig. 7.2b the maximum load and displacement were captured by the model. The initial stiffness was accurate. The mixed loading simulation shown in Fig. 7.2c slightly over-predicted the maximum load and displacement, but the result is considered acceptable.

(a) Tension.

(b) Shear.

(c) Mixed.
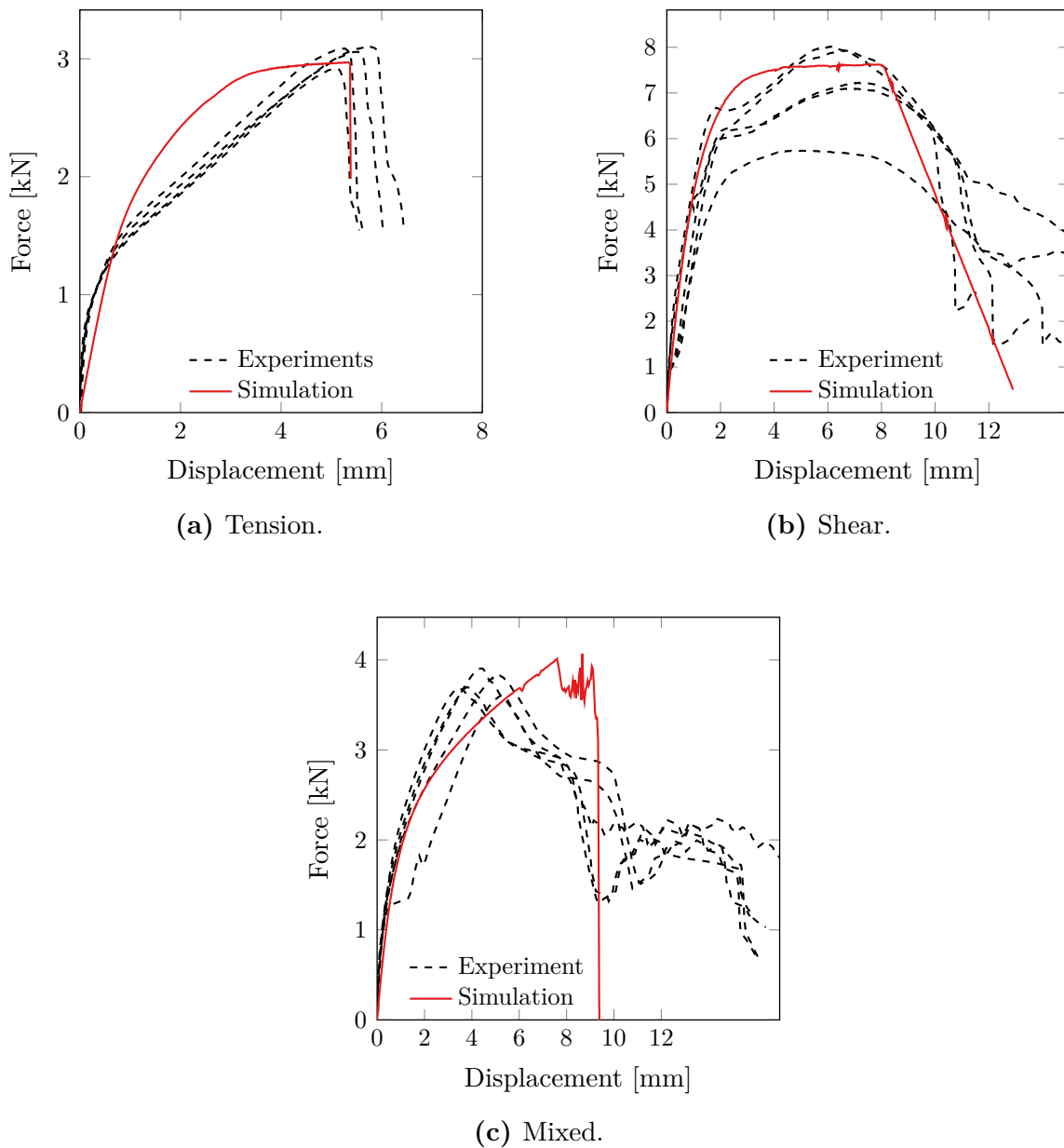
Figure 7.2: Simulation results from cross type 2 test.

Results from the simulations of the cross type 3 specimen are shown in Fig. 7.3. As for the type 2 simulation, acceptable results were achieved for all simulations. Tension and shear, presented in Fig. 7.3a and Fig. 7.3b, respectively, gave the best results, while the mixed loading simulation shown in Fig. 7.3c, again slightly over-predicted the maximum force and displacement.

The results from the pure tension loaded simulations were able to predict both maxi-

mum load and displacement with good accuracy. The simulation was close to predicting the two nearly linear parts of the curves. In shear the simulation was able to reproduce the initial stiffness and the failure well. The simulation did not show the drops in the force-displacement curve from the experiments. This indicates that the piecewise thread stripping was not reproduced. Mixed loading results under-estimated the initial stiffness and over-estimated the maximum load and displacement. The over-estimation of displacement was possibly a result of the under-estimation of the initial stiffness.

(a) Tension.

(b) Shear.

(c) Mixed.
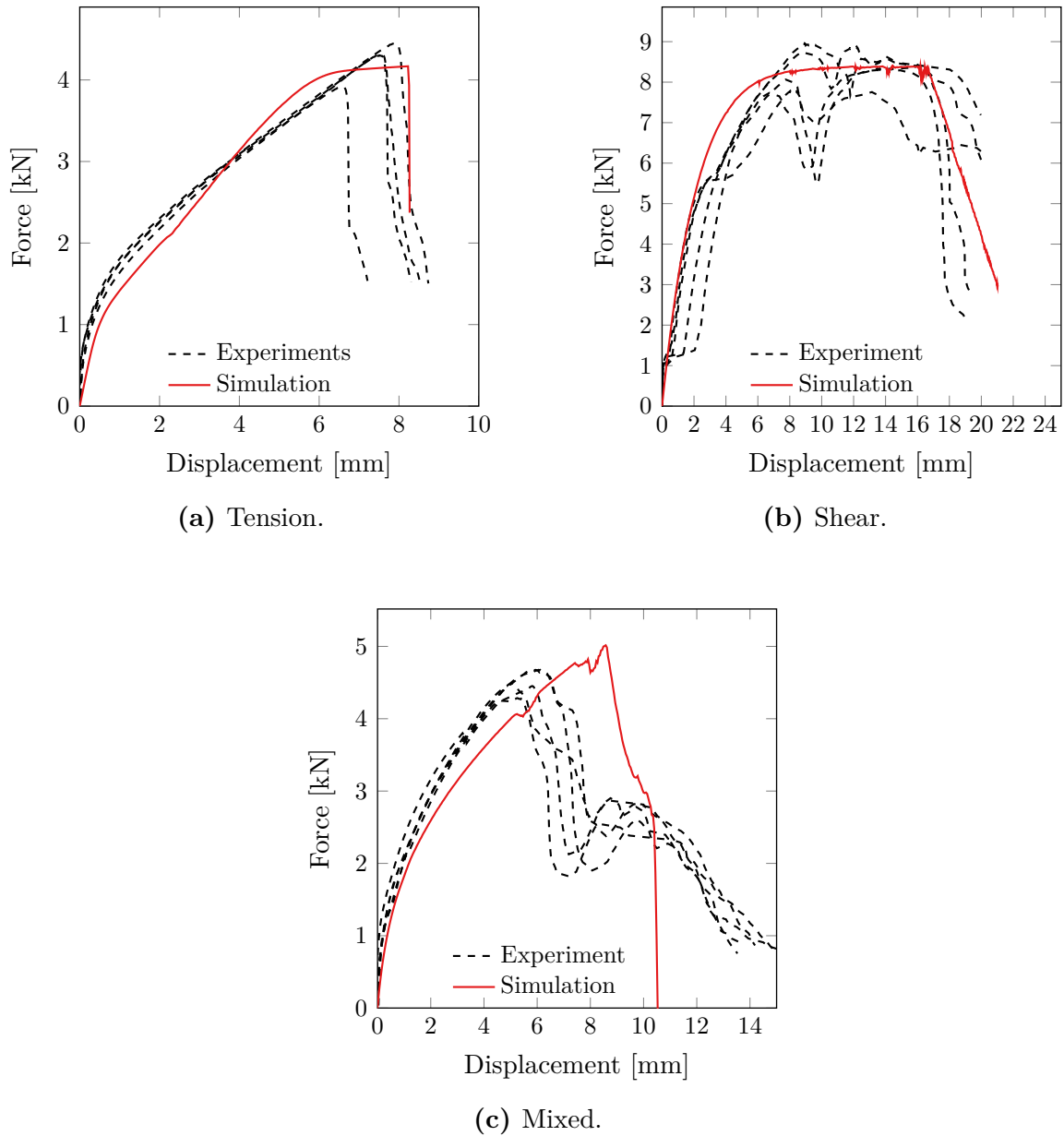
Figure 7.3: Simulation results from type 3 cross test.

7.2 Validation of the three-layered spr2 model

In this section the calibrated point-connector model for the three-layered connections is validated. Validation was done using the lap-joint and peeling tests.

7.2.1 Lap-joint

The FE model is shown in Fig. 7.4. The specimen was modelled using the nominal geometry shown in Fig. 3.11 and the measured thickness. The only difference from the two-layered simulation was the middle plate, with the properties of the rolled aluminium material. This was modelled using 1200 $2\,\mathrm{mm} \times 2\,\mathrm{mm}$ elements. As for the two-layered simulations, one of the ends was fixed in all directions, while the other was given a velocity in the longitudinal direction.
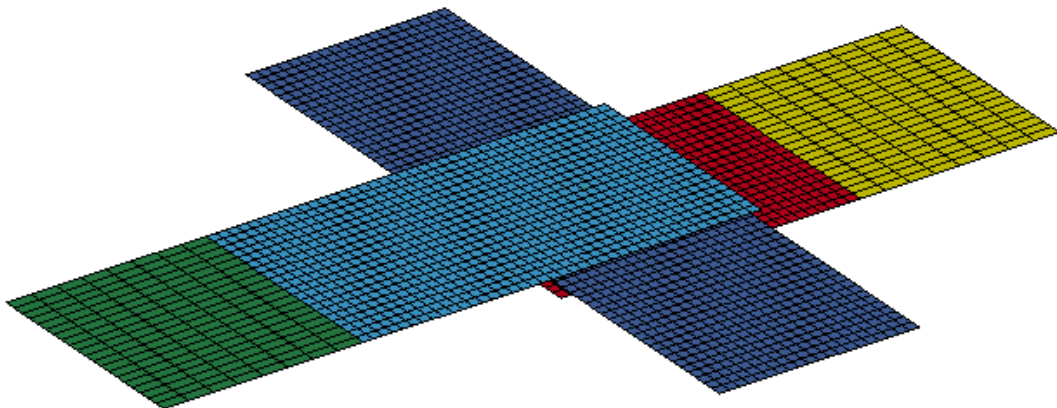
Figure 7.4: FE model of the three-layered lap-joint specimen.

Results from the three-layered lap-joint are presented in Fig. 7.5. As seen, the connector model over-predicted both the maximum load and the displacement at failure. This was probably because the model was not capable of predicting the fracture of the screw itself. The increased bending moment in the screw caused by the increased distance between the head of the screw and the threads in the bottom sheet was not captured by the model. In the simulations the failure occurred in the bottom connector, while the experiments experienced screw fracture. As expected, the model was not able to capture the slipping observed in the experiments. The slipping is difficult to predict without modelling the pre-drilled holes and the screw itself.
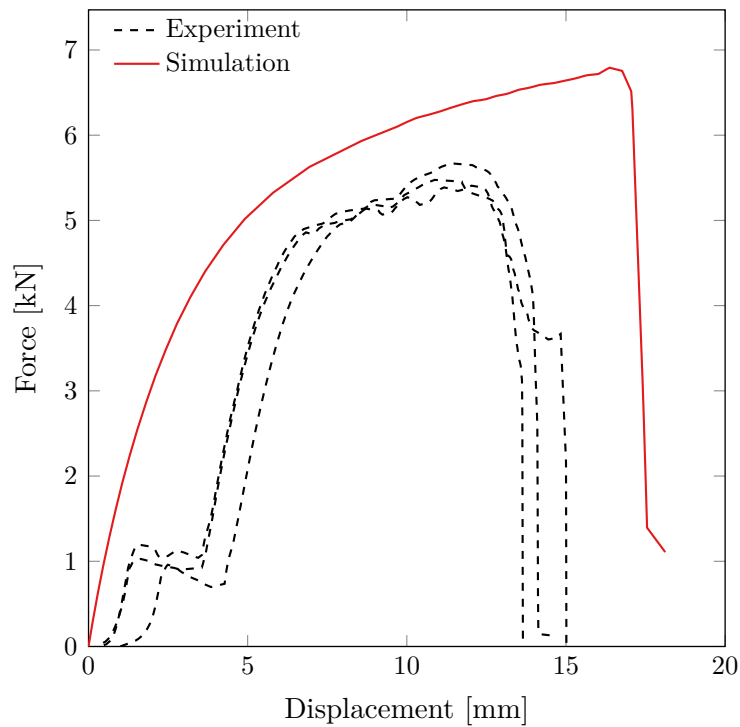
Figure 7.5: Simulation results from the three-layered lap-joint tests.

In Fig. 7.6 a comparison between a deformed specimen from simulation and experiments is presented. As seen, the deformation of the plates was not as prominent in the simulation as in the experiment. This is due to the length of the screw, and area of the screw head that stiffen the connection. It can also be seen that the experimental test failed in fracture in the top of the screw, while the bottom connector failed in the simulation.

(a) Deformed three-layered lap-joint specimen after fracture.
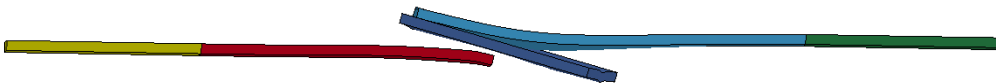
(b) Deformed three-layered lap-joint specimen after the spr2 model validation.

Figure 7.6: Comparison between experiment and validation of the lap-joint specimen.

7.2.2   Peeling

The FE model is shown in Fig. 7.7. The specimen was modelled using the the nominal geometry shown in Fig. 3.12 and the measured thickness. The model was the same as for the two-layered simulation, with an extra deformable plate between the original parts. The middle plate was modelled using 1200 $2\,\mathrm{mm} \times 2\,\mathrm{mm}$ elements, with the properties of the rolled aluminium material. As for the two-layered simulations, one of the ends was fixed in all directions, while the other was given a velocity in the longitudinal direction.

As for the two-layered peeling specimen, the rolled sheet part of the specimen was bent, and plastic strains were applied to the model. As the bent parts were equal for the two- and three-layered specimens, the mapped plastic strains from the two-layered simulation were used, showed in Fig. 6.12.
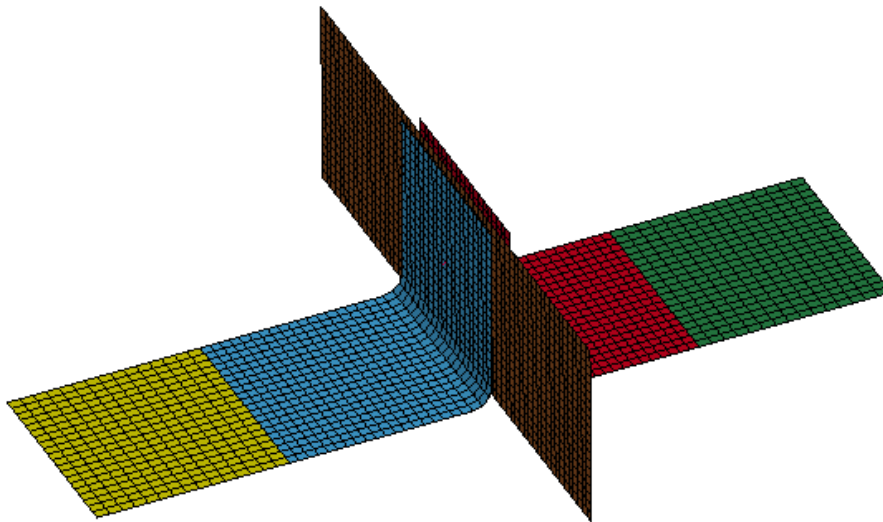
Figure 7.7: FE model of the three-layered peeling specimen.

Fig. 7.8 shows the results from the three-layered peeling simulations compared to the experiments. The simulation slightly under-predicted the force the first 20 mm of deformation. The peak caused by high rotation of the screw described in Chapter 4 was not reproduced. This was similar to the results from the two-layered peeling simulation, and is difficult to capture without modelling the entire screw itself. The displacement at failure was accurately described by the simulation.

In Fig. 7.9 a visual comparison between the experiment and the simulation is shown. As for the two-layered test, the deformation of the top sheet was too large in the simulation.

This is because of the large diameter of the screw-head, which the simulation did not represent correctly. From the visualisation of the simulation, it is obvious that the top connector failed. As the connectors should experience similar forces, it was expected that the top connector would fail first as it had the lowest capacity, shown in Table 7.1.
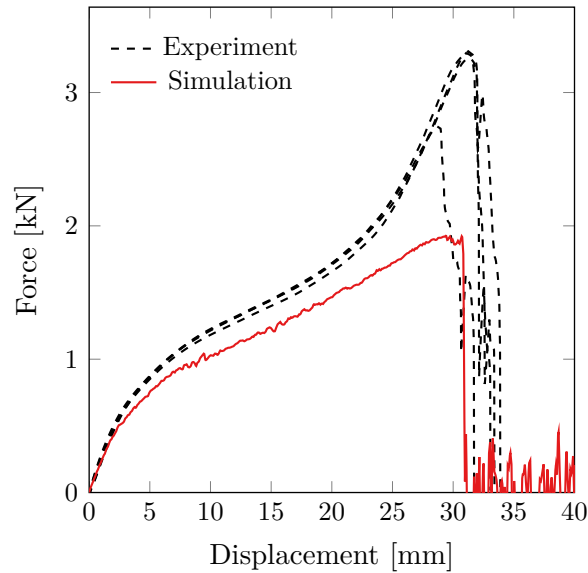
Figure 7.8: Simulation results from three-layered peeling tests.

(a) Deformed three-layered peeling specimen after fracture.
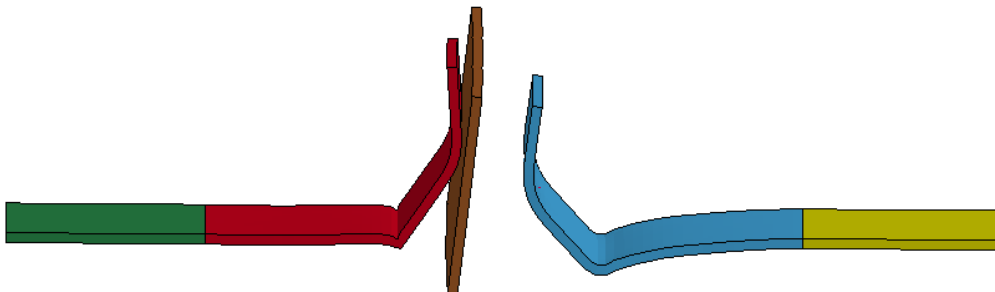
(b) Deformed three-layered peeling specimen using the spr2 model.

Figure 7.9: Comparison between experiment and simulation of the peeling specimen.

7.3 Concluding remarks

- The spr2 model was calibrated for use with three-layered FDS-connections using experimental results. Two calibrations were done, one between the top and middle plates (cross type 3) and one between the middle and bottom plates (cross type 2). One set of parameters was obtained for each calibration.

- The parameters of the optimisation fits the experimental results well, especially in tension and shear. For mixed loading the force is somewhat over-estimated.

- Numerical models of the three-layered peeling and lap-joint connections were made and analysed to validate the calibrated spr2 connector model.

- The three-layered peeling results under-predicted the force and the initial stiffness, but predicted the displacement accurately. The connector model was not able to reproduce the final stiffness peak in the peeling tests caused by the screw tail hitting the bottom plate.

- The stiffness of the three-layered lap-joint was similar to the experiments, but the forces and failure deformation was over-predicted. A way to capture the increased moment introduced by the extra sheet in shear should be investigated in future work.

Chapter 8

Conclusion

In this study the experimental behaviour of Flow-Drilling Screw (FDS) connections has been studied. Two- and three-layered connections joining one or two sheets to an extrusion have been investigated. An extensive experimental program has been carried out challenging the connections under various quasi-static loading conditions. The global force-displacement responses and the fracture behaviour have been closely investigated. Two relatively sophisticated macroscopic models have been assessed with respect to their ability to describe the behaviour of the FDS connection.

The Barlat 18 parameter anisotropic yield surface, together with the Voce hardening rule, was used to model the plate materials. The constitutive model for the extrusion was calibrated and validated with respect to material tests, while the model for the sheet was adopted from previous work. Uniaxial tension tests in seven material directions, plane strain tension and in-plane single shear tests were performed on the extruded aluminium alloy 6063 in T6 condition. Generally, high repeatability and little scatter was observed in all tests. In the uniaxial tension tests some anisotropy in flow stresses and plastic flow was observed.

Uniaxial tension tests of the screw material used in the experiments were performed. A yield strength of 1105 MPa was measured, and little hardening and high ductility were observed.

Three different cross test types in three different loading configurations, as well as lap-joint and peeling tests with both two and three layers were carried out. Generally little scatter was observed in the tests, and the repeatability was acceptable. Shear dominated loading

situations generally experienced higher forces than tensile dominated loading. In two-layered cross tests, the pure shear loaded specimens experienced twice as high forces as the tensile loaded. The tensile dominated specimens generally failed in thread stripping. Cross type 2 in pure shear and three-layered lap-joint failed due to fracture of the screw itself between the top and middle plate. Type 3 cross tests in pure shear failed due to end tear-out in the material of the top layer. Generally comparing results from two- and three-layered tests the same trends are discernable. The type 3 cross tests showed the highest forces of all cross tests in all loading configurations. Very similar results were registered for two- and three-layered lap-joint and peeling tests. Relative sliding between the top and bottom layer was observed for both pure shear loaded and mixed loaded tests due to the pre-drilling of the top sheet.

A component with six screw connections was tested. The component consisted of a hat-profile joined to an extruded U-beam using three screws on each flange. Little scatter was observed, and the repeatability was acceptable. All screws in the connections experienced both rotation and one-sided thread stripping. Failure occurred to the bottom screw first, and the two others failed shortly after. Only the screws on one side failed in each test. Failure of the test rig occurred in two of the tests. The tests showed no sign of plastic deformation, and were repeated with good results. More component tests should be conducted to validate the tests done in this thesis

The chosen material calibration was validated using uniaxial tension, plane strain tension and in-plane single shear experiments and simulations. Uniaxial tension and plane strain tension simulations showed satisfying results, while forces were over-estimated for the in-plane single shear test. This indicates that the yield surface was close to correct in the plane strain dominated domain, but less accurate in the shear dominated domain.

Two macroscopic models for large-scale finite element simulations were calibrated to the FDS cross results. Firstly, the spr2 point-connector model originally developed for self-piercing rivet connections was calibrated. The optimised model was able to reproduce the cross test experimental results well. Validation using the lap-joint specimen showed accurate results, while peeling and the component tests were less accurate. In peeling the model represented the stiffness and deformation at failure well, but was not able to represent the maximum force observed in the experiments. The validation of the component test represented the maximum force and deformation at failure well, but the simulation showed signs of yielding earlier than the experiments.

Secondly, a spotweld model consisting of solid elements with a specially designed material model tied between the sheets was calibrated. A sensitivity analysis was conducted for the model. The analysis revealed that smaller diameter and lower yield stress led to lower forces in the connection. Varying Young's modulus and hardening factor did not reveal conclusive results. Validation of the model revealed too early failure for all tests. The diameter used in the model was relatively small. This may have caused the connection to be too soft, enabling for rotation and thus increasing the normal force in the connector.

The spr2 model was calibrated for use with three-layered FDS-connections using experimental results. One set of parameters was obtained for the connection between the top and middle plates, and one set for the middle and bottom plates. The parameters of the optimisation fit the experimental results well, especially in tension and shear. For mixed loading the force was somewhat over-estimated. Validation of the spr2 model was done, using three-layered peeling and lap-joint tests. Results from three-layered peeling under-predicted the force and the initial stiffness, but predicted the displacement accurately. The stiffness of the three-layered lap-joint was similar to the experiments, but the forces and failure deformation was over-predicted.

This thesis has documented the behaviour of two- and three-layered connections previously not described. Finite element models of the connections have been optimised and validated. Some considerations regarding future work follows. The spr2 model for three-layered connections should be further investigated and optimised, especially for shear loaded conditions. Parameters of the spotweld model should be investigated further. An optimisation of the model using software such as LS-OPT is adviced to identify connector parameters that are closer to the experimental results.

Appendix A

Experimental setup

A.1 Material tests

The tests were conducted in accordance with ISO-standards.

For the uniaxial tension tests, the pre strained tension test and the in-plane single shear tests, a Zwick/Roell Z030 universal test machine with a 30 kN load cell was used. A MTS 634.31F-25 exstensometer was used, with varying gauge lengths depending on the test type. A HBM Scout 55 amplifier was used with a NI USB-6356 logging system.

For the disc compression tests, a Instron 8032 test machine was used with a 100 kN load cell. Logging was done using Instron's own software, Bluehill 2.

The uniaxial screw tests were conducted using a Dartec M 1000 RK universal test machine with a 20 kN load cell. Test 01 was first conducted in an Instron 5954 test machine with a 2 kN load cell, but at a loading of 2 kN, the specimen showed no signs of yielding.

Force, crosshead displacement and extensometer opening was logged at a frequency of 10 Hz for all tests and both test setups. All thickness measurements were taken using the same instrument, a Micromar 40 EW. Longer measurements, such as heights and widths, were taken using a Mahr IP67 caliper. The instruments were set to 0 before each set of measurements, and tightened with the same force for each measure.

A.2 Single connector tests

For the lap-joint and peeling tests, a Zwick/Roell Z030 universal test machine with a 30 kN load cell was used. A HBM Scout 55 amplifier was used with a NI USB-6356 logging system. An Instron 8550 biaxial test machine with a 100 kN loading cell was used for the three different cross tests. A Fluke NetDaq logging system was used to log load force and cross head displacement.

A.3 Component tests

An Instron 5982 test machine with a 100 kN load cell was used together with the Bluehill 3 logging system, that logged load force and cross head displacement.

Appendix B

Measurements

B.1 Material tests

Table B.1: Measurements of the uniaxial tension tests, results in mm.

Specimen nr.		Width 1	2	3	Thickness 1	2	3
UT6063_00_01	*Pre*	4.953	4.950	4.958	1.895	1.891	1.892
	Post	4.85	4.836	4.848	1.817	1.802	1.817
UT6063_00_02	*Pre*	4.945	4.949	4.960	1.890	1.891	1.888
	Post	4.857		4.88	1.814		1.837
UT6063_00_03	*Pre*	4.953	4.949	4.949	1.891	1.893	1.891
	Post		4.845	4.884		1.814	1.811
UT6063_15_01	*Pre*	4.957	4.957	4.967	1.898	1.900	1.906
	Post	4.854	4.806	4.912	1.816	1.774	1.83
UT6063_15_02	*Pre*	4.957	4.960	4.960	1.903	1.901	1.895
	Post	4.876	4.863		1.81	1.783	
UT6063_15_03	*Pre*	4.986	4.959	4.955	1.939	1.903	1.899
	Post		4.855	4.868		1.78	1.803
UT6063_30_01	*Pre*	4.946	4.944	4.952	1.893	1.903	1.888
	Post	4.89	4.87		1.824	1.8	
UT6063_30_02	*Pre*	4.950	4.963	4.954	1.902	1.913	1.905
	Post	4.878		4.895	1.808		1.826
UT6063_30_03	*Pre*	4.962	4.947	4.949	1.903	1.897	1.892
	Post		4.869	4.889		1.796	1.807
UT6063_45_01	*Pre*	4.947	4.941	4.941	1.893	1.895	1.889
	Post	4.858		4.873	1.811		1.822
UT6063_45_02	*Pre*	4.955	4.950	4.952	1.909	1.904	1.898
	Post		4.862	4.882		1.824	1.828
UT6063_45_03	*Pre*	4.953	4.951	4.952	1.894	1.893	1.889
	Post		4.888	4.895		1.837	1.84
UT6063_60_01	*Pre*	4.951	4.951	4.955	1.889	1.894	1.900
	Post		4.835	4.92		1.827	1.843
UT6063_60_02	*Pre*	4.950	4.950	4.951	1.889	1.891	1.890
	Post	4.737	4.812	4.858	1.799	1.818	1.842
UT6063_60_03	*Pre*	4.943	4.940	4.958	1.892	1.891	1.890
	Post		4.843	4.895		1.836	1.868
UT6063_75_01	*Pre*	4.936	4.926	4.928	1.897	1.895	1.893
	Post		4.78	4.828		1.85	1.86
UT6063_75_02	*Pre*	4.958	4.959	4.959	1.900	1.901	1.897
	Post		4.808	4.898		1.854	
UT6063_75_03	*Pre*	4.911	4.913	4.915	1.893	1.890	1.892
	Post		4.744	4.792		1.843	1.857
UT6063_90_01	*Pre*	4.924	4.920	4.931	1.894	1.896	1.896
	Post	4.79			1.862		
UT6063_90_02	*Pre*	4.912	4.914	4.919	1.914	1.912	1.907
	Post		4.737	4.812		1.881	1.89
UT6063_90_03	*Pre*	4.915	4.915	4.917	1.896	1.897	1.895
	Post	4.696		4.823	1.856		1.884

Table B.2: Measurements of the plane strain tension tests, results in mm.

Specimen nr.	Minimum width of test area	Thickness
PST6063_00_01	17.29	1.889
PST6063_00_02	17.30	1.889
PST6063_00_03	17.30	1.888

Table B.3: Measurements of the in-plane single shear tests, results in mm.

Specimen	Minimum height of test area	Thickness
ISS6063_00_01	2.5	1.935
ISS6063_00_02	2.5	1.927
ISS6063_00_03	2.5	1.901

Table B.4: Measurements of the disc compression tests, results in mm.

Specimen nr.		D_0	D_{90}	D_{45}	D_{135}	t
DISC6063_00_01	Pre	14.09	14.02	14.05	14.03	1.872
	Post	17.19	15.48			1.425
DISC6063_00_02	Pre	14.12	14.03	14.02	14.04	1.877
	Post	17.33	15.42			1.410
DISC6063_00_03	Pre	14.13	14.06	14.05	14.04	1.883
	Post	17.36	15.46			1.435
DISC6063_00_04	Pre	14.12	14.05	14.05	14.05	1.882
	Post	17.27	15.51			1.425
DISC6063_00_05	Pre	14.13	14.03	14.03	14.02	1.886
	Post	17.55	15.45			1.404
DISC6063_00_06	Pre	14.14	14.05	14.05	14.06	1.874
	Post	17.64	15.44			1.405

Table B.5: Measurements of the UT screw specimen tests, results in mm.

Specimen nr.	Diameter
1	2.028
2	2.026
3	2.034
4	2.025
5	2.025
6	2.015
7	2.039
8	2.017
9	2.030
10	2.027

B.2 Single connector tests

Table B.6: Measurements of the C specimens in mm.

Specimen nr.	l_{top}	w_{top}	t_{top}	l_{bottom}	w_{bottom}	t_{bottom}	$m1$	$m2$
C11_00_01	120.10	40.22	1.989	120.55	39.95	1.940	20.11	60.22
C11_00_02	120.00	39.96	1.988	120.68	40.09	1.995	20.06	60.02
C11_00_03	120.07	40.12	1.990	120.57	40.09	1.977	20.17	60.13
C11_00_04	120.17	39.98	1.993	119.54	40.04	1.998	20.22	60.21
C11_45_01	120.13	40.03	2.000	120.49	40.06	1.956	20.2	59.90
C11_45_02	120.04	40.06	1.986	120.02	40.11	1.943	20.04	59.96
C11_45_03	120.18	40.28	1.989	120.67	40.14	1.976	20.37	60.07
C11_45_04	120.01	40.21	1.985	120.73	39.86	1.983	20.14	60.09
C11_45_05	120.12	39.87	2.000	120.68	39.95	1.977	20.17	60.16
C11_90_01	120.09	40.01	1.995	120.55	40.13	1.994	20.28	60.10
C11_90_02	120.05	39.97	1.995	120.44	39.92	1.977	20.07	60.03
C11_90_03	120.04	40.23	1.988	120.57	39.89	1.941	19.70	59.85
C11_90_04	119.99	40.27	1.998	120.36	40.00	1.938	20.05	59.83
C11_90_05	120.16	40.01	1.994	120.52	39.99	1.984	20.16	60.14
C11_90_06	120.01	39.44	1.987	120.53	40.09	1.988	20.35	60.25
Average	120.08	40.04	1.992	120.46	40.02	1.971	20.14	60.06

Table B.7: Measurements of the LJ specimens in mm.

Specimen nr.	l_{tot}	l_{top}	w_{top}	t_{top}	l_{bottom}	w_{bottom}	t_{bottom}	$m1$	$m2$
SLJ_00_01	181	120.32	38.34	1.986	100.20	39.78	1.972	20.14	19.85
SLJ_00_02	181	120.12	40.06	1.985	100.05	40.04	1.981	20.18	20.48
SLJ_00_03	181	120.06	40.08	1.992	100.02	39.90	1.978	20.34	20.08
SLJ_00_04	181	119.90	40.13	1.994	100.04	39.89	1.981	20.36	19.63
SLJ_00_05	181	120.10	40.22	1.989	99.87	40.12	1.969	20.47	19.90
Average	181	120.10	39.77	1.989	100.04	39.95	1.976	20.30	19.99

Table B.8: Measurements of the P specimens in mm.

Specimen nr.	l_{tot}	l_{top}	w_{top}	t_{top}	l_{bottom}	w_{bottom}	t_{bottom}	t_{tot}	$m1$	$m2$
P_90_00_01	164	83.54	40.19	1.987	80.53	40.32	1.872	3.899	19.71	20.07
P_90_00_02	163	83.55	40.10	1.995	79.59	40.31	1.878	3.899	19.99	20.24
P_90_00_03	163	83.29	40.24	1.994	79.30	40.28	1.875	3.915	19.91	19.89
P_90_00_04	163	83.48	40.18	2.005	79.90	40.41	1.879	3.895	19.24	20.09
P_90_00_05	163	83.20	40.26	2.005	79.82	40.15	1.879	3.941	20.04	21.22
Average	163	83.41	40.19	1.997	79.83	40.29	1.877	3.910	19.78	20.30

Table B.9: Measurements of the C21 specimens in mm.

Specimen nr.	l_{top1}	w_{top1}	l_{top2}	w_{top2}	t_{toptot}	l_{bottom}	w_{bottom}	t_{bottom}	$m2$	$m1$
C21__00__01	120.13	40.06	120.32	40.11	4.015	120.60	40.09	1.936	59.99	19.96
C21__00__02	120.30	40.09	120.16	40.01	4.006	120.57	39.89	1.940	60.11	19.27
C21__00__03	120.07	39.77	120.24	40.46	4.017	120.77	40.09	2.000	60.11	20.24
C21__00__04	119.96	40.09	120.17	40.07	4.021	120.41	40.17	1.975	59.99	20.26
C21__00__05	120.16	40.07	120.54	40.06	4.096	120.44	40.10	1.984	60.32	20.35
C21__45__01	120.39	40.08	120.19	40.08	4.044	120.62	39.84	1.991	60.49	20.17
C21__45__02	120.03	40.16	120.16	40.07	4.060	120.41	40.09	1.981	60.41	19.92
C21__45__03	120.41	40.06	120.19	40.06	4.167	120.54	40.13	1.995	59.97	20.13
C21__45__04	120.39	40.06	120.32	40.06	4.112	120.71	40.05	1.985	59.98	20.25
C21__45__05	120.12	40.26	120.26	40.00	4.000	120.73	39.90	1.986	60.41	20.09
C21__90__01	120.13	40.12	120.32	40.14	3.988	120.51	39.99	1.955	60.40	20.10
C21__90__02	120.10	40.02	120.22	40.09	4.049	120.42	40.09	1.955	60.34	20.29
C21__90__03	120.12	40.06	120.41	40.08	4.031	120.31	40.11	1.970	59.97	19.06
C21__90__04	120.33	40.06	120.12	40.04	4.023	120.72	40.06	1.975	60.48	20.20
C21__90__05	120.00	40.07	120.37	40.07	4.049	120.56	40.07	1.940	60.08	20.14
Average	120.18	40.07	120.27	40.09	4.045	120.55	40.04	1.971	60.20	20.03

Table B.10: Measurements of the C12 specimens in mm.

Specimen nr.	l_{top}	w_{top}	t_{top}	$l_{bottom1}$	$w_{bottom1}$	$l_{bottom2}$	$w_{bottom1}$	$t_{bottomtot}$	$m2$	$m2$
C12__00__01	119.97	39.98	2.011	119.83	39.99	119.99	40.02	3.998	59.30	19.62
C12__00__02	120.09	40.02	1.996	119.93	40.19	120.60	40.06	3.962	59.96	19.99
C12__00__03	120.02	40.07	1.990	120.15	40.13	120.52	40.07	4.014	60.12	20.06
C12__00__04	120.18	39.95	1.991	120.00	40.11	119.81	40.00	4.022	59.96	19.85
C12__00__05	120.06	39.99	1.992	120.17	40.33	120.50	40.03	4.045	59.87	20.06
C12__45__01	119.96	40.00	2.000	120.12	40.20	120.36	40.13	4.015	59.83	19.86
C12__45__02	120.20	40.03	1.988	120.14	40.17	120.65	40.12	4.030	60.15	19.96
C12__45__03	120.21	39.97	1.991	120.39	39.96	120.50	40.04	4.042	60.40	19.97
C12__45__04	119.97	40.08	1.998	120.04	40.22	119.93	40.06	3.970	59.86	20.22
C12__45__05	119.94	40.06	1.991	120.12	40.01	120.45	40.05	3.987	60.15	19.80
C12__90__01	120.10	39.99	1.998	120.09	40.00	120.46	40.07	4.052	60.24	20.27
C12__90__02	120.06	40.00	1.991	120.15	39.94	120.59	40.10	4.055	60.19	20.12
C12__90__03	120.06	39.95	1.993	120.15	40.16	120.32	40.08	3.970	59.92	19.95
C12__90__04	120.07	40.00	1.985	119.85	39.97	119.80	39.82	4.218	60.07	20.13
C12__90__05	120.05	39.90	1.989	120.21	40.07	120.66	40.00	4.051	59.95	20.24
C12__90__06	120.04	39.96	1.991	120.16	40.19	120.57	40.07	3.966	59.82	20.22
Average	120.06	40.00	1.993	120.09	40.10	120.36	40.05	4.025	59.99	20.02

Table B.11: Measurements of the 3LJ specimens in mm.

Specimen nr.	l_{tot}	l_{top}	w_{top}	l_{mid}	w_{mid}	l_{bottom}	w_{bottom}	t_{top}	t_{mid}	t_{bottom}	$m1$	$m2$
3SLJ__01	183	120.13	40.31	120.47	40.08	99.97	39.82	1.988	1.988	1.981	20.13	20.30
3SLJ__02	183	120.20	40.23	120.09	39.98	99.96	40.01	1.992	1.998	1.981	19.99	21.00
3SLJ__03	181	120.16	40.32	120.38	40.05	100.17	40.14	1.991	1.990	1.973	19.69	21.02
Average	182	120.16	40.29	120.31	40.04	100.03	39.99	1.990	1.992	1.978	19.94	20.77

Table B.12: Measurements of the 3P specimens in mm.

Specimen nr.	l_{tot}	l_{top}	w_{top}	l_{mid}	w_{mid}	l_{bottom}	w_{bottom}	t_{top}	t_{mid}	t_{bottom}	$m1$	$m2$
3_P__01	165	83.58	40.29	119.90	40.28	80.37	40.13	1.999	1.997	1.87	19.35	19.63
3_P__02	165	83.24	40.11	119.94	40.06	79.74	39.80	1.996	1.989	1.874	20.40	20.15
3_P__03	166	83.89	40.00	120.00	40.22	80.48	40.18	1.998	1.995	1.876	19.89	20.08
3_P__04	165	83.54	40.11	120.05	40.19	79.99	39.69	2.001	1.999	1.873	20.20	19.91
Average	165	83.56	40.13	119.97	40.19	80.15	39.95	1.999	1.995	1.873	19.96	19.94

B.3 Component tests

Table B.13: Main measurements of the T-component specimens in mm.

Specimen nr.	$length_{hat}$	$width_{hat}$	$height_{hat}$	t_{hat}	$length_U$	$width_U$	$height_U$	t_U
T_01	299	151.38	62.29	1.991	267	100.1	40.02	1.888
T_02	299	151.78	62.60	1.993	266	99.9	39.99	1.889
T_03	300	149.67	62.36	1.994	269	99.9	40.00	1.891
Average	299	150.94	62.41	1.993	267	100.0	40.00	1.890

Table B.14: Measured screw placement in the T-component specimens in mm, see Fig. B.1.

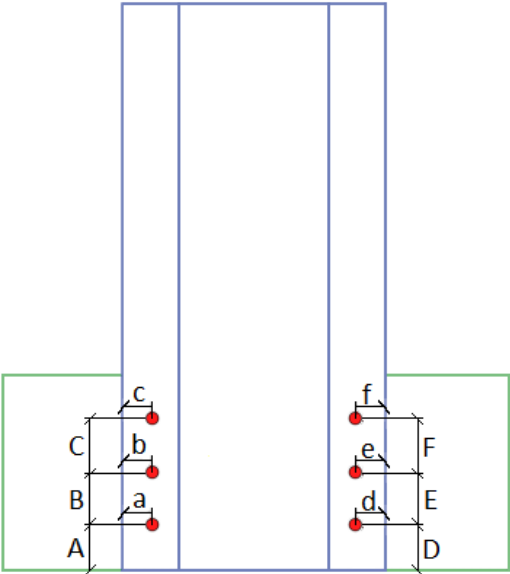| Specimen nr.	a	b	c	d	e	f	A	B	C	D	E	F
T_01	17.53	17.77	17.76	18.19	18.04	17.69	25.57	24.57	25.46	22.46	25.27	24.39
T_02	18.46	17.8	17.76	19.38	17.88	18.08	25.7	24.21	25.3	24.24	24.36	24.8
T_03	17.15	17.06	17.61	18.17	17.18	17.29	26.45	25.03	23.63	24.7	24.73	24.21
Average	17.71	17.54	17.71	18.58	17.70	17.69	25.91	24.60	24.80	23.80	24.79	24.47

Figure B.1: Placement of screws in the T-component specimens.

Appendix C

Experimental results

C.1 Uniaxial tension

For specimen UT_6063_15_01 the extensometer registered a high displacement almost immediately after the test started, and the curve leans a bit backward as can be seen in Fig. C.1b. The curve plotted here has been shifted a distance of 0.0067 which was the average distance between specimen UT_6063_15_02 and UT_6063_15_01 at 200 MPa and 50 MPa. The specimen UT_6063_15_03 had an initial geometrical imperfection in the primary test area, but this does not seem to have influenced the test significantly

(a) 0° direction.

(b) 15° direction.

(c) 30° direction.

(d) 45° direction.

(e) 60° direction.

(f) 75° direction.

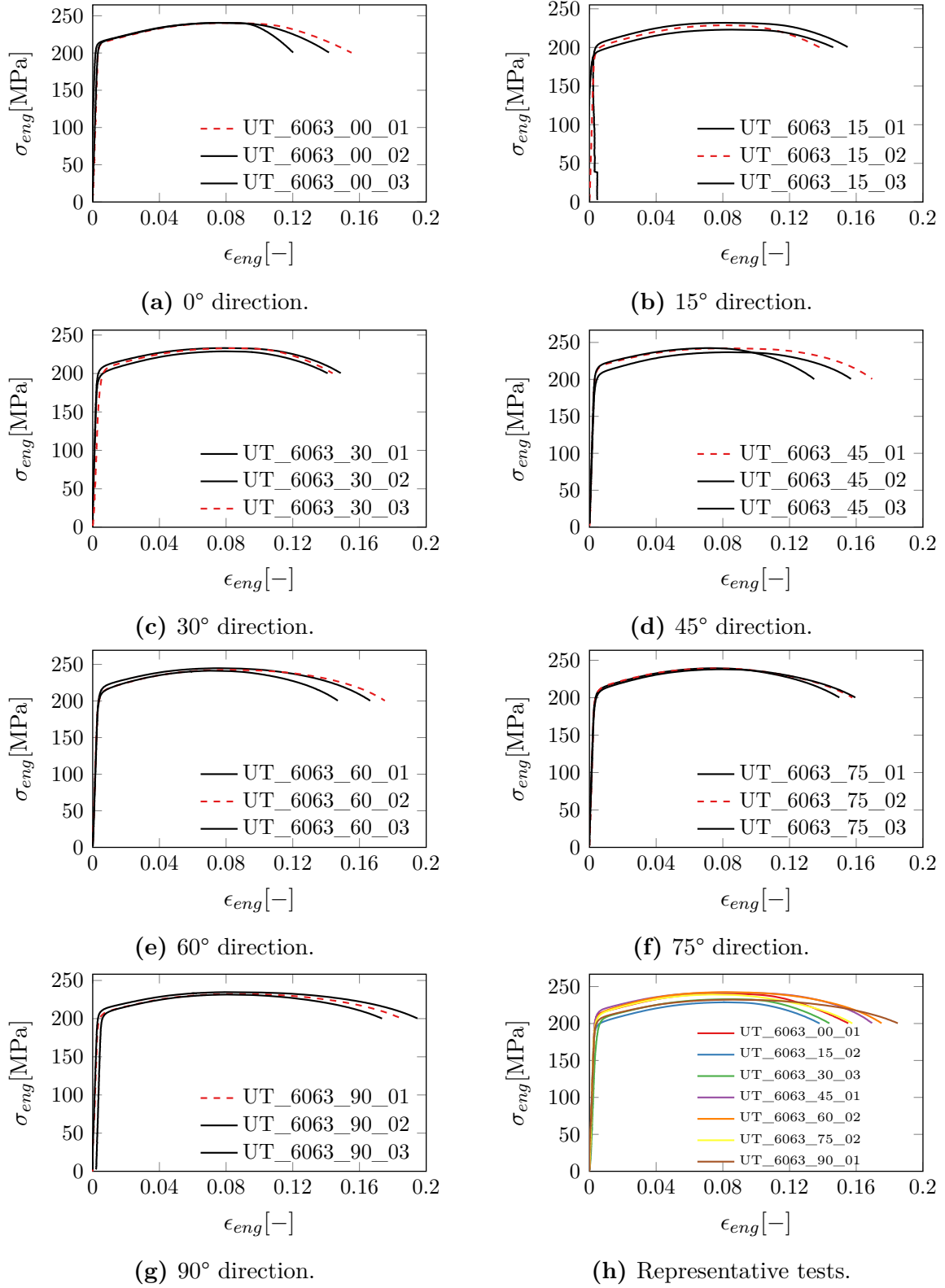**(g)** 90° direction.

(h) Representative tests.

Figure C.1: Results from unaxial tension tests. Representative curves from each test are shown as red dashed lines.
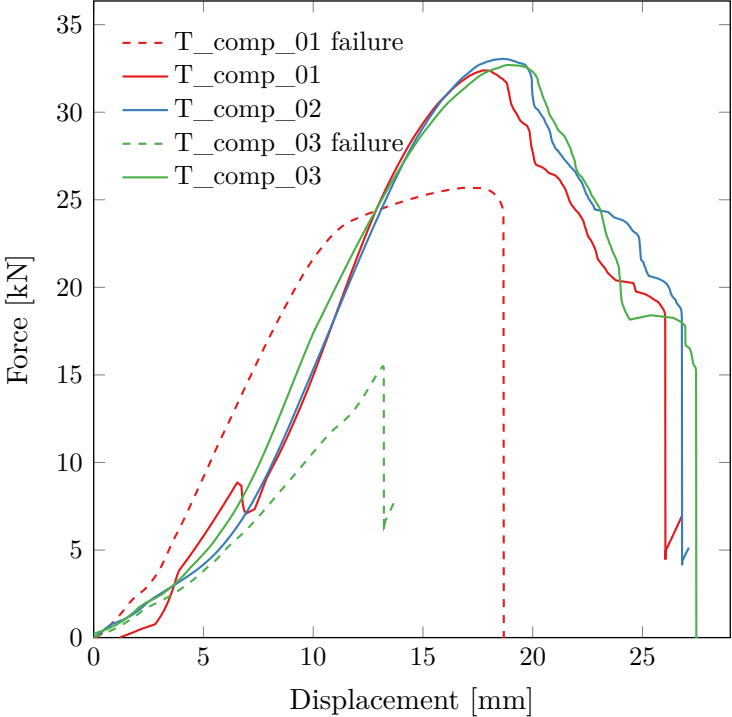
C.2 Component test

Figure C.2: All results from component tests.

Bibliography

[1]   A Toma, G Sedlacek, and K Weynand. "Connections in cold-formed steel". In: *Thin-walled structures* 16.1 (1993), pp. 219–237.

[2]   R. Pedreschi and B. Sinha. "The potential of press-joining in cold-formed steel structures". In: *Construction and Building Materials* 10.4 (1996), pp. 243–250.

[3]   R Lennon, R Pedreschi, and B. Sinha. "Comparative study of some mechanical connections in cold formed steel". In: *Construction and Building Materials* 13.3 (1999), pp. 109–116.

[4]   G Di Lorenzo and R Landolfo. "Shear experimental response of new connecting systems for cold-formed structures". In: *Journal of constructional steel research* 60.3 (2004), pp. 561–579.

[5]   P Wung. "A force-based failure criterion for spot weld design". In: *Experimental Mechanics* 41.1 (2001), pp. 107–113.

[6]   P Wung et al. "Failure of spot welds under in-plane static loading". In: *Experimental Mechanics* 41.1 (2001), pp. 100–106.

[7]   S.-H. Lin et al. "Failure loads of spot welds under combined opening and shear static loading conditions". In: *International Journal of Solids and Structures* 39.1 (2002), pp. 19–39.

[8]   Y.-L. Lee et al. "Ultimate strength of resistance spot welds subjected to combined tension and shear". In: *Journal of Testing and Evaluation* 26.3 (1998), pp. 213–219.

[9]   B. Langrand and A. Combescure. "Non-linear and failure behaviour of spotwelds: a "global" finite element and experiments in pure and mixed modes I/II". In: *International journal of solids and structures* 41.24 (2004), pp. 6631–6646.

[10] B. Langrand and E. Markiewicz. "Strain-rate dependence in spot welds: Non-linear behaviour and failure in pure and combined modes I/II". In: *International Journal of Impact Engineering* 37.7 (2010), pp. 792–805.

[11] R Porcaro et al. "Joining of aluminium using self-piercing riveting: testing, modelling and analysis". In: *International Journal of Crashworthiness* 9.2 (2004), pp. 141–154.

[12] R Porcaro et al. "Self-piercing riveting process: An experimental and numerical investigation". In: *Journal of Materials Processing Technology* 171.1 (2006), pp. 10–20.

[13] R Porcaro et al. "The behaviour of a self-piercing riveted connection under quasi-static loading conditions". In: *International journal of solids and structures* 43.17 (2006), pp. 5110–5131.

[14] R Porcaro et al. "An experimental investigation on the behaviour of self-piercing riveted connections in aluminium alloy AA6060". In: *International Journal of Crashworthiness* 11.5 (2006), pp. 397–417.

[15] R Porcaro et al. "Crashworthiness of self-piercing riveted connections". In: *International Journal of Impact Engineering* 35.11 (2008), pp. 1251–1266.

[16] X. Sun, E. V. Stephens, and M. A. Khaleel. "Fatigue behaviors of self-piercing rivets joining similar and dissimilar sheet metals". In: *International journal of fatigue* 29.2 (2007), pp. 370–386.

[17] X. Sun and M. A. Khaleel. "Strength estimation of self-piercing rivets using lower bound limit load analysis". In: *Science and Technology of Welding & Joining* 10.5 (2005), pp. 624–635.

[18] X. Sun and M. A. Khaleel. "Dynamic strength evaluations for self-piercing rivets and resistance spot welds joining similar and dissimilar metals". In: *International journal of impact engineering* 34.10 (2007), pp. 1668–1682.

[19] J. K. Sønstabø and P. H. Holmstrøm. "Behaviour and Modelling of Self-piercing Screw and Self-piercing Rivet Connections: An Experimental and Numerical Investigation". 2013.

[20] A. Hanssen et al. "A large-scale finite element point-connector model for self-piercing rivet connections". In: *European Journal of Mechanics-A/Solids* 29.4 (2010), pp. 484–495.

[21]   N.-H. Hoang et al. "Structural behaviour of aluminium self-piercing riveted joints: An experimental and numerical investigation". In: *International Journal of Solids and Structures* 49.23 (2012), pp. 3211–3223.

[22]   F Seeger et al. "An Investigation on Spot Weld Modelling for Crash Simulation with LS-DYNA". In: *4th LS-DYNA User Forum, Bamberg.* 2005.

[23]   S. Malcolm and E. Nutwell. "Spotweld failure prediction using solid element assemblies". In: *6th European LS-Dyna users' conference. Gothenburg, Sweden.* Citeseer. 2007.

[24]   S. Sommer and J. Maier. "Failure modeling of a self piercing riveted joint using ls-dyna". In: *8th European LS-DYNA conference.* 2011.

[25]   O.-G. Lademo et al. "Identification and validation of constitutive model and fracture criterion for AlMgSi alloy with application to sheet forming". In: *Materials & Design* 30.8 (2009), pp. 3005–3019.

[26]   D. Achani et al. "Evaluation of constitutive models for textured aluminium alloys using plane-strain tension and shear tests". In: *International journal of material forming* 4.2 (2011), pp. 227–241.

[27]   S Dumoulin et al. "Description of plastic anisotropy in AA6063-T6 using the crystal plasticity finite element method". In: *Modelling and Simulation in Materials Science and Engineering* 20.5 (2012), p. 055008.

[28]   F Barlat et al. "Linear transfomation-based anisotropic yield functions". In: *International Journal of Plasticity* 21.5 (2005), pp. 1009–1039.

[29]   G. Davies. *Materials for automobile bodies.* Butterworth-Heinemann, 2012.

[30]   A. S. Training. "Self-study programme 383, Audi TT Coupé' 07 - Body".

[31]   Böllhof. "Self-pierce riveting for perfect joints".

[32]   A. S. Training. "Self-study programme 456, Audi A8'10".

[33]   E. FDS. "The flow drill screw for high strength sheet metal joints". 2010.

[34]   B Gladman et al. *LS-DYNA® Keyword User's Manual–vol. II–Version 971.* 2013.

[35]   J. R. Davies. *Aluminium and aluminium alloys.* ASM international, 1993.

[36]   A. Association et al. "International alloy designations and chemical composition limits for wrought aluminum and wrought aluminum alloys". 2009.

[37] E. Fagerholt. "Field Measurements in Mechanical Testing Using Close-Range Photogrammetry and Digital Image Analysis". PhD thesis. Norwegian University of Science and Technology, Department of Structural Engineering, 2012.

[38] G. Besnard, F. Hild, and S. Roux. ""Finite-element" displacement fields analysis from digital images: application to Portevin–Le Châtelier bands". In: *Experimental Mechanics* 46.6 (2006), pp. 789–803.

[39] T. L. Anderson. *Fracture mechanics: fundamentals and applications.* CRC press, 2005.

[40] H. J. Kim and J. A. Yura. "The effect of ultimate-to-yield ratio on the bearing strength of bolted connections". In: *Journal of Constructional Steel Research* 49.3 (1999), pp. 255–269.

[41] N. Stander et al. "LS-OPT user's manual". In: *Livermore software technology corporation* (2008).

[42] B Gladman et al. *LS-DYNA® Keyword User's Manual–vol. I–Version 971.* 2007.